A THEORETICAL AND EXPERIMENTAL TREATMENT OF PERISTALTIC PUMPING AND ITS RELATION TO URETERAL FUNCTION

by

STEVEN LOUIS WEINBERG

S.B., Drexel Institute of Technology
(1965)

S.M., Massachusetts Institute of Technology
(1967)

SUBMITTED IN PARTIAL FULFILLMENT
OF THE REQUIREMENTS FOR THE
DEGREE OF DOCTOR OF PHILOSOPHY

at the
MASSACHUSETTS INSTITUTE OF TECHNOLOGY
March, 1970

Signature of Author Signature redacted
Department of Mechanical Engineering,
March 1970

Certified by Signature redacted
Thesis Supervisor

Accepted by Signature redacted
Chairman, Departmental
Graduate Committee

Archives
MASS. INST. TECH.
JUL 16 1970
LIBRARIES

A THEORETICAL AND EXPERIMENTAL TREATMENT OF PERISTALTIC PUMPING AND ITS RELATION TO URETERAL FUNCTION

by

Steven L. Weinberg

Submitted to the Mechanical Engineering Department on February 24, 1970 in partial fulfillment of the requirement for the degree of Doctor of Philosophy.

ABSTRACT

Pumping by means of an infinite train of peristaltic waves is investigated under conditions where the inertial forces can be neglected. The analysis is formulated in the unsteady laboratory reference frame for both two-dimensional and axially-symmetric geometries because of its direct application to experimental pumps and ureteral function. Pressure variations as a function of position, time and geometry were calculated. In addition, new theoretical consideration is given to the phenomena of "reflux" and "trapping".

An experimental program using a quasi-two-dimensional apparatus was carried out in order to investigate the quantitative and qualitative aspects of the theory. Studies of pressure vs time, for various squeeze ratios, flow rates, and Reynolds numbers, were conducted for a sinusoidal wall geometry. No effects of Reynolds number were observed within the operating range of the experiments, i.e. up to a Reynolds number of 0.25. Visual studies documented the existence of "reflux" along the walls as well as the identification of "trapped" flow regions beneath the crests of the waves. Quantitative measurements relating to these phenomena were made, and are in agreement with the theory.

The infinite-wave-train analysis is combined with a discussion of urinary physiology in order to develop a model for ureteral function. Evaluation of urometric data provided a basis for formulation of a ureteral wave shape which agrees with radiographic and visual observations. According to the model, the bulk of the urine is carried within a large bolus region which has little pressure variation associated with it. The major pressure variations occur within a two-stage-contracted region which directly follows the bolus. The peak pressure within the wave occurs approximately in the center of the contracted region, not at the end of the bolus. Dimensions within the contracted region (0.1 mm or less) are approximately equal to the dimensions within the resting ureter. Consideration is given to a circular cross section, a lobed cross section, and a combined cross section which includes both circular and lobed regions. Finally, a discussion is included of "reflux" and "trapping" as related to ureteral function.

Thesis Supervisor: Ascher H. Shapiro
Title: Professor and Head, Department of Mechanical Engineering

ACKNOWLEDGEMENTS

The author wishes to express his appreciation to the following persons: Professor A. H. Shapiro, Professor M. Jaffrin, Eugene Eckstein, David Palmer, and Dick Fenner. In addition, the author wishes to thank Miss Sara Rothchild and Mrs. Rosmarie Geering for their aid in typing the manuscript. Finally, the author wishes to express his appreciation to his wife, Arlene, for her aid and encouragement throughout his doctoral program.

Acknowledgement is also made to the M.I.T. Computation Center for its work, done under Problem Number M 5370.

The work was supported under contract number N00014-67-A-0204-0008, Office of Naval Research.

TABLE OF CONTENTS

NOMENCLATURE

a	mean half-width of passage (plane geometry); or mean radius (axisymmetric geometry)
b	half-amplitude of peristaltic wave
c	wave speed
ϕ	non-dimensional parameter relating to the leakage flow in experiment (refer to Equation (D-7))
e,f,i,j	variables describing continuous wall geometry
H	non-dimensional wall coordinate, $\frac{h}{a}$
h	transverse wall coordinate
$\bar{H}$	mean wall coordinate, $\frac{\bar{h}}{a}$
k	asymmetry factor describing bolus size for continuous geometry
ℓ	length
L	non-dimensional length, $\frac{\ell}{\lambda}$
P	pressure
$\tilde{P}$	non-dimensional pressure ($\frac{a^2\rho}{3\mu c\lambda}$ for plane geometry; $\frac{a^2\rho}{8\mu c\lambda}$ for axisymmetric geometry)
ΔP_λ	pressure rise per wave length
$\Delta\tilde{P}_\lambda$	non-dimensional pressure rise per wave ($\frac{a^2\Delta P_\lambda}{3\mu c\lambda}$ for plane geometry; $\frac{a^2\Delta P_\lambda}{8\mu c\lambda}$ for axisymmetric geometry)
Q	instantaneous flow rate in lab reference frame
Q_ψ	instantaneous flow rate between axis and the streamline
Q_L	instantaneous leakage flow in the experiment
Q_F	instantaneous forward flow in the experiment

Q_n net instantaneous flow in the experiment

Q^* net instantaneous flow per half-width of channel per unit height, $\frac{Q_n}{2w}$

$\bar{Q}$ time-mean flow observed in lab reference frame

$\bar{Q}_\psi$ time-mean flow between axis and the streamline

$\bar{Q}_R$ time-mean reflux flow

$\bar{Q}_L$ time-mean leakage flow in experiment

Q_U net flow carried by a ureteral wave (spurt volume)

q flow rate observed in the lab reference frame

r wave frame transverse coordinate (axisymmetric)

R_c non-dimensional catheter radius, $\frac{r_c}{a}$

r_c radius of catheter

R peristaltic Reynolds number, $\frac{a^2 c}{\nu\lambda}$

R_x entry length Reynolds number, $\frac{c\ell_x}{\nu}$

$\mathcal{R}$ reflux flow as a fraction of net flow

t time

t_p residence time of a particle in the wave reference frame

u, v velocity components in wave frame (plane)

U, V velocity components in lab frame (plane)

w height of test section

x, y coordinates in wave frame (plane)

x non-dimensional coordinate, $\frac{x}{\lambda}$

X, Y coordinates in lab frame (plane)

Greek

α	wave number, $\frac{a}{\lambda}$
β,γ,σ	variables defined by Equation (B-4)
ϕ	squeeze ratio, $\frac{b}{a}$
λ	wave length
μ	viscosity
ν	kinematic viscosity
ρ	density
ψ	stream function in wave reference frame
δ	boundary layer thickness
χ	stream function ratio, $\frac{\psi}{\psi_w}$
θ^*	non-dimensional mean flow per half-width per unit height of test channel, $\frac{\overline{Q^*}}{ac}$
θ	non-dimensional time-mean flow ($\frac{\bar{Q}}{ac}$ for plane geometry; $\frac{\bar{Q}}{\pi a^2 c}$ for axisymmetric geometry)
θ_0	non-dimensional flow for $\Delta P_\lambda = 0$
θ_R	non-dimensional reflux flow ($\frac{\bar{Q}_R}{ac}$ for plane geometry; $\frac{\bar{Q}_R}{\pi a^2 c}$ for axisymmetric geometry)
$\tilde{\psi}$	non-dimensional stream function ($\frac{\psi}{ac}$ for plane geometry; $\frac{\psi}{a^2 c}$ for axisymmetric geometry)
η	non-dimensional coordinate ($\frac{Y}{a}$, $\frac{y}{a}$ for plane geometry; $\frac{R}{a}$, $\frac{r}{a}$ for axisymmetric geometry)
τ	dimensionless time, $\frac{ct}{\lambda}$

Subscripts

w	refers to wall position
t	refers to edge of trapped bolus
0	refers to the position on a wave where $\xi = 0$
u	refers to conditions at upstream reservoir
d	refers to conditions at downstream reservoir
N	refers to node N
ψ	refers to the streamline ψ

1. INTRODUCTION

1.1. Objectives

Recently, various authors have discussed different aspects of peristaltic pumping, but few have attempted to relate their work to the actual behavior of the ureter. This thesis has two primary objectives. First, to substantiate by experiment the theoretical predictions for an infinite train of peristaltic waves. Second, to formulate a fluid mechanical model for ureteral function.

From the medical point of view, such a model should yield insight into the functioning of normal and abnormal ureters. Further, it may also pose new questions and hypotheses which should be considered by ureteral physiologists. A quantitative understanding of ureteral function might provide information concerning the possible effects of catheters on the pressure pulse and the mechanism of bacterial reflux.

1.2. Previous Work

The theoretical formulations of different investigators can be conveniently categorized in terms of the following variables for an infinite train of peristaltic waves. These are

(i) the wave number, $\alpha \equiv a/\lambda$

(ii) the squeeze ratio, $\phi \equiv b/a$

(iii) the Reynolds number, $R \equiv a^2 c/\lambda\nu$*

(iv) the flow parameter, $\theta \equiv \bar{Q}/ac$ for plane geometry;

$\theta \equiv \bar{Q}/\pi a^2 c$ for axisymmetric geometry

*For discussion of the appropriate definition of Reynolds number see Reference (4), Appendix A.

as well as the wave shape. In the published investigations, only sinusoidal waves were considered except as noted.

Burns and Parks[1] considered the case of zero Reynolds number, i.e. inertial forces << viscous forces, for both plane and axisymmetric geometries. Since their solution was derived in terms of powers of ϕ, the solution is limited to small squeeze ratios. In some calculations, terms of order ϕ^4 were considered. Their solution allowed for arbitrary values of wave numbers.

Hanin[2] considered the case of a plane geometry with small squeeze ratios, and with the mean pressure gradient equal to zero. His solution contained the long-wave-length approximation, i.e. $\alpha = 0$, but allowed for arbitrary Reynolds numbers.

Fung and Yih[3] considered the case of a plane geometry, but allowed for arbitrary values of Reynolds number and wave number. Their solution is expressed as an expansion in ascending powers of ϕ, and is thus only valid for small squeeze ratios.

Shapiro, Jaffrin, and Weinberg[4] considered both the plane and axisymmetric geometries for zero Reynolds number and wave number. Their solution allows for arbitrary squeeze ratios, and many results are given in closed form. The results include particle trajectory calculations, and disclosure of two fluid mechanical phenomena designated as reflux and trapping.

Jaffrin[5] established the effects of wave number and Reynolds number in the plane geometry by expansions in powers of α and R. The solution, which allows for arbitrary amplitude ratio ϕ, shows the effects of wave number and Reynolds number on the pressure rise per

wavelength and on the time-mean flow. The effects of α and R on reflux and trapping are also included.

A detailed comparison of the foregoing theories is not included within this thesis as Jaffrin[5] has illustrated the relationships between the models. It will suffice to mention that all agree in the relevant ranges of the governing parameters α, ϕ, and R.

Lykoudis[6] made an attempt to model the fluid mechanics of the ureter. However, instead of peristalsis, he considered a collapsing cylinder whose radius varied sinusoidally with time. The model was limited in that it did not model the anatomical operation of the ureter and it could not produce any net flow unless check valves were fitted at either end of the cylinder.

1.3. Structure of Thesis

Chapter 2 describes the physiology of the ureter as a basis for later formulation of a theoretical model. Both normal and abnormal conditions are discussed. Operation of the kidneys and bladder are mentioned when relevant to ureteral function.

Chapter 3 presents briefly the analysis as viewed in the unsteady laboratory reference frame. Emphasis is placed on those aspects relevant to the ureteral model described in Chapter 4. Formulation in the lab reference frame shows how the infinite-wave-train theory can be modelled by the finite-wave-length experiment of Chapter 5. Chapter 3 also includes a discussion of trapping and reflux.

A simplified model of ureteral function is present in Chapter 4 for various possible geometries. The effects of a catheter on the

flow rate and pressure field are also discussed.

Chapter 5 is concerned with a two-dimensional experiment whose purpose is to test the validity of the inertia-free model. In this chapter, qualitative and quantitative results are presented.

The conclusions of Chapter 6 are given in two parts. The first concerns the relationship between the experimental observations and the predictions of the infinite-wave-train theory. The second part assesses the ureteral model and its relationship to medical observations.

2. URINARY PHYSIOLOGY

2.1. Normal Physiology of the Urinary Tract

In order to model the fluid mechanics within the ureter, a basic understanding of its physiology is required. This chapter is intended to provide a simplified view of ureteral function and to summarize current physiological literature. When necessary, both the anatomy and histology of the ureter will be discussed in order to aid in the understanding of ureteral function. From the concepts presented, a simplified physiological model of ureteral function will be developed.

Figure 1 is a general sketch of the ureter and of the other elements of the urinary system. The urine, which is an ultrafiltrate of blood plasma, is formed in the cortex region of the kidney in a large number of small ducts known as nephrons. Both active reabsorption and secretion of selective materials occur within these ducts. The nephrons terminate in large tubules and finally into primary ducts known as calyces. These in turn empty into the renal pelvis which is the upper reservoir of the ureter. The ureters, which are located distal to the renal pelvis, carry the fluid by means of peristaltic waves to the bladder where the urine is stored until micturition.

The calyx, renal pelvis, ureter, and bladder will be discussed individually and then combined to yield a dynamic picture of ureteral function. The discussion will be limited to normal ureters since their operation must be understood before abnormal systems can be comprehended.

Renal Pelvis and Calyces. The calyces are the primary ducts proximal to the pelvis. Narath[7] and Kiil[8] among others, showed the existence of calycic contractions through the activation of the longitudinal muscles located in their walls. Kiil further showed the activity of the calyces and renal pelvis to be independent. Histologically, each of the calyx ducts was shown to have circular or sphincter muscles at the proximal end (sphincter fornicis) and distal end (sphincter calycis) as illustrated in Figure 1. Using urometric techniques, Kiil showed that even though sphincteral contractions do occur, the contracted regions can not withstand mild pressure gradients. For this reason, he concluded that the sphincters are of subordinate importance in the transport of urine.

Kiil also demonstrated that the pressure variations which exist in the calyces are very small compared with the magnitude of the pressure variations within the ureter. The resting pressure in the calyces was shown to be approximately equal to the renal pelvic pressure. Even though the calyces and proximal members of the excretory system are of great physiological interest, their dynamics do not play a major role in the functioning of the ureter.

Rattner, Fink, and Murphy[9], in addition to Kiil, showed conclusively that the pressure in the renal pelvis remains approximately constant with time at a level ranging between 2 mm to 10 mm Hg. Morales, Crowder, Fishman and Maxwell[10] demonstrated the dependency of renal pressure on urine flow rate. Their results indicated that increased rates of diuresis tend to dilate the renal pelvis and increase renal pressure.

The actual shape of the renal pelvis varies between individuals; however, this variation in shape does not necessarily affect its functioning. In general, the shape of the renal pelvis can be considered similar to that of a funnel. Renal pelvic volume ranges from 3 cc to 5 cc, and remains constant independent of the peristaltic transport of urine.

It is evident that the renal pelvis undergoes mild contractions of its detrusor muscles, but it is not known whether this contraction is actually the beginning of the peristaltic wave. When pressure variations in the renal pelvis are observed they are usually similar to the peristaltic pressure fluctuations but of much smaller magnitude (approximately 1.5 mm of Hg).

Histologically, the division line between the calyces and renal pelvis is the location of the sphincter calycic muscles. However, no precise dividing line exists between the renal pelvis and the ureter. Anatomically, this junction is not well defined since the funnel-shaped pelvis exists only in very few patients. However, this general region is designated as the ureteropelvic junction.

Kiil showed that the renal pelvis and ureteral cone fill simultaneously while in relaxed state. The peristaltic wave forms in the ureteropelvic junction and the wave progresses toward the bladder carrying the urine which was contained within the ureteral cone.

Ureter. In adults the normal length of the ureter ranges from 25 cm to 30 cm with a resting outside diameter varying between 2 mm and 10 mm. Figure 2 shows a microscopic cross section of a contracted

segment of a human ureter*. It should be mentioned that the actual cross-sectional shape of the lumen is not well known in vivo. The folded appearance of the lumen might be a result of the fixation process. Internal dimensions of the lumen range between 0.1 mm up to 5 mm. The lumen is surrounded by both circular and longitudinal muscles lying within a sheath of connective tissue and blood vessels, giving the external appearance of a thin smooth tube. Bäcklund[12] is one of the few investigators who attempted to record diametric variations of the ureter with a peristaltic wave. It appears from his simultaneous recordings of external diameter and internal pressure that pressure variations are associated with sections of the ureter undergoing observable dimensional fluctuations. His recordings of ureteral diameter and pressure as a function of time yield some insight into the wave form, but the important dimensions required for ureteral modelling are the internal dimensions of the lumen at various stages in the wave. The exact variation of lumen shape with time and pressure still remains unknown.

Recent cineradiographic studies of Barry, Absher, and Boyarsky[13] showed that a lag exists between the initiation of contraction and the peak of the pressure event. This delay ranges from about 1 second to 1.6 seconds. This fact will be of importance in analyzing the results of the theoretical model.

Another interesting observation reported by Barrey et al. was that the bolus seemed to pass the tip of the catheter at the low pressure

---

*From Reference (11).

phase in the recording. They also reported that a further contraction of the ureter exists after the "visible image" or bolus passes the recording hole in the catheter.

The peristaltic wave travels at an average velocity of approximately 3 cm/sec with a frequency ranging from 3 to 10 waves per minute depending on the activity of the kidneys. Investigators have shown by means of pressure-time traces that the character of the pressure pulse is similar at various locations along the ureter.

Davis, Zimskind, and Paquet[14], in addition to Kiil and others, have shown that the basal pressure (see Figure 3) within the ureter remains constant throughout the entire length of the ureter, independent of the intravesical (bladder) pressure. This pressure is approximately equal to the pressure within the renal pelvis and calyces. As a contraction complex passes over a ureteral catheter the pressure peaks at values ranging between 13 mm and 35 mm of Hg and then returns to the basal level. Figure 3a is a representation of a series of typical normal pressure waves recorded with an intralumenal catheter by Kiil. Only pressure pulses obtained by Kiil are presented, but many other investigators using modern techniques have obtained similar results.

Average flow rates through each ureter can range up to 2.5 cc/min. Morales et al.[10] conducted a series of experiments which demonstrated that each peristaltic wave carries between 0.02 and 0.7 cc.

The flow through the ureters is not continuous, but appears to enter the bladder in spurts. Figure 3c helps illustrate this point. By considering the location of the catheter, the wave speed, the time, and the duration of the spurt, the fluid entering the bladder can be

shown to coincide with the arrival of a wave at the ureterovesical junction. As was previously mentioned, upon formation of a wave, a small volume of fluid is confined immediately forward of the contraction region. This bolus of fluid is transported with the wave and is probably responsible for the spurt observed at the ureterovesical orifice. Between the spurts there appears to be little or no flow entering into the bladder[10].

It has also been observed that increased flow rates are accomodated by increased peristaltic frequency and increased bolus length, with only a small increase in the diameter of the bolus [8, 9, 10, 15]. If the basal pressure in the renal pelvis is artificially raised to an abnormal level all observed peristaltic activity ceases, even though the peristaltic action potential can still be recorded through the ureteral membrane.

Urometric techniques have shown that throughout the entire length of the ureter the basal pressure is independent of bladder pressure. This can be the case only if there is some type of valve which isolates the bladder from the ureter. This so-called valve is known as the ureterovesical junction. In man, the ureter does not directly pass through the bladder wall, but remains in the bladder wall for 5 mm to 26 mm before it terminates at the ureterovesical orifice[16]. The details of physiological operation of the valve are not completely understood. One possible mechanism which might account for the valve action could be a squeezing of the ureterovesical junction resulting from the internal pressure of the bladder on the bladder wall. Failure of the valve results in a gross reflux of urine into the ureter with a

corresponding rise in basal and interpelvic pressure.

The physiological significance of the smooth longitudinal muscles located in the ureteral wall needs to be determined. Boyarsky[17] described a secondary gliding motion of the ureteral wall in the following manner, "The ureteral wall slides up over the bolus like a trouser over a leg". To understand the purpose of this activity, the longitudinal motion must be studied in much greater detail.

Bladder. The bladder is a highly elastic vesical whose wall is composed of three distinct layers of smooth muscle which are irregularly interwoven throughout the connective tissue of the bladder wall. The volume of the bladder is highly dependent on the size of the patient and the stage of filling, but may be as high as 500 ml. The desire to void usually occurs when the intravesicular pressure is nearly equal to the peak peristaltic pressure (approximately 25 mm of Hg).

2.2. Pathology of the Ureters

In this section an attempt will be made to describe briefly a few of the abnormal conditions which may occur within the urinary tract. Although many abnormal conditions can be treated successfully, a large number are not well understood and therefore specific treatment is unknown.

One of these latter conditions is known as "bulk reflux". Bacteria which invade the bladder through the urethra irritate the bladder wall and musculature, causing failure of the ureterovesical valve. Since the pressure in the bladder is usually higher than the basal level

within the ureter, failure of this valve results in a rapid Poiseuille type back flow towards the kidney.

Under certain poorly defined conditions bacteria which were originally in the bladder or lower ureter make their way back to the kidneys in a matter of hours[18]. This type of reflux will be defined as "peripheral reflux". Diffusion, or even diffusion accompanied by the motility of the bacteria, has been discounted as a plausible mechanism for this type of bacterial reflux due to the time scale involved.

The ureters can also become obstructed by kidney stones, cancers or other disorders which tend to occlude the lumen of the ureters. External lesions may also occur constricting the motion of the ureters. These conditions have severe effects on the performance of the ureters and exhibit themselves as severe modifications of the pressure and flow variations within the afflicted ureter.

2.3. Simplified Physiological Model

Given the physiological facts above, the task still remains to generate a simplified physiological model which can be used to explain the fluid mechanics of ureteral function. Shapiro, Jaffrin and Weinberg[4] indicated that the inertia-free model could be used to obtain insight into urodynamics. They also showed that in the ureter the wavelength is long compared to the diameter of the ureter. For simplicity of computation, we assume that the wave does not change shape while propagating between the renal pelvis and ureterovesical junction.

The peristaltic wave appears to be composed of a relaxed region, a contracted region, and a distended bolus region (see Figure 1).

In this analysis, the longitudinal motion of the ureter will be neglected.

The shape of the lumen during passage of a wave is not known, but it is conceivable that the lumen varies between lobed shape at the relaxed regions and quasi-circular in the distended bolus region. For this reason both two-dimensional and axisymmetric geometries will be considered.

As can be seen from typical pressure pulses represented in Figure 3, the distal and proximal basal pressures across the wave are approximately equal. For this reason we will assume that the pressure rise across the wave is small compared with the peak pressure. This assumption will be explored in greater detail in Section 4.2.

Since the flow enters the bladder in spurts and no flow is observed between spurts, it can be assumed that the fluid velocities are approximately zero in the relaxed regions of the ureter. This is in agreement with the observations that there are no pressure gradients in the relaxed regions. Therefore, all the significant fluid motions are associated with the contracted and dilated region of the wave.

To summarize, certain characteristics of ureteral function are quite well documented and can be used to establish a model. These characteristics are:

(i) the negligibly small pressure rise per wavelength

(ii) the magnitude of the maximum pressure

(iii) the qualitative shape of the pressure pulse

(iv) the quantity of liquid carried per wave

On the other hand, certain gaps exist in the physiology which hinder close comparisons between the theoretical model and the ureter.

The first major gap is the lack of knowlege concerning the intralumenal wall variation with time and distance along the ureter. Because of the complex wall structure of the ureters, observation of the external diameter does not yield reliable information about the dimensions and shape of the lumen.

The second large deficiency in the physiology concerns the measurements of pressure variation and flow within the ureter at various stages of activity. Most investigators have considered either pressure variations or flow characteristics, but not the two simultaneously. In order to make accurate comparisons between the ureter and the models, it would be desirable to record flow and pressure simultaneously.

2.4. End Regions

Ureterovesical Junction. The details of operation and the anatomy of the ureterovesical junction were discussed in some detail in Section 2.3. For this reason, discussion in this section will be limited to a possible explanation of how a wave with $\Delta P_\lambda \tilde{=} 0$ can expel urine into a pressurized bladder.

One possible explanation for this apparent contradiction might be a variation in the wave shape locally in the region of the bladder. In this region the contracted section of the wave might undergo further contraction causing a strong positive pressure rise in a manner analogous to a tightening sliding cuff. Further physiological studies of this junction would be necessary to determine the validity of the above hypothesis.

Ureteropelvic Junction. The formation of the wave in the ureteropelvic region of the kidney can be considered fluid mechanically as a problem onto itself. Certain facts can be observed from urometric studies in the ureter. Formation of the wave does not seem to affect the pressure pulse or basal pressure level at distal points along the ureter. Using the above information, one can hypothesize that the pressure rise in the forming wave must be approximately zero at all stages of formation.

Since the ureter is almost empty prior to formation of a wave, all the urine carried by a particular wave must come predominately from the renal pelvis reservoir.

From the current state of knowledge regarding ureteral physiology, it is obvious that before any detailed modelling of the ureterovesical or ureteropelvic junctions can be accomplished, extensive physiological studies must be undertaken.

3. ANALYSIS OF AN INFINITE WAVE TRAIN

As analytical background for Chapters 4 and 5, it will be necessary to develop briefly the analysis of an infinite wave train in the unsteady laboratory reference frame. The concepts of "peripheral reflux" and "trapping" will also be discussed. By directly utilizing the lab reference frame, it will be shown that under certain conditions the infinite-wave-train situation can be simulated by a finite-wave-train experiment.

3.1. Assumptions (Infinite-Wave-Train Model)

Infinite Wavelength. In the previous chapter, it was mentioned that the resting dimensions of the ureter are still not well defined, but it is expected that the breadth of the lumen ranges somewhere between 0.1 mm and 3 mm. The length of a wave is about 15 cm, yielding a value of wave number α of less than 1/50. Since α is very small, the infinite-wavelength approximation can be used.

This assumption makes it possible to neglect the transverse components of the pressure gradient as compared with the longitudinal gradients. In other words, the pressure can be assumed instantaneously uniform across each section.

Inertia-Free Flow. As was demonstrated by Shapiro et al.[4] the viscous forces within a peristaltic wave are of order $\mu c/a^2$, at least when no thin boundary layer region exists. The order of magnitude of the inertial forces can be written as $\rho c^2/\lambda$. Knowing that the Reynolds

number is the ratio of inertial forces to viscous forces, it can be seen that the appropriate Reynolds number can be written as $R = a^2 c/\nu\lambda$. For the ureter this Reynolds number is of order 0.25. This value is small enough to give some relevance to the inertia-free theory.

The two assumptions of infinite wavelength and zero Reynolds number lead to instantaneous Poiseuille flow at each section.

Constant Fluid Properties. In this analysis the viscosity and density will be considered constant with time. The viscosity of urine is approximately 0.01 Poise at 38°C.

Wall Shape. An infinite wave train has a wall shape of the general form

$$H = H(\xi - \tau) \tag{3-1}$$

At a later stage in the analysis, the wave shape will be restricted specifically to a sinusoidal geometry. It should be reemphasized that this definition of wall shape only allows for transverse motion of the wall.

3.2. Basic Formulation (Two-Dimensional Geometry)

Using the assumptions described in Section 3.1, the governing equations of motion reduce to the following form (refer to Figure 4a for the nomenclature):

X-Momentum: $$\frac{\partial P(X,t)}{\partial X} = \mu \frac{\partial^2 U(X,y,t)}{\partial X^2} \tag{3-2a}$$

Y-Momentum: $$\frac{\partial P}{\partial Y} = 0 \qquad (3\text{-}2b)$$

Continuity: $$\frac{\partial U}{\partial X} + \frac{\partial V}{\partial Y} = 0 \qquad (3\text{-}3a)$$

In integral form, the equation of continuity can also be expressed as:

$$\frac{\partial Q(X,t)}{\partial X} + \frac{\partial h(X,t)}{\partial t} = 0 \qquad (3\text{-}3b)$$

Boundary Conditions:

$$\left.\begin{aligned} \frac{\partial U}{\partial Y} &= 0 \\ V &= 0 \end{aligned}\right\} \quad @ \quad Y = 0 \qquad (3\text{-}4a)$$

$$\left.\begin{aligned} U &= 0 \\ V &= \frac{\partial h}{\partial t} \end{aligned}\right\} \quad @ \quad Y = h \qquad (3\text{-}4b)$$

The above boundary conditions describe the condition of symmetry on the axis and the no-slip condition at the walls, respectively.

Integration of the momentum equation (3-2a), using the boundary conditions (3-4), leads to a locally-Poiseuille velocity profile,

$$\frac{U}{c} = \frac{3}{2} \frac{\partial \tilde{P}}{\partial \xi} (\eta^2 - H^2) \qquad (3\text{-}5)$$

Using this velocity distribution, the instantaneous rate of flow through the cross section can be represented as

$$\frac{Q(\xi,\tau)}{ac} = \int_0^1 \frac{U}{c} \, d\eta \qquad (3\text{-}6)$$

A second form for the instantaneous flow can be obtained from integration of the continuity relation (3-3b), i.e.

$$\frac{Q(\xi,\tau)}{ac} = -\int \frac{\partial H}{\partial \tau}\, d\xi + f(\tau) \tag{3-7}$$

We now calculate the dimensionless time-average flow, $\theta \equiv \bar{Q}/ac$, as

$$\theta(\xi) \equiv \int_0^1 \frac{Q(\xi,\tau)}{ac}\, d\tau \tag{3-8}$$

Using Equations (3-5) and (3-6), the pressure gradient at any section can be shown to be

$$\frac{\partial \tilde{P}}{\partial \xi} = -\frac{1}{H^3}\frac{Q(\xi,\tau)}{ac} \tag{3-9}$$

The periodicity of the wall coordinate can now be employed to describe the periodic character of other variables. In particular, the pressure gradient and the local flow must also be periodic and of the following form:

$$\frac{\partial \tilde{P}}{\partial \xi}(\xi,\tau) = \frac{\partial \tilde{P}}{\partial \xi}(\xi - \tau) \tag{3-10a}$$

and

$$Q(\xi,\tau) = Q(\xi - \tau) \tag{3-10b}$$

Because of the periodic character of these dependent variables, it is convenient to introduce the variable $\tilde{x} \equiv (\xi - \tau)$. Equation (3-7) can now be integrated in terms of this new variable.

$$\frac{Q(\tilde{x})}{ac} = H(\tilde{x}) + f(\tau) \tag{3-11}$$

For a periodic system, Equation (3-10b) shows that $f(\tau)$ must be equal to a numerical constant, i.e. $f(\tau) = F$. Using the time mean of Equation (3-8) along with Equation (3-11) results in the following form of dimensionless time-mean flow, which is independent of ξ:

$$\theta = \bar{H} - H + \frac{Q}{ac} \tag{3-12a}$$

where

$$\bar{H} \equiv \int_0^1 H(\xi)d\xi \tag{3-12b}$$

Rearrangement of Equation (3-5) with the help of Equation (3-12) results in the following velocity distribution:

$$\frac{U}{c} = \frac{3}{2}\left\{\frac{\theta - \bar{H}}{H} + 1\right\}\left\{1 - \frac{\eta^2}{H^2}\right\} \tag{3-13}$$

From continuity equation (3-3a) and boundary condition (3-4c), the V component of velocity can be shown to equal

$$\frac{V}{c} = \frac{3}{2}\,\alpha\,\frac{\partial H}{\partial \xi}\left\{\frac{\theta - \bar{H}}{H}\left(\frac{\eta}{H}\right) - \left(\frac{2}{3} + \frac{\theta - \bar{H}}{H}\right)\left(\frac{\eta}{H}\right)^3\right\} \tag{3-14}$$

where $\alpha \equiv a/\lambda$.

The local pressure gradient at any point within the peristaltic wave may now be found from Eq. (3-2a) as

$$\frac{\partial \tilde{P}}{\partial \xi} = -\frac{1}{H^2} - (\theta - \bar{H})\frac{1}{H^3} \tag{3-15}$$

The pressure rise per wavelength can now be found merely by integrating this relation over one wavelength for any flow θ and any periodic wave shape $H(\xi - \tau)$.

Finite Wave Train. Since one cannot conveniently perform a laboratory experiment with an infinite train of waves, it is necessary to determine under what conditions a finite-wave-train experiment can adequately simulate the infinite-wave-train model.

The instantaneous flow defined by Equation (3-11) is valid for any wave shape. Using Equations (3-8) and (3-11) the dimensionless-mean flow becomes

$$\theta(\xi) = \bar{H} + \frac{1}{\tau}\int_0^{\tau} f(\tau)d\tau \qquad (3\text{-}16)$$

Substituting relation (3-11) into Equation (3-9) results in an equation defining the pressure gradient in terms of wall position and the as yet unknown function $f(\tau)$ becomes

$$f(\tau) = \left\{ -(\tilde{P}_d - \tilde{P}_u) - \int_0^L \frac{d\xi}{H^2} \right\} \frac{1}{\int_0^L \frac{d}{H^3}} d\xi \qquad (3\text{-}17)$$

where the $\tilde{P}_u$ and $\tilde{P}_d$ are the dimensionless pressures at the input and exit of the pump, respectively, and L is the dimensionless length of the pump. From this relation, it can be seen that three conditions are necessary for $f(\tau)$ to be constant with time. These are:

(i) $(\tilde{P}_d - \tilde{P}_u)$ must be independent of time. This condition can be easily satisfied by constant pressure reservoirs.

(ii) H must be constant for all waves (e.g. periodic wave train)

(iii) L must be an integer number of wavelengths

With $f(\tau)$ equal to a constant, Equation (3-15) will also represent the pressure gradient in the finite-wavelength model. Integration of this expression over the entire pump length yields

$$\tilde{P}_d - \tilde{P}_u = - \int_0^L \left\{ \frac{1}{H^2} + (\theta - \bar{H}) \frac{1}{H^3} \right\} d\xi \qquad (3\text{-}18)$$

If L is equal to an integer number of waves and H is periodic, this expression can be rewritten as

$$\tilde{P}_d - \tilde{P}_u = - N \int_0^1 \left\{ \frac{1}{H^2} + (\theta - \bar{H}) \frac{1}{H^3} \right\} d\xi \qquad (3\text{-}19a)$$

or

$$\tilde{P}_d - \tilde{P}_u = N \, \Delta\tilde{P}_\lambda \qquad (3\text{-}19b)$$

where N represents the number of wavelengths between the upstream reservoir and the node with pressure P_N.

From (3-19b) it can be seen that the pressure distribution within the finite-wave-train experiment exhibits an interesting nodal type behavior at every wavelength along the pump. In other words, each node is acting as a local constant pressure reservoir within the pump.

Making use of this nodal property and integrating (3-15), the pressure variation at any position within the pump can be expressed

$$\tilde{P}(\xi,\tau) - \tilde{P}_N = N \, \Delta P_\lambda - \int_0^{\xi - N} \left\{ \frac{1}{H^2} + (\theta - \bar{H}) \frac{1}{H^3} \right\} d\xi \qquad (3\text{-}20)$$

For a sinusoidal wall shape, e.g.

$$H = 1 + \phi \sin 2\pi(\xi - \tau) \tag{3-21}$$

the pressure rise per wavelength ΔP_λ is equal to

$$\Delta\tilde{P}_\lambda = \frac{1}{2} \frac{\phi^2}{(1 - \phi^2)^{5/2}} [3 - (2 + \phi^2)\theta] \tag{3-22}$$

The solid curves in Figures 5, 6, and 7 represent the theoretical $\Delta\tilde{P}_\lambda$ vs θ curves for three values of ϕ(the experimental data will be discussed in Chapter 5). The maximum flow for zero pressure rise is defined as θ_0, and the maximum pressure rise for zero net flow is $\Delta\tilde{P}_{\lambda_{max}}$. The curves in Figures 8 through 11 represent the theoretical variation of pressure with time for three values of ϕ and for various values of ξ and θ. It should be noted that these curves do not correspond directly to the two-dimensional theory but relate to a modified theory which includes the geometry of the experimental apparatus. This modification, which will be discussed in detail in Section 3.4. and in Chapter 5, affects the magnitude of the pulse without altering its shape. The ordinate of the curves is the normalized pressure difference $\tilde{P} - \tilde{P}_0$. $\xi = 0$ represents the coordinate of the reference node. Time is represented on the x-axis, where $\tau = 0$ is the beginning of a wavelength and $\tau = 1$ is the beginning of the next wave. The experimental data in Figures 8 to 11 will be explained in Chapter 5.

Transformation of Variables. The unsteady laboratory reference frame can be transformed into a steady-state reference frame by means of the coordinate transformations below (refer to Figure 4b for the nomenclature in this transformed reference frame). In this reference frame, the viewer effectively moves with the wave.

$$\tilde{x} = \xi - \tau \qquad \frac{u}{c} = \frac{U}{c} - 1$$

$$\frac{y}{a} = \frac{Y}{a} \qquad \frac{v}{c} = \frac{V}{c} \tag{3-23}$$

The velocity profiles and pressure gradient expressed in the steady-state reference frame are:

$$\frac{u}{c} = -1 + \frac{3}{2}\left(1 + \frac{q/ac}{H}\right)\left[1 - \left(\frac{n}{H}\right)^2\right] \tag{3-24}$$

$$\frac{v}{c} = \frac{3}{2}\,\alpha\,\frac{dH}{d\tilde{x}}\left[\frac{q/ac}{H}\left(\frac{n}{H}\right) - \left(\frac{2}{3} + \frac{q/ac}{H}\right)\left(\frac{n}{H}\right)^3\right] \tag{3-25}$$

and

$$\frac{d\tilde{P}}{d\tilde{x}} = -\frac{1}{H^2} - \frac{q/ac}{H^3} \tag{3-26}$$

where the flow q is equal to

$$\frac{q}{ac} = \int_0^H \frac{u}{c}\,dn \tag{3-27}$$

By using the transformation relations and Equations (3-8) and (3-27) the flow can be written as

$$\frac{q}{ac} = \theta - \bar{H} \tag{3-28}$$

The transformed reference frame is in fact the wave reference frame described by Shapiro et al.[4]. In the analyses to follow, increasing use will be made of this steady wave reference frame.

Stream Function (Wave Reference Frame). In the laboratory reference frame the flow is unsteady, so the particle path lines (e.g. Figure 9 of Reference 4) are not necessarily related to the streamlines (e.g. Figure 4 of Reference 1). In the wave reference frame, the path lines, streamlines, and streak lines all coincide. These streamlines are similar to the wall shape, but with decreasing amplitude as the axis is approached; except, however, for certain cases where a region of closed streamlines are present. Some typical streamlines are shown in Figure 12.

In the steady wave reference frame the streamlines correspond to the particle trajectories, and can be used as a quantitative marker for identifying fluid particles. Defining the stream function by

$$d\psi = u\,dy - v\,dx \tag{3-29}$$

and using the velocity profiles described by (3-24) and (3-25), the normalized stream function ratio χ can be written as

$$\chi = \frac{\psi}{\psi_w} = -\frac{1}{2CH}\left[\eta(H - 3C) - \frac{\eta^3}{H^2}(H - C)\right] \tag{3-30}$$

where

$$C \equiv \bar{H} - \theta \tag{3-30a}$$

with $\tilde{\psi} = 0$ on the axis, the value of the stream function at the wall becomes

$$\tilde{\psi}_w = -C \tag{3-31}$$

Trapping. Under certain conditions of θ and ϕ, there are regions of the flow which contain closed streamlines[4]. When this phenomenon occurs, the center streamline splits, and a region of recirculating closed streamlines form (refer to Figure 12). This region comprises a bolus of fluid which, in the laboratory reference frame, appears to be "trapped" under the crest of the wave about the center line.

Limit of Trapping. The conditions of ϕ and θ in which trapping occurs can be determined directly from the solution of Equation (3-30). When trapping exists, the center streamline $\psi = 0$ must split to form the bounding streamline of the bolus. Before the onset of trapping, Equation (3-30) will have one real solution for η if $\psi = 0$, i.e. $\eta = 0$. At the onset of trapping, three real equal values of η will exist for $\chi = 0$, i.e. $\eta = 0$. Conceptually, this means that at the onset of the trapping the bolus will have zero volume. As the size of the bolus increases, the boundary of the trapped bolus can be obtained from the solution of Equation (3-30) for $\chi = 0$.

Using the above statement, trapping will occur when any non-dimensional wall coordinate H is

$$H \geq 3C \tag{3-32}$$

After onset of trapping the geometric boundary of the trapped bolus is defined simply by

$$\eta_T = H\left(\frac{H - 3C}{H - C}\right)^{1/2} \tag{3-33}$$

if $H \neq C$.

The criterion for trapping obtained by Shapiro et al.[4] reduces mathematically to

$$\frac{\theta}{\theta_0} \geq \frac{(2 - \phi)(2 + \phi^2)}{9\phi^2} \tag{3-34}$$

It can be shown quite easily that Equations (3-33) and (3-34) yield the same limit of trapping.

Peripheral Reflux. Simultaneous integration of the U and V components of velocity in the laboratory reference frame enabled Shapiro et al.[4] to obtain the particle trajectories within the peristaltic wave (e.g. Figure 9 of Reference 4). From these trajectories they were able to calculate the average speed of advance of each particle as a function of geometry and time mean flow. On the basis of the analysis they illustrated that under certain flow conditions the time average flow was composed of an algebraic sum of forward flow in the core of the pump and reverse of reflux flow near the walls.

In order to obtain a measure of the rate and quantity of reflux material, ψ is used as an indication of material particles, then the time-mean flow between the axis and a particular value of ψ is calculated. The instantaneous flow between the axis and the coordinate ψ can be expressed as:

$$Q = \int_0^{Y(\psi,\xi;\tau)} U(\xi,\eta,\tau)\,d\eta \tag{3-35}$$

Using Equation (3-24) and (3-30) the time-average flow beneath the particles identified by ψ becomes

$$\bar{Q}_{\psi} = \psi + \frac{c}{T}\int_{0}^{T} y(\psi,X,t)dt \qquad (3\text{-}36)$$

where T defines the wave period. Since the integral is evaluated at constant ψ and X, one can substitute $-\frac{1}{c}\,dx$ for dt. After non-dimensionalizing, Equation (3-35) can be rewritten as:

$$\theta_{\psi} = \tilde{\psi} + \int_{0}^{1} \eta(\tilde{\psi},\xi)d\xi \qquad (3\text{-}37)$$

Time-average flow is therefore the sum of the steady flow, as seen in the wave reference frame, and the time-average flow in one period if all the material in one wavelength between the axis and the streamline ψ were transported as a solid block with the wave speed c.

The integrand in Equation (3-37) is obtained numerically by solving the stream function relation (3-30) for η except for limiting cases of small ϕ, where a perturbation solution can be octained in closed form.

Figure 13 is a sketch showing the four general types of curves which can be obtained for $\bar{Q}_{\psi}/\bar{Q}_{w}$ vs χ.

Curve I represents a case where neither trapping nor reflux occurs.

Curve II is a representation of a case without reflux but with trapping. Point "a" represents the quantity of fluid trapped within the bolus region.

Curve III represents a case of reflux but no trapping. The quantity of fluid between the origin and point "b" represents

the time-mean forward flow in the core. ψ_b is the value of the stream function which divides the forward and reflux regions. The region between "b" and the terminal point of the curve represents the quantity of reflux flow. "$\mathcal{R}$" is the amount of reflux flow as a fraction of the net flow.

Curve IV defines the case where both reflux and trapping are present.

By comparing the values of ψ_b obtained from this analysis with the values of ψ_b obtained by Shapiro et al.[4], one can see both analyses yield the same results.

Reflux Limit. Even though the limit of reflux is discussed in great detail by Shapiro et al.[4], the technique employed will be briefly reviewed to facilitate the discussion of the reflux limit in Chapter 4.

By utilizing a perturbation solution about the point (1.1) in Figure 13 the stream function near the wall can be defined by a small parameter

$$\varepsilon = \tilde{\psi} - \tilde{\psi}_w \tag{3-38}$$

Assuming the wall can be expressed as a power series in ε the wall shape can be rewritten as

$$\eta(\xi,\phi,\theta,\varepsilon) = H + a_1\varepsilon + a_2\varepsilon^2 + \ldots \tag{3-39}$$

Introducing this relation and (3-37) into the stream function relation and solving for the coefficients a_1, a_2, etc., then applying (3-39)

into (3-37) results in the following value of flow rate near the wall for a sinusoidal wall shape.

$$\theta_\psi = \phi\theta - \frac{3}{2}\frac{\varepsilon^2(\phi\theta - \phi^2)}{(1 - \phi^2)^{3/2}} + \ldots \qquad (3\text{-}40)$$

Differentiation of this expression at the point $\theta = \theta_w$ and $\psi = \psi_w$ show the slope of the Q_ψ/Q_w curve to be equal to zero at the point (1.1). For reflux to occur θ_ψ must be greater than θ_w. This can only be the case if $\theta < \phi^2$ or if

$$\frac{\theta}{\theta_0} < \frac{2 + \phi^2}{3} \qquad (3\text{-}41)$$

Two-Dimensional Summary Curve. Figure 14 represents a graphic summary of the results obtained for the two-dimensional sinusoidal geometry[4]. The squeeze ratio is given on the abscissa; $\phi = 0$ represents no peristalsis and $\phi = 1$ represents complete occlusion. The ordinate represents the time-average flow ranging between $\theta = 0$ and $\theta = \theta_0$. The regions of reflux and trapping are shown for the case of zero Reynolds number*. Only the lower limit of trapping is shown in Figure 13 since the upper limit is outside the pumping range of the model (i.e. $0 > \theta > \theta_0$; $0 > \phi > 1$).

Reflux is quite common over most of the pumping range up to $\theta/\theta_0 = 0.7$ for small ϕ, and up to $\theta/\theta_0 = 1$ for complete occlusion.

---

*Refer to Reference 5 for the effects of Reynolds number and wave number.

Also plotted on these curves are the contours of constant reflux fraction "$\mathcal{R}$". For values of $\phi > 0.1$ the reflux fraction was found numerically using Equation (3-37) along with the interpretation of described in Figure 13 (solid line). For $\phi < 0.1$ an exact solution (dashed line) for reflux fraction was obtained (both solutions are represented on Figure 11).

The reflux fraction is quite small when θ/θ_0 is greater than 0.5; yet, as θ/θ_0 decreases, $\mathcal{R}$ approaches infinity since θ_0 approaches zero. Since the reflux flow remains finite, the absolute non-dimensional value of θ_R is shown in Figure 15 as a function of ϕ where the value of reflux flow is defined by

$$\theta_R = \theta_{max} - \theta \tag{3-42}$$

3.3. Basic Formulation (Axisymmetric Geometry)

Only the relations necessary for a later discussion of ureteral function will be developed in this section. The basic formulation and conclusions are similar to the two-dimensional case, so detailed discussion will not be included (see Reference 4 for the detailed analysis). The nomenclature used in the axisymmetric geometry is also included on Figure 4.

Integration of the governing equations in the wave reference frame and subsequent transformation to the laboratory reference frame leads to the following velocity profiles

$$\frac{U}{c} = 2\left(1 + \frac{q/\pi a^2 c}{H^2}\right)\left[1 - \left(\frac{\eta}{H}\right)^2\right] \tag{3-43}$$

and

$$\frac{V}{c} = \alpha \frac{\partial H}{\partial \xi} \left[2 \frac{q/\pi a^2 c}{H^2} \left(\frac{\eta}{H}\right) - \left(1 + 2 \frac{q/\pi a^2 c}{H^2}\right) \left(\frac{\eta}{H}\right)^3 \right] \tag{3-44}$$

where

$$\frac{q}{\pi a^2 c} = \int_0^{H^2} \left(\frac{U}{c} - 1\right) d(\eta^2) \tag{3-45}$$

The local pressure gradient becomes

$$\frac{\partial \tilde{P}}{\partial \xi} = - \frac{1}{H^2} - (\theta - \overline{H^2}) \frac{1}{H^4} \tag{3-46}$$

Using the following form for the Stokes' stream function

$$d\psi = u\, r\, dr + v\, r\, dx \tag{3-47}$$

the stream function ratio can be written as

$$\chi \equiv \frac{\psi}{\psi_w} = - \left[\frac{M + H^2}{2H^4} \right] \frac{2}{M} \eta^4 + \left[\frac{2M + H^2}{2H^2} \right] \frac{2}{M} \eta^2 \tag{3-48a}$$

where

$$M \equiv \frac{q}{\pi a^2 c} = \theta - \overline{H^2} \tag{3-48b}$$

The value of the stream function at the wall

$$\tilde{\psi}_w = \frac{M}{2} \tag{3-49}$$

if $\tilde{\psi} = 0$ on the axis.

The pressure variation with time can be written as

$$\tilde{P}(\xi,\tau) - \tilde{P}_0 = \int_0^{\xi} [\frac{1}{H^2} + (\theta - \overline{H^2}) \frac{1}{H^4}] d\xi \qquad (3\text{-}50)$$

For the case of a sinusoidal wall shape the pressure rise per wavelength $\Delta\tilde{P}_\lambda$ from Reference 4, is given as

$$\Delta\tilde{P}_\lambda = \frac{16\phi^2(1 - \frac{\phi^2}{16}) - 8\phi(1 - \frac{\phi}{4})(1 - \frac{3}{2}\phi^2)\theta}{(1 - \phi^2)^{7/2}} \qquad (3\text{-}51)$$

where

$$\Theta = \frac{\theta}{(2\phi - \phi^2/2)} \qquad (3\text{-}51a)$$

Trapping Limit. In the axisymmetric geometry, the splitting of the central streamline can also be used to identify the onset of trapping.

In the axisymmetric geometry the stream function is a biquadratic equation in η. Before trapping is initiated only one real value of η can exist for $\chi = 0$, i.e. $\eta = 0$. At the initiation of trapping all values of η will be real and equal to zero. As the trapping bolus grows, two roots will remain equal to zero while the remaining positive root will define the boundary of the trapped zone, i.e. $\eta = \eta_t$. However,

$$0 < \eta_t < H \qquad (3\text{-}52)$$

The lower limit of trapping is defined by the following relation

$$H = (-2M)^{1/2} \tag{3-53}$$

where M is defined by Equation (3-48b).

As the trapped bolus grows, the boundary is defined by

$$\eta_T = \left[\frac{(2M + H^2)}{(M + H^2)}\right]^{1/2} H \tag{3-54}$$

if $M \neq H^2$.

Shapiro et al.[4] obtain the trapping criteria in the following form

$$\frac{\theta}{\theta_0} \geq \frac{(1 - 2\phi)(2 + 3\phi^2)}{(16 - \phi^2)\phi^2} \tag{3-55}$$

Again as in the two-dimensional case, the results can be demonstrated to be equivalent.

Reflux. For the axisymmetric geometry the quantity of dimensionless time-mean flow below any material particle ψ can be expressed as

$$\theta_\psi = 2\tilde{\psi} + \int_0^1 \eta^2(\tilde{\psi}, \xi)\, d\xi \tag{3-56}$$

Reflux Limit. Using techniques similar to those employed in the plane geometry, the reflux limit is identically equal to $\theta/\theta_0 = 1$, i.e. for all values of flow, reflux will be present except at $\theta = \theta_0$.

Axisymmetric Summary Curve. Figure 16 is the summary curve for the axisymmetric geometry. With ϕ as the abscissa and θ/θ_0 as the ordinate, the limits of trapping and reflux are shown along with the contours of constant reflux fraction. As in the two-dimensional case $\mathcal{R}$ was obtained numerically for $\phi > 0.1$ and in closed form for $\phi < 0.1$.

Figure 17 is a representation of the reflux flow θ_R for θ/θ_0 equal to zero.

3.4. Three-Dimensional Channel Effects

The apparatus, although approximately two-dimensional, has a rectangular cross section with inactive end walls. For this reason, it is important to consider the effect of these end walls in the theory.

Basically, the pumping duct can be considered as a rectangular channel of constant height with varying aspect ratio. The two-dimensional theory can be simply modified using an approximate technique described by Purday[15]. With this approximation the two-dimensional pressure gradient (Equation 3-15) becomes†

$$\frac{\partial \tilde{P}}{\partial \xi} = \frac{\int_0^1 \frac{n}{n+1} H \, d\tau - \theta^*}{\int_0^1 \frac{n}{n+1} \, d\tau} \left(\frac{\frac{n+1}{n}}{H^3} - \frac{\frac{n+1}{n}}{H^2} \right) \qquad (3\text{-}57)$$

where θ^* is the actual non-dimensional half-width flow per unit height of channel, and $n(\xi,\tau)$ is a function of aspect ratio as determined by

---

†Refer to Appendix B for the details of this analysis.

$$n^2(x,t) + n(x,t) = \frac{w^2}{2h^2} \tag{3-58}$$

Here w is the height of the channel and $2h(\xi,\tau)$ is the local gap width. In the extreme case of $\phi = 0.9$, the value of n for the experiment (see Chapter 5) ranges between 13 at the wide section to 27 in the contracted region. More will be said in Chapter 5 concerning this modification and the comparison of the results thereof with experimental results.

4. URETERAL MODEL

The physiological information presented in Chapter 2, coupled with the concepts and relations developed in Chapter 3, provide a platform upon which a theoretical model of ureteral function can be constructed. As will be shortly demonstrated, the ureteral model can be considered as an extension of the infinite-wave-train analysis.

4.1 Basic Assumptions

Since the analysis presented in Chapter 3 was based upon assumptions which are also relevant to the ureter, i.e.:

(i) the long-wave-length approximation

(ii) neglecting of the inertial forces

(iii) constant viscosity and density,

the governing equations of Chapter 3 will be valid for the ureteral model.

Little is known regarding the detailed physiology of the ureteropelvic and ureterovesical junctions. What is known, however, indicates that entry and exit of a peristaltic wave from the ureter does not affect the character of the urometric pressure pulse.

In the ureteral analysis it will be necessary to consider passage of a solitary wave. However, as long as the velocity and pressure fields are prescribed distal and proximal to a wave, the theoretical approach will be analogous to that prescribed in Chapter 3.

Along with the foregoing assumptions, additional constraints will be placed on the theoretical model which relate directly to urometric

observations. These constraints do not alter the theoretical presentation of Chapter 2 but place restrictions on the values of certain of the variables.

In the case of a ureteral wave, the conditions at both ends of a wave are well documented. From Chapter 2, the wave was shown to have a negligible pressure rise across it as compared with the peak pressure, i.e. $\Delta P_\lambda \tilde{=} 0$. This condition seems to exist within the ureter, as indicated by Figure 18a, which is a sketch of a typical physiological pressure pulse taken from Kiil[8]. Figures 18b and 18c display the character of pressure pulses if $\Delta P_\lambda < 0$ and $\Delta P_\lambda > 0$, respectively. Since neither of the latter two cases are observed urometrically in normal ureters, the pressure rise across a wave must be approximately equal to zero.

A second constraint on the model requires that the fluid remain motionless between individual preistaltic waves (i.e. $U = V = 0$ in the resting ureter). In fact, if fluid velocities did occur within the inactive ureter, urine would enter the bladder continuously. Moreover, there would be pressure gradients ahead of, and behind, the peristaltic wave, in opposition to clinical observations.

One important conclusion can be drawn from the preceding paragraphs. Each ureteral wave can be considered independent of any proximal or distal wave. As long as an inactive or resting length of ureter separates each peristaltic wave and $\Delta P_\lambda \tilde{=} 0$, each individual wave can have its own pressure pulse, spurt volume, and geometry.

4.2. General Formulation (Circular Lumen)

Since the ureteral lumen, during various phases of dilation, must approach an axially-symmetric cross section, it is necessary to consider the fluid mechanics for such a shape.

Ureteral catheters presently used must affect the size and shape of the ureteral lumen. Since the outside diameter of the catheter is approximately equal to the distended diameter of the lumen, the axisymmetric model should yield some insight into the effects of the catheter, at least to a first approximation.

When considering the solitary ureteral wave in the wave reference frame, the constraint on the flow field in the resting ureter places a restriction on the steady wave frame flow q. In the laboratory reference frame U = 0; whereas, in the wave reference frame u = -c in the inactive ureter. For this reason q must be constant at all sections and equal to

$$q = -\pi a^2 c \tag{4-1}$$

where a is the radius of the resting ureter.

By using Equation 23 from Shapiro et al[4], which may be written as

$$\frac{Q}{\pi a^2 c} = \left(\frac{h}{a}\right)^2 + \frac{q}{\pi a^2 c} \quad , \tag{4-2}$$

together with Equation (4-1), a simple but important fact regarding the flow field can easily be seen. The instantaneous flow Q will be positive only if the radial position of the wall is greater than the

resting radius, i.e. h > a, and will be negative for h < a. Knowing that the flow is locally Poiseuille, the pressure gradient will be negative if h > a and positive if h < a. This point will be made clearer in the discussion of the pressure gradient to be presented later.

Taking the time average of Equation (4-2) and using Equation (4-1) the dimensionless time-mean flow can be expressed as

$$\theta = \overline{H^2} - 1 \tag{4-3}$$

where $\overline{H^2}$ is the wall position squared when averaged over a wave length. In other words, in order for a ureteral wave to carry a net positive flow rate, $\overline{H^2}$ must be greater than unity.

Using Equation (4-3), all the relevant equations presented in Chapter 3 can be modified to pertain to the solitary ureteral wave.

The pressure gradient within a wave, which can be obtained from Equations (3-46) and (4-3), is equal to

$$\frac{\partial \tilde{P}}{\partial \xi} = \frac{(1 - H^2)}{H^4} \tag{4-4}$$

As was indicated above, the pressure gradient will be positive or negative depending upon the value of H, i.e. $\partial \tilde{P}/\partial \xi > 0$ if $H < 1$ and $\partial \tilde{P}/\partial \xi < 0$ if $H > 1$.

Wave Shape. If the actual wave shape were known within the ureter, Equations (4-3) and (4-4) would directly yield the associated pressure pulses and spurt values which could then be compared with urological observations. However, because of insufficient data, it is necessary

to use an inverse procedure: i.e. to determine from physiological data a wave shape which is consistent with the theoretical model.

To this end, a typical urometric pulse can be used to yield the general form for the ureteral wave. Distinction must first be made between a length-varying pressure pulse at constant time which can be obtained from Equation (4-4), and a time-varying pressure pulse at a fixed location which is obtained urometrically.

Figure 19a represents an arbitrary wave shape at any instant of time. Using Equation (4-4) the associated instantaneous curve of pressure vs distance is shown in Figure 19b. However, if a catheter is placed at a fixed location, the pressure pulse, which would be recorded against time, is shown in Figure 19c. From the length-varying pressure pulse the positive pressure gradient is associated with the contracted region, and the negative gradient is related to the dilated region. In the time-varying pressure pulse the reverse is the case, i.e. the positive gradient occurs within the dilated region and the negative gradient occurs within the contracted region.

Examination of typical ureteral pressure pulses, e.g. Figure 3 or Figure 31, shows that $\partial P/\partial \tau$ is first positive then negative. Considering the concepts just presented, the ureteral wave must be composed of a dilated region ($H > 1$) followed by a contracted region ($H < 1$). It should be noted that radiographic and visual observations support this conclusion.

The choice of a particular wave shape is not critical to the understanding of ureteral fluid mechanics as long as the wave shape is consistent with the general form as dictated by the shape of the

pressure pulse. From urometric data it appears as if the wave shape varies between successive waves and between individuals. For these reasons a stepped or square wave shape is chosen because it leads to simple calculations and a simple understanding of ureteral fluid mechanics.

It is obvious that this geometry cannot simulate the smoothly-varying shape of the ureter; however, as will be shown later, it is a good approximation to the smooth geometry.

The particular wall shape which will be used in this analysis is illustrated in Figure 20a. The shape consists of a contracted region of uniform cross section ($H_1 < 1$) and a two-stage dilated region. The first, which is designated the transition region, has a uniform radius of the same order as the resting radius ($H_2 \gtrsim 1$). The second dilated stage or bolus region has a uniform radius much greater than the resting radius ($H >> 1$).

Pressure Pulses. Figure 20b represents the triangular shaped pressure pulse which is obtained from this stepped wave. This pulse is a reasonable approximation to the urometric pulses (see Figure 3). The pressure rise per wave length is the sum of three pressure differences, i.e. ΔP_1, ΔP_2, ΔP_3. Each pressure difference can be expressed as

$$\Delta P_i = \ell_i \left(\frac{\partial P}{\partial X}\right)_i \qquad (4\text{-}5)$$

where the subscript i refers to the various regions.

A great deal of information concerning the amplitude and shape of the pressure pulse can be extracted directly from the character of the pressure gradient as can be seen from Figure 21. Increasing the squeeze, i.e. reducing H_1, results in a continuously increasing pressure gradient. However, as H increases beyond unity, as will be the case in both dilated regions, the pressure gradient is bounded by a minimum value. For the axisymmetric geometry, this limiting value occurs at a value of $H = \sqrt{2}$.

As the radius of the dilated region increases, the magnitude of the pressure gradient approaches zero. Since the size of the bolus is much greater than unity, the pressure gradient within the bolus will be approximately equal to zero or $\Delta P_3 \cong 0$. In other words, no major pressure variations will be associated with the bolus region of the wave. For this reason, the major ureteral pressure variations will be associated with the transition and contraction regions of the wave. Since the pressure rise per wave length must be equal to zero and $\Delta P_3 \cong 0$, the value of $\Delta P_1 = -\Delta P_2$. Therefore, the maximum pressure rise within a wave is restricted by ΔP_2 even though ΔP_1 is without limit.

This fact leads to an interesting disclosure. With this model the peak pressure will occur at the transition point between the contraction and transition regions which lags the passage of the bolus by ℓ_2/c seconds. As previously noted, Barry et al[13] reported such a time lag between passage of the bolus over the tip of the catheter and the peaking of the pressure pulse.

A closer comparison can be made between the theoretical pressure pulse and the physiological pressure pulse if a more realistic wave shape is chosen. Figure 22 is a sketch showing one possible continuous wave along with the mathematical relations describing its shape. With the continuous geometry, the end of the transition region is arbitrarily chosen as the point where the pressure gradient is about 5% of the maximum pressure gradient.

Using the continuous wave shape of Figure 22, Equation (4-4) can be integrated to yield the time-varying pressure pulse. Figure 23 includes several pressure pulses for various geometries along with a typical urometric pulse obtained by Kiil[8]. In all cases the pulses are similar to the physiological pulse. By proper choice of wall shape, the theoretical pulse can be made to duplicate the urometric data.

Effect of Catheterization. The general formulation for the introduction of a non-occlusive catheter is shown in Appendix B. The analysis considers the presence of a catheter of radius r_c which is introduced into an axisymmetric ureter. In the analysis, it is assumed that the presence of a catheter does not affect the wall shape or dimensions. It is obvious that the shape of the ureteral wave must change when a catheter is inserted; however, as a first approximation, the analysis will yield the potential effects of the catheter.

The effects of the catheter on the urometric pulse can be seen in Figure 24, which is a graphical representation of the pressure gradient as expressed in Figure (B-5). The general shape of the pressure gradient curve remains unchanged as catheter size is increased;

however, the magnitude of the pressure gradient is severely affected. Since the peak pressure within a wave is limited by the magnitude of the maximum negative gradient within the transition region if $\Delta P_\lambda = 0$, the peak pressures within the catheterized ureter will be greater than that of the non-catheterized ureter for the same geometric variables (L_1, L_2 and H_2).

The qualitative shape of the pressure pulse with the square wall model will remain unaffected by introduction of a catheter, i.e. the peak pressure will still lag passage of the bolus and the pressure variation within the bolus will be small.

Qualitatively, the introduction of a catheter has a small effect on the pressure pulse produced by the continuous wall shape of Figure 22. To strengthen this point, Figure 23 also includes a pressure pulse produced from the catheterized model.

Reflux. To investigate the characteristics of the reflux phenomenon within a ureteral wave, the method of calculation previously developed in Chapter 3 will be employed..

The time-mean flow between the axis and a streamline in the wave frame can be calculated using Equation (3-42) and (3-35) along with Equation (4-3). The results are similar in character to those presented in Chapter 3.

One can solve for the reflux limit in a manner analogous to that presented in Section 3.3. The stream function can first be defined by Equation (3-38) then used to define the wall position in povers of ε as was shown in Equation (3-39). Substituting this relation into Equation (3-37) along with the appropriate value of the stream function,

then solving for the constants allows the flow near the wall to be written in a form similar to Equation (3-40). Since θ_ψ must be greater than θ_w, the general condition of reflux in the ureteral model can be written as

$$\int_0^1 \left(\frac{1}{H^4} - \frac{1}{H^2}\right) d\xi > 0 \qquad (4\text{-}6)$$

Since $\Delta P_\lambda = 0$ in the ureter, Equation (4-4) can be integrated to yield the following relation for the pressure rise per wave

$$\int_0^1 \left(\frac{1}{H^4} - \frac{1}{H^2}\right) d\xi = 0 \qquad (4\text{-}7)$$

Comparison of Equation (4-6) and (4-7) leads to the important conclusion that, with the axisymmetric cross section, reflux cannot occur if $\Delta P_\lambda = 0$. However, for any $\Delta P_\lambda > 0$ reflux might be present.

Displacement Profiles. In the wave reference frame, fluid particles move thru the wave along particular stream lines. The time each particle takes to pass through the wave will be designated as its residence time τ_p. In the wave reference frame, the non-dimensional residence time of the particle on the stream line ψ equals

$$\tau_p = \int_1^0 \frac{d\tilde{x}}{\left(\frac{u}{c}\right)_\psi} \qquad (4\text{-}8)$$

$(u/c)_\psi$ is the local-wave-frame velocity of the particle ψ.

Initially, i.e. at $\tau = 0$, all particles will be located at $\xi = 1$. In the laboratory reference frame the particles are carried within the wave for a time equal to the residence time. To clarify this point consider the following: if, in the wave reference frame, a particle takes one wave period to pass thru the wave then, in the laboratory frame the wave has progressed one period. Therefore, if a particle were initially at $\xi = 1$ at $\tau = 0$, then after the wave moves one period the particle will still be at $\xi = 1$.

When τ_p is greater than unity, the wave will progress more than one period before the particle exits the wave, leaving the particle with a net forward displacement, i.e. $\xi > 1$. If, on the other hand, τ_p is less than unity the wave will have a final position less than $\xi = 1$ placing it in the reflux region.

With trapping present, particles within the bolus and particles along the center streamline cannot pass through the wave. However, particles off the axis will have definite residence times.

At $\tau = 0$ a transverse line of particles can be marked at $\xi = 1$. Once particles pass through the wave their position will not change with time since they will be in the inactive ureter ($U = 0$). If one waits until all particles have passed through the wave, a curve may be drawn through their final positions. This curve will be designated as the net displacement profile.

Figure 25a is a series of displacement profiles obtained for various geometrics. Curves I, II and III do not show any indication of reflux, as should be expected, since these geometries yield a zero pressure rise per wave. If the constraint of $\Delta P_\lambda = 0$ is relaxed, a

profile can be obtained which clearly indicates the existence of reflux along the walls(curve IV).

Trapping. The limit of trapping for the axisymmetric ureteral wave can be obtained by a substitution of Equation (4-3) into Equation (3-53). This expression becomes

$$H \geq \sqrt{2} \tag{4-9}$$

This means that a trapped bolus will exist beneath any position of a wave that has a radius greater than $\sqrt{2}$.

Summary Curve. With the ureteral wave, a summary curve can be drawn showing the regions of reflux and trapping as a function of geometry. A particular curve will exist for each L_1, L_2, L_3, and H_3, but Figure 26 only illustrates the case where $L_1 = .441$, $L_2 = .441$, $L_3 = .118$ and $H_3 = 25$. These particular values were chosen since they are comparable with physiological data. More will be said regarding these dimensions in the next section.

With L_1, L_2, L_3 and H_3 defined, the two remaining variables, i.e. H_1 and H_2, will be used as the x and y axes, respectively. Displayed on this figure are the limits of reflux and trapping. The curve showing the loci of geometries yielding $\Delta P_\lambda = 0$ is concurrent with the limit of reflux.

Comparison with Physiological Data. In the physiological literature three facts are well documented and will be used to determine the validity of the ureteral model, i.e., the qualitative shape of the

pressure pulse, the magnitude of the peak pressure above basal level, and the fluid carried within a wave (spurt voluem).

Several points pertaining to the qualitative shape of the pressure pulse have been discussed previously. With both the square wall and continuous wall shapes, the general shape of the pressure pulse is similar to the urometric data. In fact, since the peak pressure occurs between the transition and contraction regions the theoretical model predicts the delay observed by Barry et al[13] between passage of the bolus and the peak pressure. Because of the large radius of the bolus, as compared with the resting radius, small pressure variations occur within the bolus region.

In comparing the theoretical model with urometric data it would be of interest to study the variation of non-dimensional peak pressure as a function of the relevant geometric parameters for $\Delta P_\lambda = 0$, i.e. L_1/L_2 and H_2. The corresponding value of H_1 can be determined from Figure 26. A plot of $\tilde{P}_{max} - \tilde{P}_{basal}$ is shown in Figure 27. $L_1/L_2 = 3/7$ and $L_1/L_2 = 7/3$ depict the limiting values of L_1 and L_2 which have physiological relevance. The peak pressure is bounded at $H_2 = 1.5$, as could be expected, since the pressure gradient within the transition regions limits the peak pressure.

The fluid carried within a ureteral wave is related to the time mean flow through the following relation.

$$Q_U = \pi a^2 c \cdot \frac{\lambda}{c} \cdot \theta \qquad (4\text{-}10)$$

Equation (4-10) can be used along with Equation (4-3) to determine the spurt volume within the axisymmetric ureteral wave.

At this point it would be helpful to consider a few possible geometries and illustrate the spurt volumes and peak pressures carried by these waves. Table 1 is a representation of a series of square wall configurations. Because of the large number of variables, certain of the parameters were held constant including the wave speed c = 3 cm/sec and the viscosity μ = .01 Poise.

The value of resting diameter was chosen so that the peak differential pressure ($P_{max} - P_{basal}$) would be within the physiological range. Variation in resting diameter has a strong influence on peak pressure since the pressure is inversely proportional to a^2.

The value of bolus diameter was also held constant since within the ureter the lumen is most likely circular and constant in diameter along the length of the bolus.

With the bolus and resting diameters held constant, the length and diameter of the contracted and transition regions can be varied. Certain facts, previously discussed, now become evident: First, the values of the peak pressure are independent of the dimensions of the bolus region and depend only on the dimensions of the contraction and dilated regions. Second, the fluid carried within a wave is only a function of bolus size and is not affected by the details of the pressure pulse. Finally, the diameter within the contracted ureter is approximately equal to the resting diameter. This fact seems to be substantiated by radiographic studies which showed that the bulk of the fluid transport is related to the bolus region, while the resting, transition, and contracted regions of the ureter appear to be void of urine. Since the dimensions within the contraction and transition regions are very

small (0.1 mm), radiographic techniques would be unable to detect the presence of urine.

With the geometries chosen in Table 1, the time lag between passage of the bolus and the peak pressure ranges between 1.1 and 4 seconds.

Because of the large diameter of the bolus, i.e. $H_3 = 25$, trapping will exist within this region of the wave. The presence of trapping within the transition region of the wave depends on the actual geometry of the region.

4.3. General Formulation (Lobe-Shaped Lumen)

From Figure 2 it can be seen that the ureteral lumen can form a quasi-lobe-shaped geometry at least in the resting ureter. Since the actual geometry is quite complicated a lobe-shaped model can be constructed which includes the major characteristics of the ureter. The following sketch based on Figure 2 shows a cross-sectional shape consisting of six lobes each having a width 2h, where h is the transverse coordinate of the wall relative to the center line of each lobe.

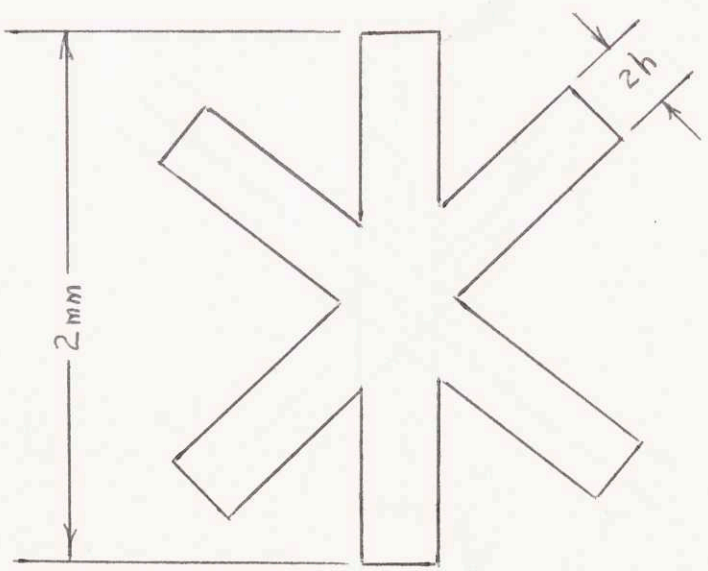

The overall dimension was chosen to be 2 mm since the ureteral lumen is approximately equal to this value. If we neglect the center core, the cross-sectional geometry can be considered as 6 parallel two-dimensional channels.

The general formulation is analogous to the circular formulation presented in Section 4.2. Because of the similarity between the circular and lobed models the discussion will be brief and only the important relations will be touched upon.

Since no fluid motions exist except within the active wave regions, the wave frame flow q, i.e. the flow per unit height in one-half of a two-dimensional lobe, must equal

$$q = -ac \tag{4-11}$$

Using this relation along with mean-flow rate as defined by Equation (11) of Reference 4, the mean-flow carried by a two-dimensional ureteral wave is related to the average position of the wall by the following relation.

$$\theta = \overline{H} - 1 \tag{4-12}$$

In other words, the average dimensionless wall coordinate $\overline{H}$ must be greater than unity if the wave is to have net positive flow rate.

The dimensionless pressure gradient within the lobe-shaped wave can be obtained by substituting equation (4-12) into Equation (3-15). This relation can be written as

$$\frac{\partial \tilde{P}}{\partial \xi} = \frac{(1 - H)}{H_3} \tag{4-13}$$

This expression can be integrated to yield the pressure variation within the wave.

Because of the similarity between Equations (4-13) and (4-4) the general shape of the wave must be composed of a dilated region followed by a contracted region. With the square wall shape, the wave will still consist of three regions and have a triangular pressure pulse as shown in Figure 20.

Equation (4-13) can be plotted against wall position in order to show the character of the pressure gradient in various regions of the wave (see Figure 21). The general shape of the pressure gradient curve is similar to the axisymmetric curve in that they both have a lower bound for the pressure gradient when $H > 1$. The bound occurs at $H = 1.5$ with the lobe-shaped geometry. One can also see that the magnitude of the pressure gradient is always less than the axisymmetric pressure gradient. This means that for the same basic geometric configuration, the peak pressure in the two-dimensional wave will be less than the peak pressure in the circular ureter. Alternatively, with the lobed cross section a smaller value of "a" is required to place the peak pressure within the physiological range.

Reflux and Trapping. Using a pertibation solution similar to the one discussed in Chapter 3 and in Section 4.2, the condition for reflux with the lobe-shaped geometry can be written as

$$\int_0^1 \left(\frac{1}{h} - \frac{1}{H^2}\right) d\xi < 0 \qquad (4\text{-}14)$$

Using Equations (3-30a) and (3-32) along with Equation (4-12) results in the following criteria for trapping.

$$H > 3 \tag{4-15}$$

If the value of the wall coordinate h is greater than three times the resting coordinate "a", a trapped bolus will exist below that portion of the wave.

With $H_3 = 10$, $L_3 = .118$, and $L_1 = L_2 = .441$, a summary curve can be constructed showing the regions of reflux and trapping as a function of H_1 and H_2. Here again, an infinite family of geometric configurations exist for $\Delta P_\lambda = 0$, but only a relevant set of parameters was chosen for display. Also shown on this figure are the values of H_1 and H_2 which yield $\Delta P_\lambda = 0$. From this curve it can be seen that reflux will not exist when $\Delta P_\lambda = 0$.

Displacement Profiles. Net particle displacement profiles can be constructed for the lobe-shaped geometry by using Equation (4-8) along with the two-dimensional velocity profiles and stream function. Curves I, II, and III of Figure 25b show a series of displacement profiles for geometries where $\Delta P_\lambda = 0$. Curve IV shows a profile where the constraint on ΔP_λ was relaxed in order to illustrate a reflux condition.

Comparison with Physiological Observations. By summing the flow from each of the 6 lobes a relation can be developed between the spurt volume Q_U and the mean-flow rate defined by Equation (4-12). This relation can be written as

$$Q_U = 1.2\ ac \cdot \frac{\lambda}{c} \cdot \theta \qquad (4\text{-}16)$$

The general character of the peak pressure within a stepped wave is shown graphically in Figure 29. Since the major pressure variations are associated with the contraction and transition regions, only H_2, L_1 and L_2 are displayed as variables. As with the circular geometry, the two curves depict the limiting values of the longitudinal coordinates which have physiological significance. The value of H_1 corresponding to each value of H_2 can be obtained from Figure 28 when $\Delta P_\lambda = 0$.

Using Figure 28 along with Equations (4-16) and (4-12), Table 2 can be constructed showing the spurt volumes and peak pressures for various geometries for which $\Delta P_\lambda = 0$. As with the circular geometry, the spurt volume is related to the bolus region; while, the pressure pulse is related to the contraction and transition regions. As was mentioned previously, the value of resting lobe width required to place the peak pressure within the physiological range is less than required for the circular geometry, i.e., 0.056 mm as compared with 0.1 mm, respectively. With all geometric configurations, wave speed and viscosity were constants and equal to 3 cm/sec and .01 Poise, respectively.

4.4. Combination of the Lobed and Circular Geometries. The ureteral lumen is not entirely circular or lobe-shaped, in fact, the shape most likely varies between circular in the bolus region and lobe-shaped in the resting, contracted, and transition regions.

As a first approximation, one can consider the cross section within the wave to suddenly change from circular to lobe-shaped at the end of the bolus region. In actuality, a continuous transition must exist; however, the conclusions formulated using the sudden transition model will yield some insight into the smooth transition. The general wave shape and nomenclature will be similar to the wave shapes presented in Figure 20 and 22 except H_3 will be radial while H_2 and H_1 will be the transverse coordinate "Y".

From the discussions presented in Sections 4.2 and 4.3, the effects produced by a combination geometry will be straight forward. It has been shown that the major fluid transport is associated with the bolus region of the wave, while the pressure pulse is related to the transition and contraction regions. Since the spurt volume and pressure pulse are independent, each quantity can be calculated for its appropriate geometry, i.e. the pressure pulse from two-dimensional theory and the spurt volume from the axisymmetric theory. In calculating actual numerical values of pressure and fluid transport, care must be taken to match the instantaneous flow rate Q on either side of the cross-sectional discontinuities.

4.5. Summary Comments on the Ureteral Model. As was illustrated in Tables 1 and 2, either the lobed or circular geometry can account for peak pressures and spurt volumes within the physiological range. A combination of the geometries, which is most likely the case within the ureter, will also yield reasonable results.

The ureteral wave is composed of a urine carrying region, where trapping is most likely present, followed by a contracted region which

is responsible for the pressure pulse. Conceptually, the ureter operates with a type of "milking action" where the urine is transported in front of a pressure cuff which is formed by the contraction and transition regions of the wave.

Along the ureter, large pressure variations are not required to transport urine, in fact, peak pressures 1/100 as large will be as effective. However, in order to expel urine into a pressurized bladder, peak pressures greater than intra-vesical pressures are required. If these peak pressures were less than the bladder pressure, a small regurgitation of urine into the ureter will occur as the ureterovesical junction opens.

The actual internal dimensions of the ureter during passage of a wave are not determined exactly from the analysis; however, the range of these dimensions is indicated. If the urometric pulses are true recordings of intra-lumenal pressure, i.e. not artifact caused by the catheter, dimensions of 0.1 mm or less are required within the resting and contracted regions of the ureter. Because of the large size of the bolus as compared with the other dimension, the ureteral wave would appear visually as a single dilated region followed by a single contracted region. Radiographic data appears to confirm this conclusion.

From the analysis, the presence of a catheter appears to have small effect in the qualitative shape of the pressure pulse, but does severely affect the magnitude of the peak pressure. As was expected, the magnitude of this effect depends on the size of the catheter as well as the accomodation of the lumen to the catheter.

The model also presents a possible interpretation of the observed time lag between the passage of the bolus and the peak pressure.

Gravity will have little effect on ureteral function as long as the ureterovesical junction effectively isolates the ureter from the bladder. When the ureter is vertical, an additional ρgh static head will be present within the ureter.

Analytically, it appears as if retrograde urine transport will not be present in normal ureters since the pressure rise across a wave must be greater than zero for reflux to occur. However, it might be present when alterations of wave shape occur. With refined physiological techniques, it might be possible to identify the presence of reflux by urometric techniques.

5. EXPERIMENTAL PROGRAM

5.1. Introduction

In Chapter 1 various theoretical treatments of peristaltic pumping were mentioned; however, adequate experimental confirmation of these theories does not exist.

The experimental program described in this chapter was developed to yield both quantitative and qualitative information on peristaltic pumping at Reynolds numbers where the fluid could be considered inertia-free. The visual experiments were designed to determine the operating conditions for which the phenomena of reflux and trapping are present.

Pressure studies included an investigation of the pressure rise per wave length and the pressure variation within a wave as a function of ϕ and θ.

Previously, T. Latham[19] constructed a quasi-two-dimensional apparatus with which he obtained the integral pumping characteristics, i.e. $\tilde{\Delta P}_\lambda$ vs θ, for a range of Reynolds numbers. For $R < 0.2$ his results substantiated the linear nature of the $\tilde{\Delta P}_\lambda$ vs θ curves, as predicted by Shapiro et al[4]. Latham's apparatus was modified by S. Weinberg and E. Eckstein in (1965) to allow for limited flow visualization. The results confirmed the existence of reflux near the walls, but the work was not published because no reliable quantitative data could be obtained with the apparatus.

5.2. Description of Apparatus

Figure 30 is a schematic diagram showing the major components of the fluid circuit. The peristaltic pump is located between two open reservoirs, each of which is composed of a lower transition chamber, which will be discussed later, and an upper tank. The upstream tank had a cross-sectional area of 1 ft^2 and a height of 1 ft, while the downstream tank had the same area but a height of 2 ft.

The fluid level in the upstream tank was maintained at P_0 by use of an over-flow pipe which was located within the reservoir. The fluid over-flow from the upstream reservoir was returned to a sump tank which was located beneath the pump.

The downstream reservoir had an adjustable over-flow pipe which was used to set the pressure level, P_L. The over-flow from the downstream reservoir passed into a three-way diverter valve. It was then diverted into a graduate for flow rate measurements or allowed to return to the sump tank for recirculation.

Manometers, which were attached to each reservoir, were used to monitor the fluid levels within the reservoirs.

A variable speed gear pump, which was located beneath the sump tank, continuously supplied the fluid to the upstream reservoir. All conduit, external to the peristaltic pump, was 1 1/2 in. I.D. vinyl tubing, except for 1 in. I.D. tubing between the gear pump and upstream reservoir.

Various mixtures of glycerine and water were chosen as the working fluid because of the large range of attainable viscosities (i.e. from

1 centipoise (cps) to 500 cps) and the transparent character of the mixtures. The latter requirement was necessary for visualization studies.

A top view of the peristaltic pump is sketched in Figure 31. The pumping duct is bounded by a semi-circular backwall, a moving wall, and two cover plates (refer to Figure 32 for a cross-sectional view of the pumping duct).

The stationary wall was composed of a 7 5/16 in. thick plexiglass plate sandwiched between two 1 in. thick plates of aluminum. A radius of 17.197 in. was machined in the back wall, then smoothed and polished to insure good visual properties.

Affixed directly to the ends of the backwall were the reservoir transition chambers. The chambers were designed so that a sudden increase in gap width would exist at the termination of the pumping region in order to minimize end effects.

From Figure 32, it can be seen that the pumping duct and transition chamber were bounded above and below by 3/4 in. thick plexiglass cover plates. The moving wall was composed of a 1/16 in. thick sheet of 70 durometer neoprene rubber taped to a .015 in. spring steel band. The rubber sheet extended 1/2 in. on either side of the steel band so that a wiper seal could be formed (see Figure 32). Due to the severe curvature of the rubber, it was necessary to sew the rubber to the edge of the steel band over the entire length of the test section.

The technique for sealing the ends of the pumping duct and transition reservoirs is shown in Figure 31. In the region of the transition reservoirs, spring steel flaps were attached to the moving wall.

The neoprene rubber sheet was taped and sewn to these flaps resulting in a continuous dynamic seal throughout the entire pumping chamber. These flaps were then clamped to the ends of the transition reservoirs enclosing the pumping channel.

With the test duct designed in this manner, internal pressures of 2 psig could be supported with minor leakage.

As was mentioned previously, the peristaltic action of the moving wall was generated using a variable speed roller cam. The cam was composed of a central aluminum structure which supported 48 adjustable roller arms. Figures 31 and 33 show the basic structure characteristics of the cam and rollers and their relative location within the apparatus. Thirty (30) of the rollers were constructed of aluminum and eighteen (18) were magnetic assemblies. The magnetic rollers were used where tension force was required to hold the steel band in position, i.e. at x = 0, 1/4, 1/2 on each wave.

Since the moving wall was indistensible, the transverse peristaltic motion was accompanied by a small amount of oscillatory type longitudinal motion. With a periodic wave, this secondary motion will have zero amplitude every wave length from the rigid holding support. In this apparatus the support was placed at one wave length from the beginning of the pumping duct so that the secondary motion would equal zero at every integer wave position within the pump.

The entire peristaltic pump was mounted within a 4 in. steel "I" beam frame which was designed to withstand both static and dynamic loading. The frame maintained tolerances within ± .003 in. without obstructing the visualization experiments.

5.3. Comparison Between the Experiment and the Two-Dimensional Theory

In constructing an experimental apparatus, it is not possible to exactly simulate the conditions prescribed by the two-dimensional theory. For this reason this section is intended to introduce the differences between theory and experiment, and to discuss three possible effects on the theoretical model.

In Chapter 3, the theory was developed for a straight pump with both walls undergoing peristaltic motion. Mechanically, it is much simpler to construct a circular experiment than a straight one. However, as long as the radius of curvature of the experiment (17.2 in.) is much larger than the mean gap width (.5") the curvature will have a negligible effect on the flow field.

The next point to be discussed concerns the effect of a single moving wall in the theory. It was shown in Chapter 3 that the local pressure gradient within a peristaltic pump is a function only of the local wall dimension relative to the local center line of the pump. In this apparatus this fact is still valid, but the center line of the pump is now in the center of the gap and is no longer the line of symmetry.

In accordance with the basic simulation criteria described in Chapter 3, the following features were incorporated into the apparatus: (a) the test section contained exactly three wave lengths (an integer number)*, (b) a periodic sinusoidal peristaltic wave was imposed on

---

*It should be noted that the two-dimensional theory could be modified to include non-integer wave lengths.

one wall, (c) open reservoirs, which were intended to approximate conditions of constant pressure, were placed at the ends of the pumping section.

At this point, feature (c) in the above paragraph requires furthur discussion. Because of the size of the reservoirs and the unsteady character of the instantaneous flow rate $Q(x,t)$ fluctuations in pressure level up to 3 mm of fluid were observed for $\phi = .9$. In addition, the flaps, which were used to seal the transition reservoirs, deformed with static pressure and induced additional pressure fluctuations. Together, these effects caused absolute pressure variations within the pump, but did not affect the differential pressure readings or visualization studies at low Reynolds numbers.

The fluctuations in reservoir pressure level became a serious problem in the higher Reynolds number studies which were done by E. Eckstein[20]. When fluid is supplied from a reservoir into a channel or duct, consideration must be given to the entry length where the Poiseuille type flow developes. Appendix C includes the details of a calculation showing that for $R < 1$ the entry length in this apparatus was less than $\lambda/25$. For this reason, it can be assumed that the flow is locally Poiseuille throughout the pumping channel.

In Section 5.2, the effect of wall indistensibility was mentioned, i.e. the presence of a secondary longitudinal motion. An analysis by Burns and Parks[1] showed that as $\alpha << 1$ this longitudinal motion will have a small effect on the theory ($\alpha = .013$ in this apparatus).

In Chapter 3, it was shown that the theoretical treatments of peristaltic pumping could be considered in terms of α, ϕ, R, and θ.

The values of these parameters in the present experiment are:

(i) Wave Number α. For all experiments conducted in this thesis the value of α was set at 0.013. From the work of Burns and Parks[1] and Jaffrin[5] this value of α was small enough so that the effects of wall curvature could be neglected.

(ii) Squeeze Ratio ϕ. Any value of ϕ between 0 and 0.9 could be imposed on the pumping channel with reasonable accuracy. However, with $\phi > 0.9$ the accuracy required in setting the gap increased beyond the maximum accuracy of the apparatus. In this experimental study, squeeze ratios of 0.9, 0.7, and 0.4 were used.

(iii) Reynolds Number R. For the experimental studies discussed in this thesis, the Reynolds number R ranged between .001 and .25. As will be shown, these Reynolds numbers were clearly within the inertia free range. By proper choice of wave speed and viscosity, values of R up to 30 could be obtained[20].

(iv) Mean Flow Rate θ. At each value of ϕ, a particular wave speed and viscosity could be chosen so that the mean flow rate θ could be obtained between $\theta = \theta_0$ and $\theta = 0$.

At this point, consideration must be given to the effects resulting from the actual cross-sectional geometry of the pumping channel. The first of these effects was originally discussed in Section 3.4 and concerns the presence of upper and lower cover plates. No more will be mentioned at this time as the results of the modification are discussed in detail in Section 5.5

In addition to these three-dimensional effects, the pumping channel also included inactive regions where the fluid was able to leak

backwards. These leakage channels existed at the seal recess slot in the backwall and at the top of the channel where the seal bends outward. Since the local pressure gradients within the pump were strongly dependent on the local gap widths, a significant increase in gap width will result in inactive regions which may in turn contain leakage flow.

The effect of this leakage flow can be incorporated into the theoretical model in the manner as discussed in Appendix D. Basically, the analysis assumes the flow in the leakage channel to be of the Poiseuille type and to be proportional to the local pressure gradient induced by the active peristaltic pump. From this analysis, a dimensionless parameter ϕ, which only depends on the geometry of the leakage channel, can be used to characterize the leakage flow within the pump. More will be said regarding this modification in Section 5.5.

5.4. Experimental Technique

The technique used to set the adjustable roller arms on the cam is discussed in the next paragraph. Initially, the moving wall was withdrawn from the machine, and a series of roller arms were extended until contact was made with the stationary wall. Using a removable micrometer rig, which was attached to the downstream transition chamber, the position of these extended rollers was measured and subsequently used to locate the position of the backwall. Knowing the thickness of the moving wall, the roller arms could be set to the desired wave shape. For the present experimental studies, the cam was adjusted to generate the following periodic wave shape:

$$\frac{h}{a} = 1 + \phi \sin 2\pi(\xi - \tau) \qquad (5\text{-}1)$$

with the local gap equal to 2h. Using the wall setting technique just described, each roller arm could be set within a tolerance of ±.002 in.

During each experimental run it was necessary to maintain a record of wave speed and fluid viscosity. The wave speed, which ranged between 1 cm/sec and 20 cm/sec, was logged on a Sanborn recorder with a timing mark. This mark was stimulated by a cam-microswitch assembly mounted on the center shaft of the machine.

After obtaining a fluid sample from the downstream over-flow pipe, during each run, the viscosity was measured using a Brookfield LV model viscometer. Occasional viscosity checks were made using a Saybolt viscometer.

Flow Rate. It was necessary to measure the time-mean flow rate through the pump by using a collection technique because of the unsteady character of the instantaneous flow rate. Using the three-way diverter valve, the downstream over-flow was diverted in graduated cylinders. Collection was made for at least six wave periods, i.e. one revolution of the cam. At the opening and closing of the diverter valve, a timing mark was entered onto the recorder by means of a foot-operated microswitch.

Pressure. The pressure rise across the machine was read directly from the reservoir manometers. To measure the pressure variation with time at fixed locations within the pumping duct, 1/8 in. diameter

pressure taps were drilled through the backwall at 1λ, 1 1/4 λ, 1 1/2 λ, 1 3/4 λ, and 2λ from the beginning of the pumping duct. All taps were placed 1 in. below the center of the channel (see Figures 35 and 37a). From the discussion of the nodal behavior of the pressure field within the pump (Chapter 3), these pressure taps were used to measure $P_{\xi=1/4} - P_0$, $P_{\xi=1/2} - P_0$, $P_{\xi=3/4} - P_0$, and ΔP_λ, respectively.

To this end, a pressure manifold was constructed from 3/8 in. tubing and attached to a Sanborn 268B differential pressure transducer (see Figure 34a). Because of the manifold, it was necessary to investigate the dynamic response of the pressure recording system. Using a technique discussed in Appendix E, the lowest natural frequency of the system was found to be 150 Hz. Since the characteristic frequencies measured were well below this value (e.g. < 1 Hz), no attenuation or amplification of the pressure signal was expected.

Visual. In all visual experiments, the character of the flow field was identified using dye injection techniques. The dye used was a mixture of Dupont Rhodamine B powered dye (orange), which was dissolved in water, and glycerine. By mixing proper proportions of glycerine and dye, the density of the dye was matched to the density of the working field. In some cases it was necessary to dissolve the powdered dye in pure glycerine.

In the visualization studies, the dye was injected into the pumping channel at two locations. When it was necessary to accurately place the dye, a micrometer controlled injection system was used (see Figure 34b). This injection rig replaced the central pressure tap during the visualization studies.

The other dye injection location, which was in the upstream transition chamber, was used for the visualization of the trapping phenomenon. This injection port, which was 0.1 in I.D. tubing, was not used when accurate placement of the dye was required.

The dye motion within the channel was photographed in color with either a Beaulieu R16 movie camera or a Mamiya Sekor 500Tb 35 mm still camera. For all experimental runs, the camera was mounted on a rig which was located on the center shaft of the experiment about 3 ft above the level of the injection ports (refer to Figure 35 for a photograph of the test channel as seen by the cameras). Data was obtained either in the wave reference frame, i.e. allowing the camera to move with the center shaft, or in the laboratory reference frame by holding the camera rig stationary.

Different visualization techniques were employed to identify the phenomena of reflux and trapping.

(i) Reflux. To identify the presence of reflux, the camera was mounted in the laboratory reference frame. Dye was injected, using the micrometer injection port, in the region near the stationary or moving wall. The net progress of the dye was photographed during various flow rates and squeezes in order that the "reflux" operating conditions could be identified.

By visualizing the flow field near the walls, reflux could be easily identified by the retrograde motion of the dye. Without reflux the dye would proceed downstream in the direction of wave motion.

(ii) Trapping. For all visualization studies pertaining to trapping, the camera recorded data in the wave reference frame. The first objective of these visual studies was to determine under what

conditions of flow θ and squeeze ϕ the trapped bolus exists within the flow field. The visualization technique which proved to be most successful for this work was related to the streamlines shape in the wave reference frame. Since the trapped bolus is bounded by a single streamline $\psi = 0$, any dye outside the bolus cannot enter into the trapped zone.

Using this simple idea, the progress of a line of dye, external of the bolus, was used to identify the existence of trapping as well as the outline of the trapped bolus. Figure 35 is a sketch showing the progress of the dye line after injection across the neck of the wave. The dye line can be considered as a series of material particle markers, each located on a particular streamline ψ. As time progresses, each particle will move along its particular streamline at a velocity depending on its location within the wave. Since the $\psi = 0$ streamline approaches a stagnation point at the end of the bolus, the dye marking this streamline will asymptotically approach a stationary position in the wave reference frame. The location of the dye marking $\psi = 0$ could be identified and used to calculate the velocities in the wave reference frame. More will be said about this point in the next section.

If no trapping is present, the injected dye will eventually pass through the wave into the following wave since all velocities within the wave are negative.

To visualize the internal structure of the bolus, dye was injected directly into the bolus. Experimentally, it was necessary to inject dye into two regions of the bolus to identify the internal

streamline patterns. Region I in Figure 36 was used to visualize the leading edge of the bolus, while Region II was used to obtain the rearward streamline patterns.

5.5. Results and Discussion

For the pressure studies as well as the visual experiments three values of squeeze ratio were used, i.e. $\phi = 0.4$, $\phi = 0.7$, and $\phi = 0.9$. These values proved sufficient to explore the operating range of the apparatus and to establish the validity of the modified leakage-channel theory.

Curves of $\Delta\tilde{P}_\lambda$ vs θ. To obtain the overall pumping characteristics of the apparatus, the pressure rise per wave length was measured as a function of flow rate for each value of ϕ. Using this data, curves of $\Delta\tilde{P}_\lambda$ vs θ were constructed and compared with the two-dimensional and modified theories.

Figures 5 through 7 display the experimental results along with the theoretical curves predicted by the two-dimensional theory (solid curves). The data clearly deviates from the theory. In order to reconcile the experiment with theory, it is necessary to include the effects produced by the actual cross-sectional geometry of the pumping channel.

At first we can consider the results obtained from the three-dimensional approximation described in Section 3.4 and Appendix A. The short dashed line in Figure 6 shows the curve of $\Delta\tilde{P}_\lambda$ vs θ with the three-dimensional approximation. This curve is only shown for $\phi = 0.7$, but the effects are similar for all ϕ's.

At each value of ΔP_λ the flow rate is reduced due to the presence of end walls. In particular, at $\Delta\tilde{P}_\lambda = 0$ the value of θ_0 is reduced to a value which is approximately equal to the value obtained experimentally. Alternatively, the pressure rise per wave length is reduced for each value of θ; however, at $\theta = 0$ the maximum pressure rise still remains above the experimental value.

The effect of a leakage area on the theory can be explained using the following concepts. The amount of leakage flow will be dependent on the magnitude of the adverse pressure gradient. At $\theta = \theta_0$ the mean pressure gradient is zero so the leakage flow will have a negligible effect on the flow field; however, as ΔP_λ is increased, the effect becomes more pronounced. For this reason θ_0 will be weakly affected by ϕ, i.e., curves of constant ϕ will remain linear and will always intersect $\theta = \theta_0$. The greater the leakage area the greater the effect on $\Delta\tilde{P}_{\lambda max}$.

The effects of the channel and leakage area can be combined to obtain a theoretical curve which agrees well with the experimental results (long dashed curves in Figures 5 through 7).

In order to correlate the modified theory with the experimental data, a value of the leakage parameter $\phi = 0.0061$ was required for $\phi = 0.7$ and $\phi = 0.4$; however, a value of $\phi = 0.0028$ was required for $\phi = 0.9$. This preceeding statement requires further explanation. Two values of ϕ were required because the area of the leakage channel was reduced between the experimental runs of $\phi = 0.9$ and those of $\phi = 0.7$ and $\phi = 0.4$. The important fact to consider is that a single value of ϕ was required for both $\phi = 0.4$ and $\phi = 0.7$. This should

be the case since ϕ depends only on the geometry of the leakage channel and no change in geometry was made between these experimental runs.

From the discussion of the leakage parameter in Section 5.3 and in Appendix D, a decrease in leakage area should be accompanied by a decrease in ϕ; however, this was not the case. This apparent contradiction can be explained by considering the assumption used in the leakage model. In the theoretical analysis, the pressure gradient in the leakage channel is imposed by the peristaltic pumping action. This fact requires that there be a free exchange of fluid in the vertical direction at every section in the pump. When narrow gaps are present, as for $\phi = 0.9$, this assumption will not be valid since there will be vertical pressure gradients restricting fluid motion. This restricted fluid motion will result in an apparent reduction in leakage area.

From the discussion in Appendix D, the value of ϕ can be related to an effective pipe leakage area. For $\phi = 0.7$, the value of ϕ corresponds to a leakage area of 0.5 cm^2, which roughly compares with the area affected by the curvature of the seal, i.e. the area where the rubber sheet bends to form the wiper seal.

The data obtained for $\Delta\tilde{P}_\lambda$ and θ also demonstrate the absence of inertial forces at least up to a Reynolds number of .25. From Figure 6, the data clearly shows that an order-of-magnitude increase in Reynolds number had no effect on the experimental results. A study conducted by E. Eckstein[20] showed that the inertial effects do not become important until the Reynolds number exceeds 2.

P(x,t) curves. Due to the sensitivity of the pressure transducer and the pressure limit of the dynamic seal, pressure pulses could be obtained experimentally only for certain values of ϕ and θ.

The experimental data is shown in Figures 8 through 11 for a series of squeeze ratios and flow rates. The theoretical curves were obtained using the leakage-channel theory with the appropriate values of ϕ. Both the leakage and the channnel modifications effect only the magnitude of the pressure pulse not the shape.

From Figures 8 through 11, it can be seen that the experimental results agree quite well with the theoretical predictions considering the strong dependence of the pressure gradient on the wall position. The best agreement between theory and experiment was obtained for $\phi = 0.4$. It should be noted, that the data displayed for $\phi = 0.4$ is an average curve taken from the actual pressure traces shown in Figure 37 (only $\theta = \theta_0$ data is shown). The eight cycle per wave oscillation present in these pulses are attributable to the pressure gradients induced by the small wall deflections which exist between the 8 roller arms. This oscillation was not observed with $\phi = 0.9$ and $\phi = 0.7$ since the local pressure gradients within the pump were much greater than the gradients induced by the wall deflection between the rollers.

The asymmetry exhibited in the pressure pulses shown in Figure 9 was attributed to an overdumped R-C filter in the electronic circuit.

Visualization Studies

(i) Reflux. Using the visualization technique discribed in Section 5.4, both qualitative and quantitative data on the reflux

phenomenon was obtained. By systematic variation of θ/θ_0 and ϕ, the reflux limit could be reasonably identified by the motion of the dye along the walls. With reflux present, the retrograde motion of the dye was a clear indication of its presence. The operating points where reflux was observed are plotted on the two-dimensional summary curve (Figure 14) with θ normalized with respect to θ_0 experimental. The symbols "Θ" and "θ" refer to the operating conditions where reflux was and was not observed, respectively. For $\phi = 0.7$ and $\phi = 0.4$, the data confirms the existence of "reflux" and "no reflux" operating regions. Using the present visualization technique, no information concerning the quantity of reflux flow could be obtained.

The reflux along the walls is clearly shown in Figure 38 which is a sequence of frames taken from the experimental data for $\phi = 0.7$ before ($\theta/\theta_0 = 0.84$) and after the onset of reflux ($\theta/\theta_0 = 0.57$). It is necessary to identify the retrograde position of the dye with a white indication line because of the limitations of black and white photography. For $\theta/\theta_0 = 0.57$ the position of the retrograde dye differs on each wall since dye was placed near the moving wall before it was placed on the stationary wall. At $\tau = 10.0$ the dye has progressed beyond the range of the camera.

(ii) Trapping. Using the techniques described in Section 5.4, the "trapped" operating conditions were observed and plotted on the two-dimensional summary curve (Figure 14). A "trapped" operating condition is indicated by " " and a "non-trapped" condition by " ". No trapping was observed for $\phi = 0.4$. At $\phi = 0.7$ the data showed

good agreement with the theoretical predictions of the two-dimensional theory. In Section 5.4 a technique was described for identifying the position of the forward stagnation point on the bolus. Briefly, the technique involved the recording of the motion of a dye line after insertion into the neck of the pumping channel. If trapping existed, the dye marking the center streamline ($\psi = 0$) approached the stagnation point of the bolus. Figure 39 is a sequence of frames showing the motion of the dye line for $\phi = 0.7$ and $\theta/\theta_0 = 1$. The location of the stagnation point as well as the outline of the bolus are clearly evident.

Using the preceeding technique, the position of the central streamline could be identified and plotted as a function of time after insertion. Figure 40 is a graph showing the position of dye marking $\psi = 0$ vs time. τ represents the non-dimensional time after insertion of the dye. $\tilde{x}$ is the wave frame position of the dye on the streamline $\psi = 0$. The curves for $\theta/\theta_0 = 1$ and $\theta/\theta_0 = 0.74$ clearly show the asymptotic behavior of the dye as it approached the stagnation point. The theoretical asymptotes are also shown on these curves.

When trapping is not present the dye passes directly through the wave as is shown for $\theta/\theta_0 = 0.52$.

Using the mean curve drawn thru the data, the slopes can be used to determine the wave frame velocity u/c as a function of $\tilde{x}$. Figure 41 is a plot of the experimental velocity data along with the velocities predicted by the two-dimensional theory. For $\theta/\theta_0 = 1$ and $\theta/\theta_0 = 0.74$ the data agrees quite well with the experimental results.

The detail structure of the bolus can be demonstrated by a series of photographs taken from experimental runs. Figure 42a is a close up view showing the shape of the leading edge of the bolus for $\phi = 0.9$ and $\theta/\theta_0 = 1$. The internal streamline pattern is clearly evident at the rear end of the bolus in Figure 42b for $\phi = 0.9$ and $\theta/\theta_0 = 1$. Figure 42c is a overall view of the trapped bolus beneath the crest of the wave with $\phi = 0.7$ and $\theta/\theta_0 = 1$.

APPENDIX A

EFFECT OF THREE-DIMENSIONAL PUMPING CHANNEL ON THE PLANE THEORY

The effects of three-dimensionality can be introduced into the plane theory by an approximate technique described by Purday[15].

Theoretically, the total instantaneous flow at each section within the pumping channel can be written as

$$Q_{total}(X,t) = 2w\left(- \frac{h^3}{3\mu} \frac{\partial P}{\partial X}\right) \tag{A-1}$$

Purday showed that for a channel the pressure gradient in a locally Poiseuille type flow will equal

$$\frac{\partial P}{\partial X} = - \frac{3\mu(h + 1)}{h^3} U_{AVG} \tag{A-2}$$

where n is a function of aspect ratio in the channel and can be obtained from Equation (3-58).

With U_{AVG} defined as flow rate per unit area of channel, a relation can be developed between the net flow rate through the pump Q_n and the theoretical flow rate Q. From Equation (a-1) and (A-2) this relation can be shown to equal

$$Q^*(x,t) = \frac{n}{n + 1} Q(x,t) \tag{A-3}$$

where

$$Q^*(x,t) \quad \frac{Q_n}{2w} \tag{A-4}$$

With the actual time mean flow defined as

$$\overline{Q^*} = \frac{1}{T}\int_0^T Q^* dt \tag{A-5}$$

where T is the wave period, and using Equation 10 of Reference 4, the non-dimensional average flow rate through the pump can be shown to be

$$\frac{\overline{Q^*}}{ac} = \frac{q}{ac}\int_0^1 \frac{n}{n+1}\, d\tau + \int_0^1 \frac{nH}{n+1}\, d\tau \tag{A-6}$$

Using the integral form of the continuity relation (Equation 3-3b) along with Equation (A-6) results in the following form of the modified pressure gradient in the experimental channel

$$\frac{\partial \tilde{P}}{\partial \xi} = \frac{\int_0^1 \frac{nH}{n+1}\, d\tau - \theta^*}{\int_0^1 \frac{n}{n+1}\, d\tau} \frac{\frac{n+1}{n}}{H^3} - \frac{\frac{n+1}{n}}{H^2} \tag{A-7}$$

where $\theta^* \equiv \frac{\overline{Q^*}}{ac}$

This expression can now be integrated to yield $p(x,t)$ and $\Delta\tilde{P}_\lambda$ vs θ^*.

APPENDIX B

INTRODUCTION OF A CATHETER

Currently, the diameters of intralumenal catheters are greater than the resting dimensions within the ureter. Therefore, as the catheter is inserted the lumen will encircle the catheter to form a quasi-axisymmetric annulus. Using this concept, a model will be developed showing the effects of a catheter on an axisymmetric lumen.

Figure 43 is a representation of the nomenclature used in this model. The analysis will be presented for a general wall shape in the wave reference frame.

It should be noted that the model assumes that the wave shape remains unchanged as the catheter is inserted. From the foregoing discussion, it is obvious that the catheter must effect the wall shape; however, for a first approximation this model shows the general effects of catheter insertion.

In the wave reference frame, the flow entering the wave is reduced due to the interference of the catheter. This wave frame flow now becomes

$$q = - c(a^2 - r_c^2) \qquad \text{(B-1)}$$

where r_c is the radius of the catheter.

The governing equations for this model are identical to those used in the axisymmetric formulation. However, the boundary conditions

are altered due to the presence of a catheter. These new boundary conditions in the wave reference frame are

$$u = -c \quad \text{at} \quad r = h$$

$$u = -c \quad \text{at} \quad r = r_c \tag{B-2}$$

Integration of the governing equations along with the introduction of Equation (B-1) results in the following expression for the non-dimensional pressure gradient in the wave reference frame

$$\frac{d\tilde{P}}{d\tilde{x}} = \frac{4}{3} \frac{R_c^2 - 1 + (H^2 - R_c^2)}{\gamma} = \omega(\tilde{x}) \tag{B-3}$$

where

$$\gamma \equiv \frac{1}{2}(H^4 - R_c^4) + 2\tau\left(\frac{1}{2} H^2 \ln H - \frac{1}{2} R_c^2 \ln R_c - \frac{1}{4} H^2 + \frac{1}{4} R_c^2\right)$$

$$- \beta(H^2 - R_c^2) \tag{B-4a}$$

$$\beta \equiv R_c^2 + \tau \ln R_c \tag{B-4b}$$

and

$$\sigma \equiv (H^2 - R_c^2)/(\ln R_c - \ln H) \tag{B-4c}$$

In the laboratory reference frame the pressure gradient can be written as

$$\frac{\partial \tilde{P}}{\partial \xi} = \Omega(\xi - \tau) \tag{B-5}$$

where $\Omega(\xi - \tau)$ is Equation (B-3) expressed in the laboratory coordinates.

The instantaneous flow within a wave is equal to

$$\frac{Q}{\pi a^2 c} = \int_{R_c^2}^{H^2} \frac{U}{c} \, d\left(\frac{R}{a}\right)^2 \tag{B-6}$$

Introducing the velocity profile and (A-1) into Equation (B-6) and integrating, results in an expression for the instantaneous flow rate. Taking the time mean of this expression over a wave length results in the following familiar form of the non-dimensional mean flow.

$$\theta = \overline{H^2} - 1 \tag{B-7}$$

APPENDIX C

EFFECT OF ENTRY LENGTH

The boundary layer thickness in a developing flow was shown by Schlichting[16] to be equal to

$$\delta = 5 \quad \frac{\nu \ell_x}{U} \tag{C-1}$$

where δ is the boundary layer thickness, ℓ_x is the length along the plate, and U is the velocity outside the boundary layer in the undisturbed stream.

Changing this expression to include the peristaltic pumping Reynolds number ($\frac{a^2 c}{\nu \lambda}$) results in the following expression for the thickness of the boundary layer;

$$\frac{\delta}{\ell_x} = \frac{5}{1/2} \quad \frac{a^2}{\ell_x \lambda} \tag{C-2}$$

At the beginning of the pumping channel the boundary layers form on both the stationary wall and the moving wall. Since the flow becomes fully developed when $\delta = a$, from equation (C-2) it can be seen that for a $R \leq 1$ the entry length region is less than $\lambda/25$.

APPENDIX D

EFFECT OF LEAKAGE FLOW

The leakage flow modification can be considered independently and then combined with the channel modification to yield a theoretical approximation for the experimental geometry.

The instantaneous flow through any section of the pump is related to the total pump cross-sectional area by the following continuity relation

$$\frac{\partial Q_n}{\partial X} + \frac{\partial A}{\partial t} = 0 \qquad \text{(D-1)}$$

In this model, the leakage area will be assumed constant at every section and equal to A_L while the pump area will equal

$$A_p(X,t) = 2wh(X,t) \qquad \text{(D-2)}$$

Using this fact, continuity can be rewritten as

$$\frac{\partial Q^*}{\partial X} + \frac{\partial h}{\partial t} = 0$$

where Q^* is defined by Equation (A-4). In this model, Q^* can be expressed as a linear sum of the instantaneous flow in the active pump Q_F and the leakage flow Q_L. Mathematically, this statement can be written as

$$\frac{Q^*}{ac} = \frac{Q_F}{ac} + \frac{A_L}{aw}\left(\frac{Q_L}{A_L c}\right) \qquad \text{(D-3)}$$

For low Reynolds numbers, the leakage flow can be considered a Poiseuille type flow, which is proportional to the local peristaltic pumping pressure gradient. The leakage will be assumed to be of the following form.

$$\frac{Q_L}{A_L c} \equiv - K \frac{A_L}{a^2} \frac{\partial P}{\partial \xi} \tag{D-4}$$

where K is a constant.

Integrating the continuity equation and using Equation (D-3) results in the following relation between the instantaneous flows and the average flows.

$$\frac{Q_F}{ac} + \frac{A_L}{aw} \left(\frac{Q_L}{A_L c}\right) = H - \overline{H} + \frac{\overline{Q}_F}{ac} + \frac{A_L}{aw} \left(\frac{\overline{Q}_L}{ac}\right) \tag{D-5}$$

Knowing that Q_F is actually equal to Q in the two-dimensional theory and using Equation (D-4), the actual pressure gradient in the pump can be written as

$$\frac{\partial \tilde{P}}{\partial \xi} = \frac{(\overline{H} - \theta^*)}{(H^3 + \phi)} - \frac{H}{(H^3 + \phi)} \tag{D-6}$$

where

$$\phi \equiv K \frac{A_L^2}{a^3 w} \tag{D-7}$$

In the analysis ϕ is a non-dimensional parameter which is found experimentally and is only a function of channel geometry. The higher the value of ϕ the larger the leakage area.

If an analogy is made between the leakage-flow defined by Equation (D-4) and a Poiseuille flow through a pipe, K can be found to equal 3/8 π. Equation (D-7) can then be used to calculate an effective pipe leakage area which will have the same leakage flow as the experimental apparatus.

APPENDIX E

CALCULATION OF THE NATURAL FREQUENCY OF THE PRESSURE-MANIFOLD SYSTEM

For a spring-mass system, the natural frequency f can be expressed as

$$f = \frac{1}{2\pi} \sqrt{k/m} \tag{E-1}$$

where k is the spring constant and m is mass. The analogy within a fluid system is

$$f = \frac{1}{2\pi} \sqrt{1/CI} \tag{E-2}$$

where C is the capacitance of the system and I is the total inertance of the fluid defined by the following relation.

$$I = \sum_{i}^{n} \frac{\rho_i \ell_i}{A_i} \tag{E-3}$$

where i refers to each component of a fluid circuit up to n components and ℓ_i/A_i is the length to area ratio of each component.

Knowing all dimensions within the pressure recording system, and assuming that the capacitance is only due to the pressure transducer, the natural frequencies of the manifold can be calculated (refer to Reference 23 for a detailed discussion of this analysis).

Resting Diameter	Wave Length	Contracted Length	Transition Length	Bolus Length	Minimum Diameter	Bolus Diameter	$P_{max} - P_{basal}$	Spurt Volume
mm	cm	cm	cm	cm	mm	mm	mmHg	cm^3
Physiological Range								
0.1 → 2	8 → 20	3 → 12	3 → 12	1 → 5	0.1 → 0.5	2 → 3	5 → 20	0.02 → 0.5
Ureteral Model								
2a	λ	$L_1\lambda$	$L_2\lambda$	$L_3\lambda$	$2H_1a$	$2H_3a$	$P_{max} - P_0$	Q_U
0.1	16	11.50	3.50	1	0.095	2.5	8.25	0.05
	17	11.50	3.50	2	0.095	2.5	8.25	0.10
	19	11.50	3.50	4	0.095	2.5	8.25	0.20
0.1	16	7.50	7.50	1	0.094	2.5	7.50	0.05
	17	7.50	7.50	2	0.094	2.5	7.50	0.10
	19	7.50	7.50	4	0.094	2.5	7.50	0.20
0.1	16	7.50	7.50	1	0.092	2.5	13.50	0.05
	17	7.50	7.50	2	0.092	2.5	13.50	0.10
	19	7.50	7.50	4	0.092	2.5	13.50	0.20
0.1	16	3.50	11.50	1	0.082	2.5	18.75	0.05
	17	3.50	11.50	2	0.082	2.5	18.75	0.10
	19	3.50	11.50	4	0.082	2.5	18.75	0.20

TABLE 1: TYPICAL VALUES OF PEAK PRESSURE AND SPURT VOLUME FOR CIRCULAR GEOMETRY

Resting Lobe Width	Wave Length	Contracted Length	Transition Length	Bolus Length	Minimum Lobe Width	Bolus Lobe Width	$P_{max} - P_{basal}$	Spurt Volume
mm	cm	cm	cm	cm	mm	mm	mmHg	cm^3
Physical Range								
0.1 → 2	8 → 20	3 → 12	3 → 12	1 → 5	0.1 → 0.5	0.1 → 1	5 → 20	0.02 → 0.5
Ureteral Model								
2a	λ	$L_1\lambda$	$L_2\lambda$	$L_3\lambda$	$2H_1a$	$2H_3a$	$P_{max} - P_0$	Q_U
0.056	16	11.50	3.50	1	0.053	0.56	6.07	0.03
	17	11.50	3.50	2	0.053	0.56	6.07	0.07
	19	11.50	3.50	4	0.053	0.56	6.07	0.12
0.056	16	7.50	7.50	1	0.052	0.56	4.50	0.03
	17	7.50	7.50	2	0.052	0.56	4.50	0.06
	19	7.50	7.50	4	0.052	0.56	4.50	0.12
0.056	16	7.50	7.50	1	0.050	0.56	9.98	0.04
	17	7.50	7.50	2	0.050	0.56	9.98	0.07
	19	7.50	7.50	4	0.050	0.56	9.98	0.13
0.056	16	3.50	11.50	1	0.046	0.56	18.24	0.05
	17	3.50	11.50	2	0.046	0.56	18.24	0.08
	19	3.50	11.50	4	0.046	0.56	18.24	0.14

TABLE 2: TYPICAL VALUES OF PEAK PRESSURE AND SPURT VOLUME FOR LOBE-SHAPED GEOMETRY

FIGURE CAPTIONS

1 - Basic Anatomy of Urinary Tract

2 - Cross Section of Ureter

3 - Urometric Pressure Pulses

4 - Basic Nomenclature in Laboratory and Wave Reference Frames

5 - $\tilde{\Delta P}_\lambda$ vs θ for $\phi = 0.4$

6 - $\tilde{\Delta P}_\lambda$ vs θ for $\phi = 0.7$

7 - $\tilde{\Delta P}_\lambda$ vs θ for $\phi = 0.9$

8 - $P(x,t)$ for $\phi = 0.9$ $\quad \theta/\theta_0 = 0.96$

9 - $P(x,t)$ for $\phi = 0.7$ $\quad \theta/\theta_0 = 0.79$

10 - $P(x,t)$ for $\phi = 0.4$ $\quad \theta/\theta_0 = 1$

11 - $P(x,t)$ for $\phi = 0.4$ $\quad \theta/\theta_0 = 0$

12 - Streamlines in Wave Frame

13 - Sketch of Mean Flow Distribution Across Pump

14 - Two-Dimensional Summary Curve

15 - Reflux Flow Curve at $\theta = 0$ (Plane Geometry)

16 - Axisymmetric Summary Curve

17 - Reflux Flow at $\theta = 0$ (Axisymmetric Geometry)

18 - Pressure Pulse for $\Delta P_\lambda \neq 0$

19 - Time-Varying vs Position-Varying Pressure Pulses

20 - Nomenclature and Pressure Pulse for Square Wall Shape

21 - Pressure Gradient for Lobed and Circular Geometries

22 - Nomenclature for Continuous Wall Shape

23 - Pressure Pulses for Continuous Wall Shape

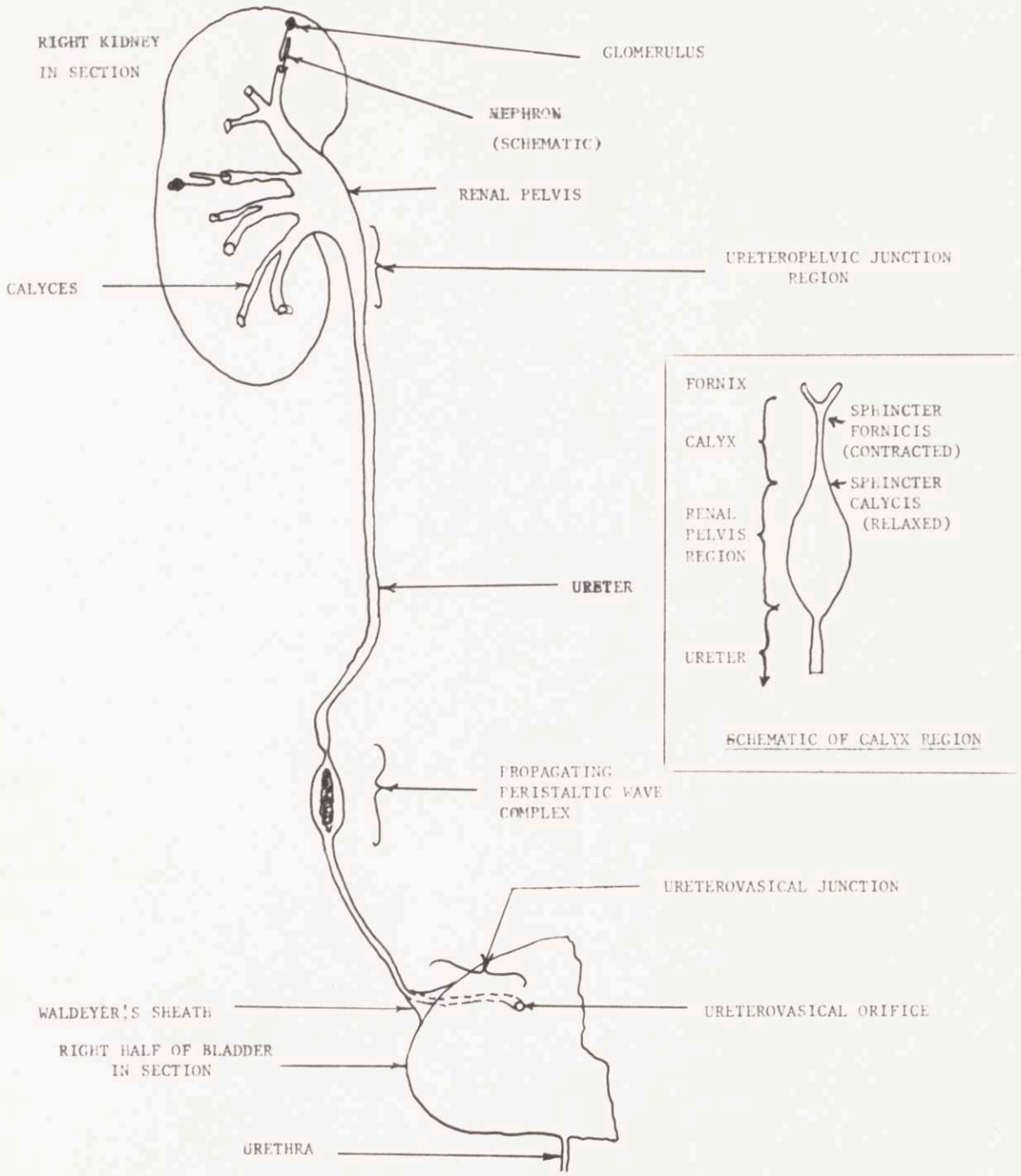
RIGHT KIDNEY
IN SECTION
GLOMERULUS
NEPHRON
(SCHEMATIC)
RENAL PELVIS
URETEROPELVIC JUNCTION
REGION
CALYCES
FORNIX
CALYX
RENAL
PELVIS
REGION
URETER
SPHINCTER
FORNICIS
(CONTRACTED)
SPHINCTER
CALYCIS
(RELAXED)
SCHEMATIC OF CALYX REGION
URETER
PROPAGATING
PERISTALTIC WAVE
COMPLEX
URETEROVASICAL JUNCTION
WALDEYER'S SHEATH
URETEROVASICAL ORIFICE
RIGHT HALF OF BLADDER
IN SECTION
URETHRA

FIGURE 1

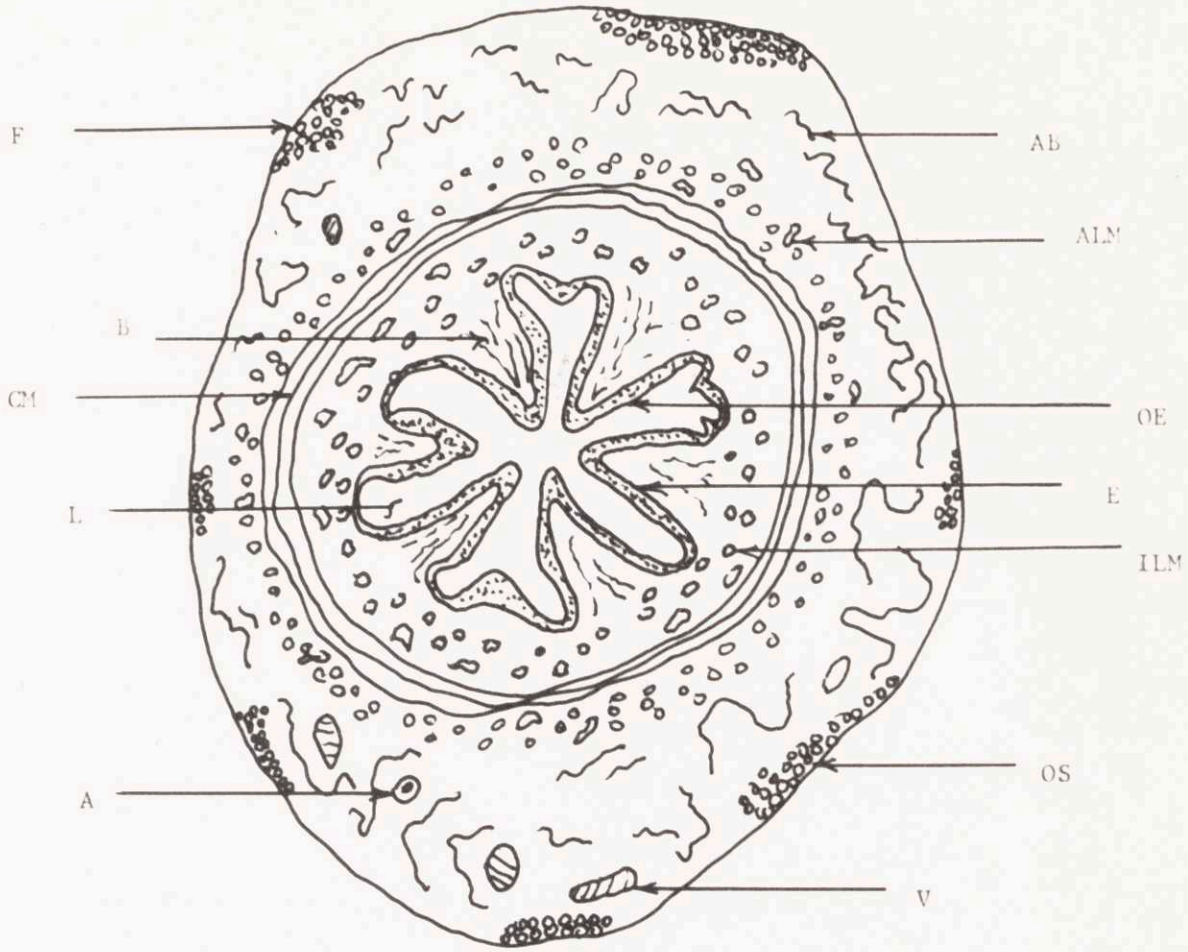

A - ARTERIES
AB - ADVENTITIAL CONNECTIVE TISSUE
ALM - EXTERNAL LONGITUDINAL MUSCLES
B - LAMINA PROPRIA
CM - CIRCULAR MUSCLES
E - DEEP LAYER OF EPITHELIUM
F - FAT TISSUE
ILM - INTERNAL LONITUDINAL MUSCLES
L - LUMEN
OE - SUPERFICIAL EPITHELIAL CELLS
OS - OUTER SHEATH
V - VEINS

FIGURE 2

(a) TYPICAL SERIES OF URETERAL PRESSURE PULSES

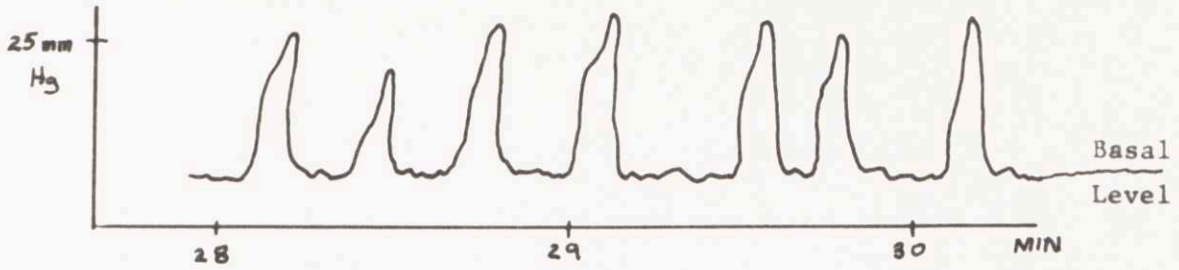

(b) PELVIC PRESSURE AS BLADDER IS BEING FILLED

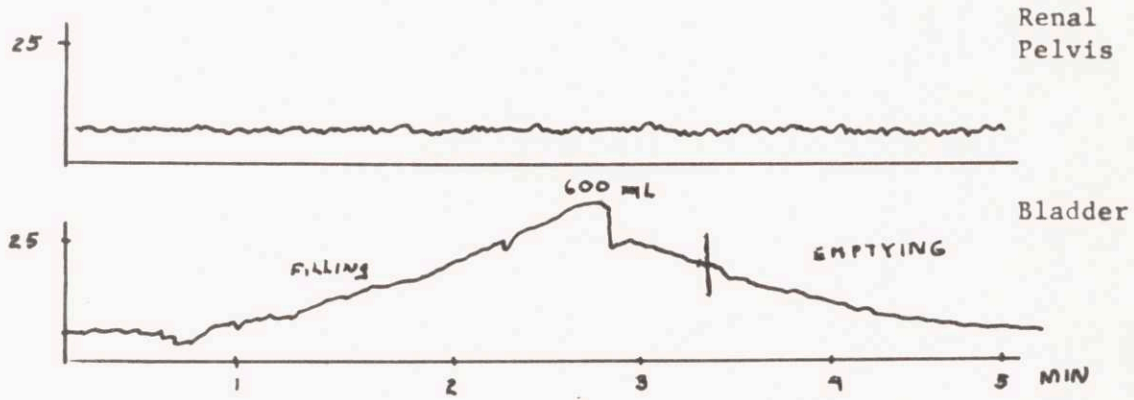

(c) URETERAL CONTRACTIONS AND URINE SPURTS DURING FILLING OF BLADDER

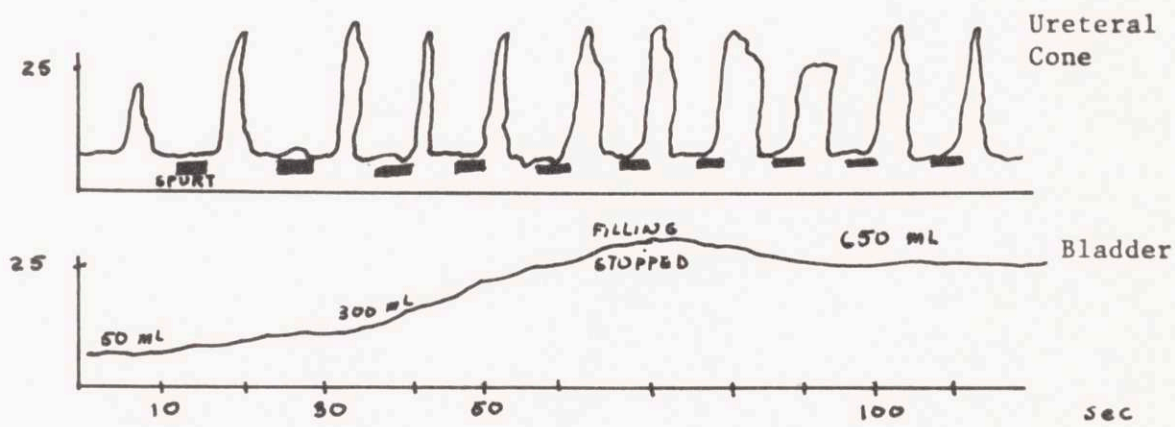

FIGURE 3

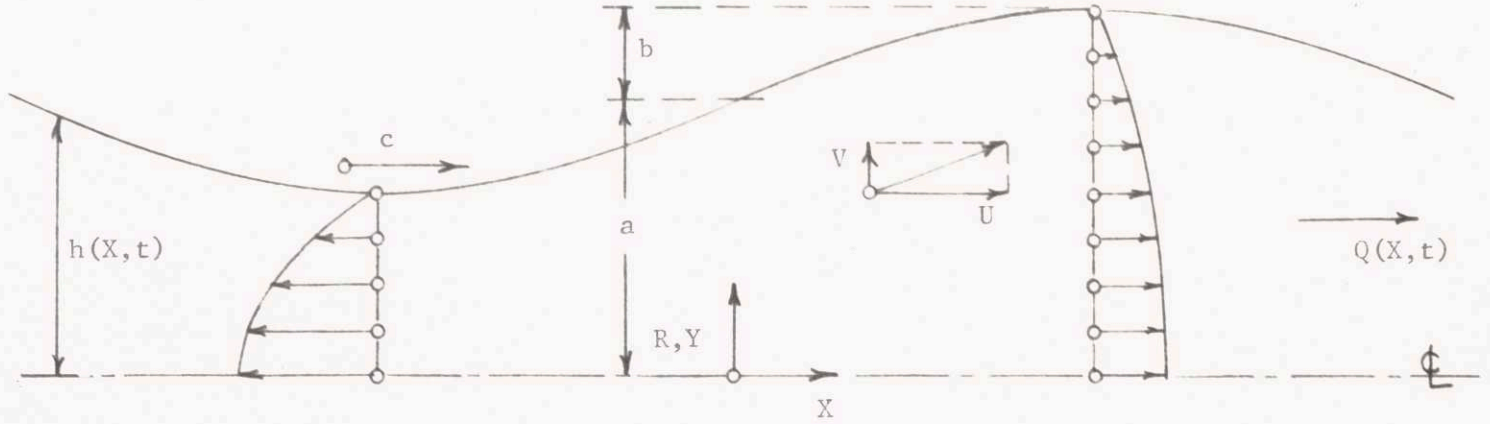

LABORATORY REFERENCE FRAME

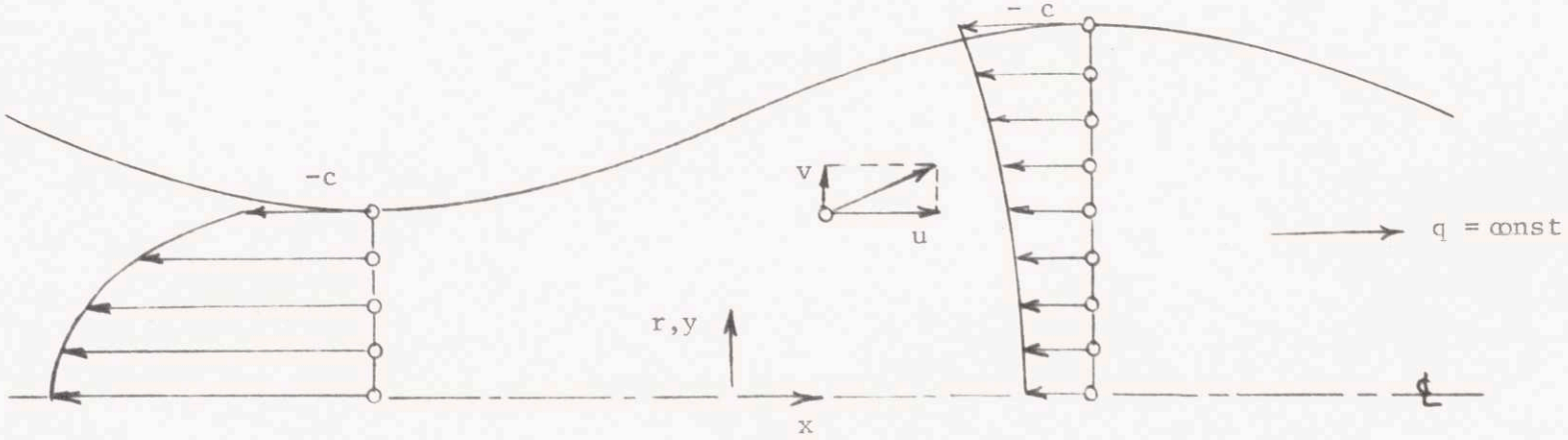

WAVE REFERENCE FRAME

FIGURE 4

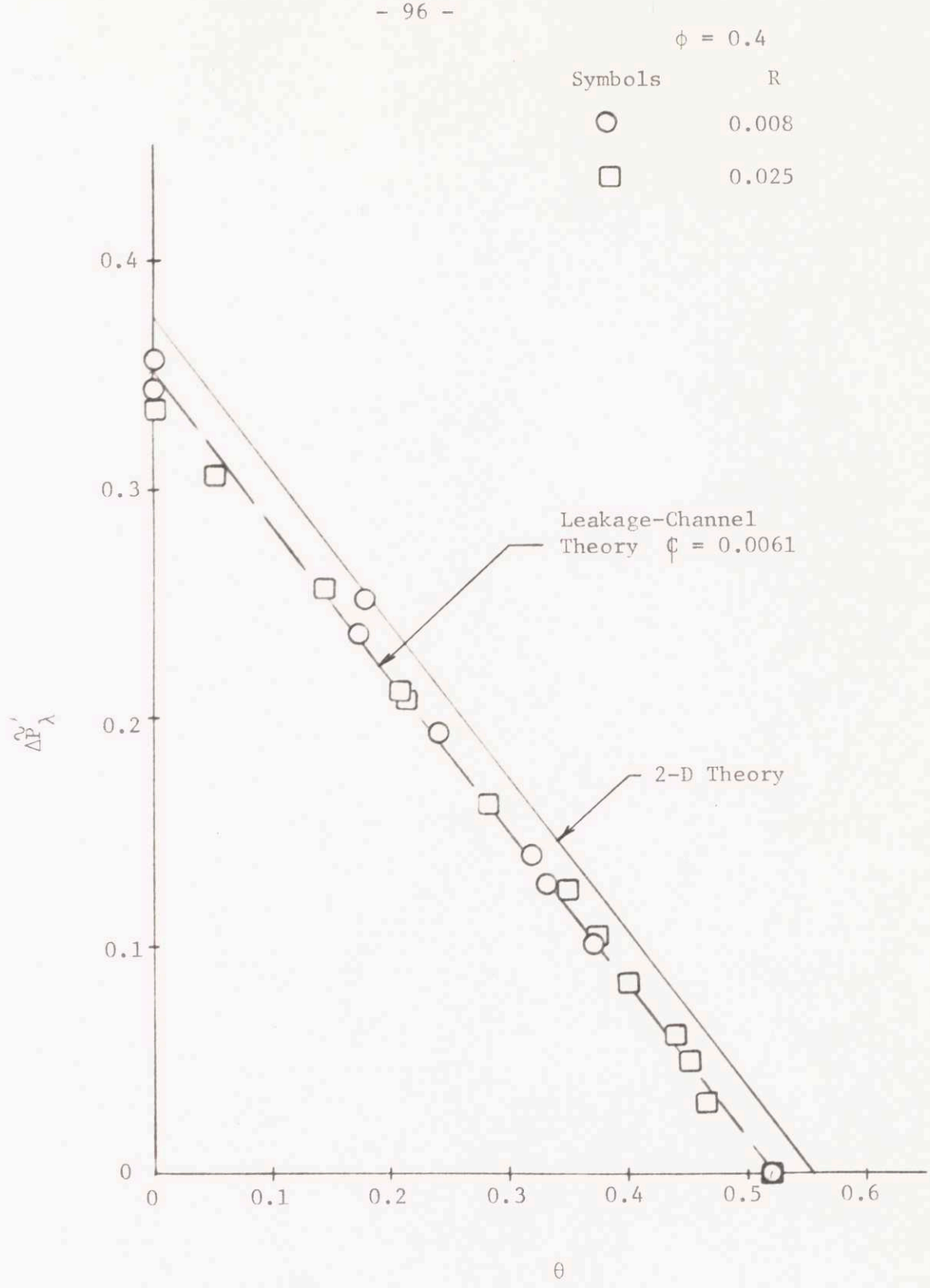
ϕ = 0.4
Symbols
R
0.008
0.025
Leakage-Channel Theory ¢ = 0.0061
2-D Theory
$\Delta\tilde{P}'_\lambda$
θ
0
0.1
0.2
0.3
0.4
0.5
0.6

FIGURE 5

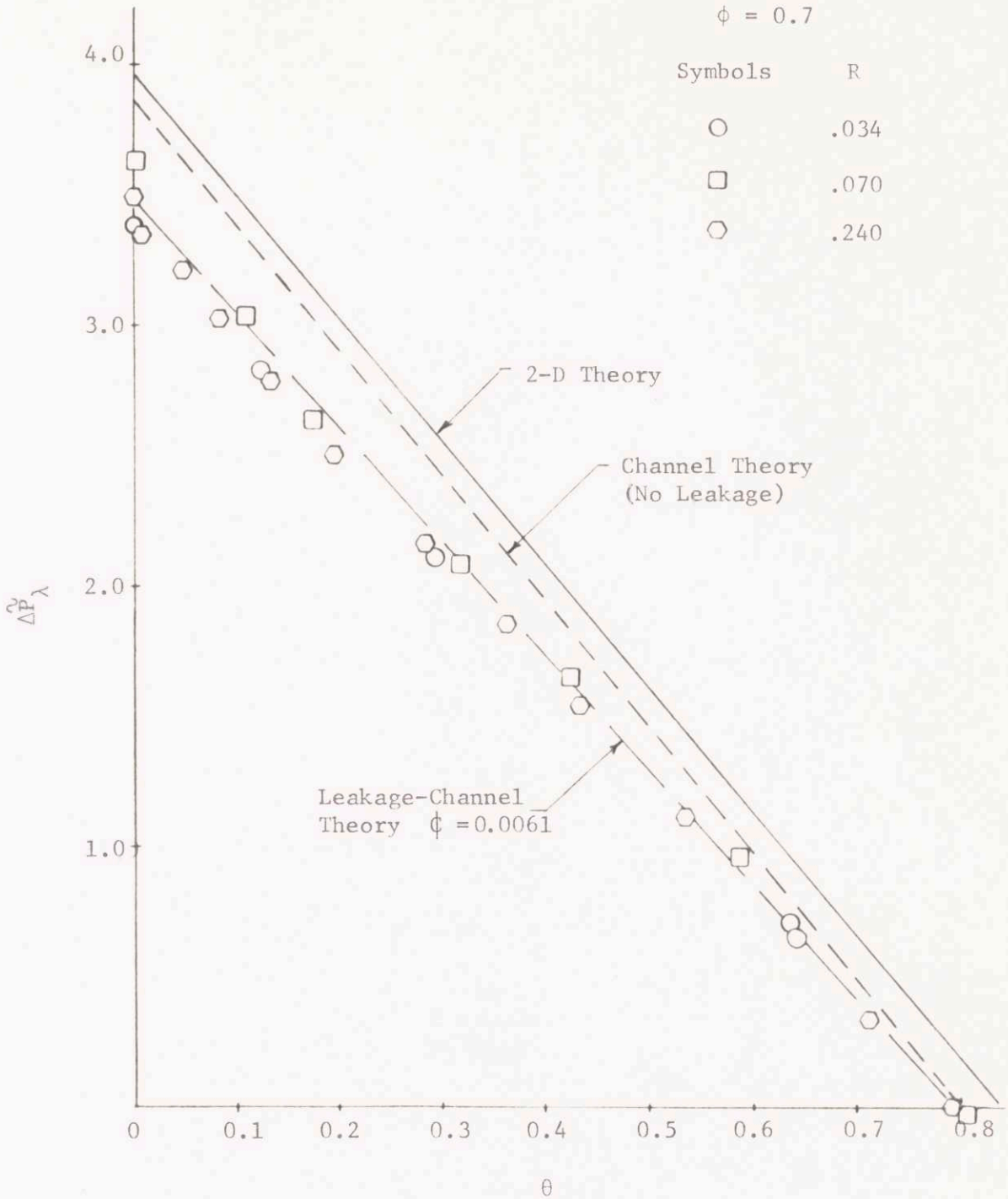
ϕ = 0.7
Symbols R
.034
.070
.240
2-D Theory
Channel Theory
(No Leakage)
Leakage-Channel
Theory ¢ =0.0061
4.0
3.0
2.0
1.0
0
0.1
0.2
0.3
0.4
0.5
0.6
0.7
0.8
θ
$\Delta\bar{P}_\lambda$

FIGURE 6

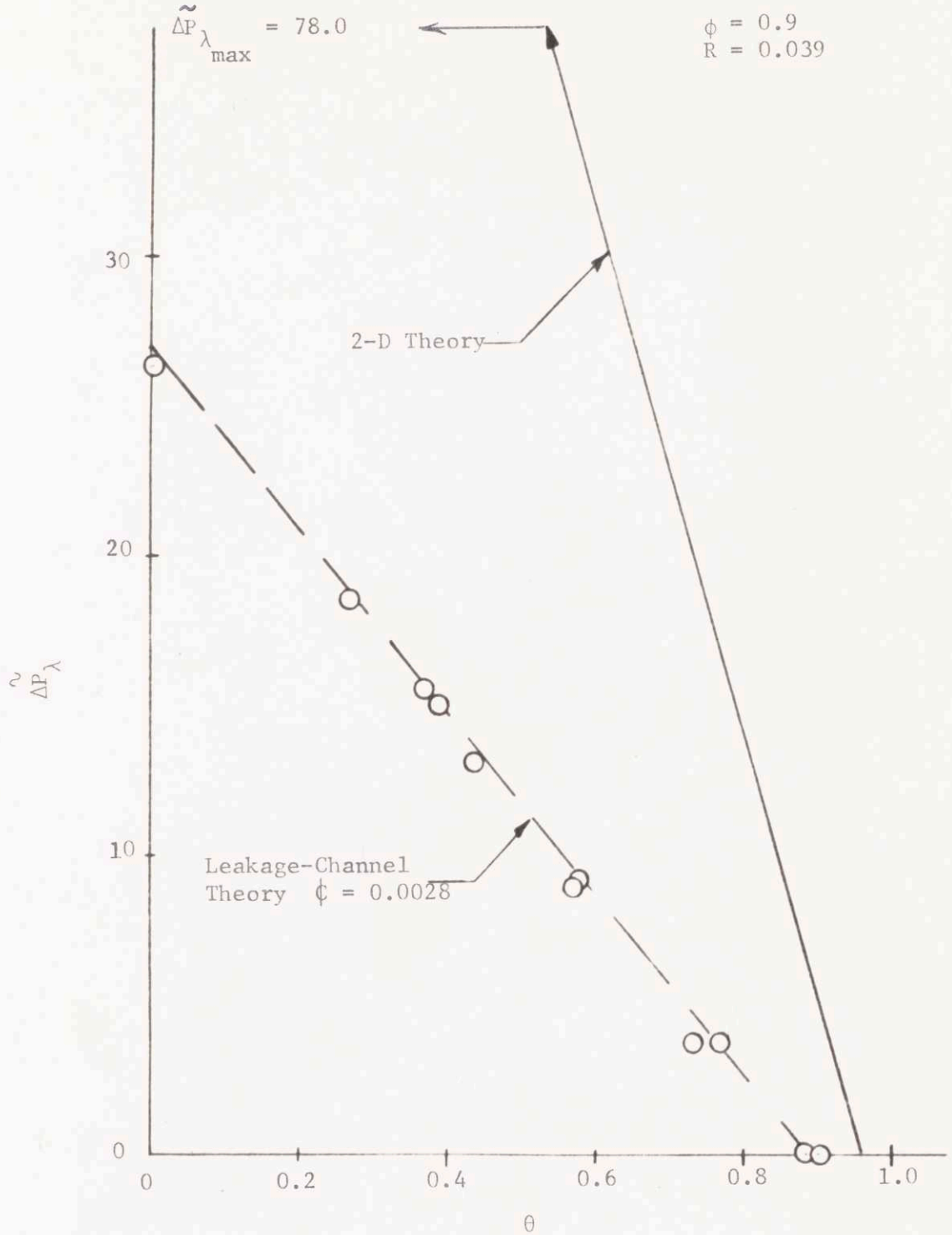
$\widetilde{\Delta P}_{\lambda_{max}}$ = 78.0
ϕ = 0.9
R = 0.039
30
20
10
0
2-D Theory
Leakage-Channel
Theory ¢ = 0.0028
$\widetilde{\Delta P}_{\lambda}$
0
0.2
0.4
0.6
0.8
1.0
θ

FIGURE 7

$\phi = 0.9$ $\frac{\theta}{\theta_0} = 0.96$

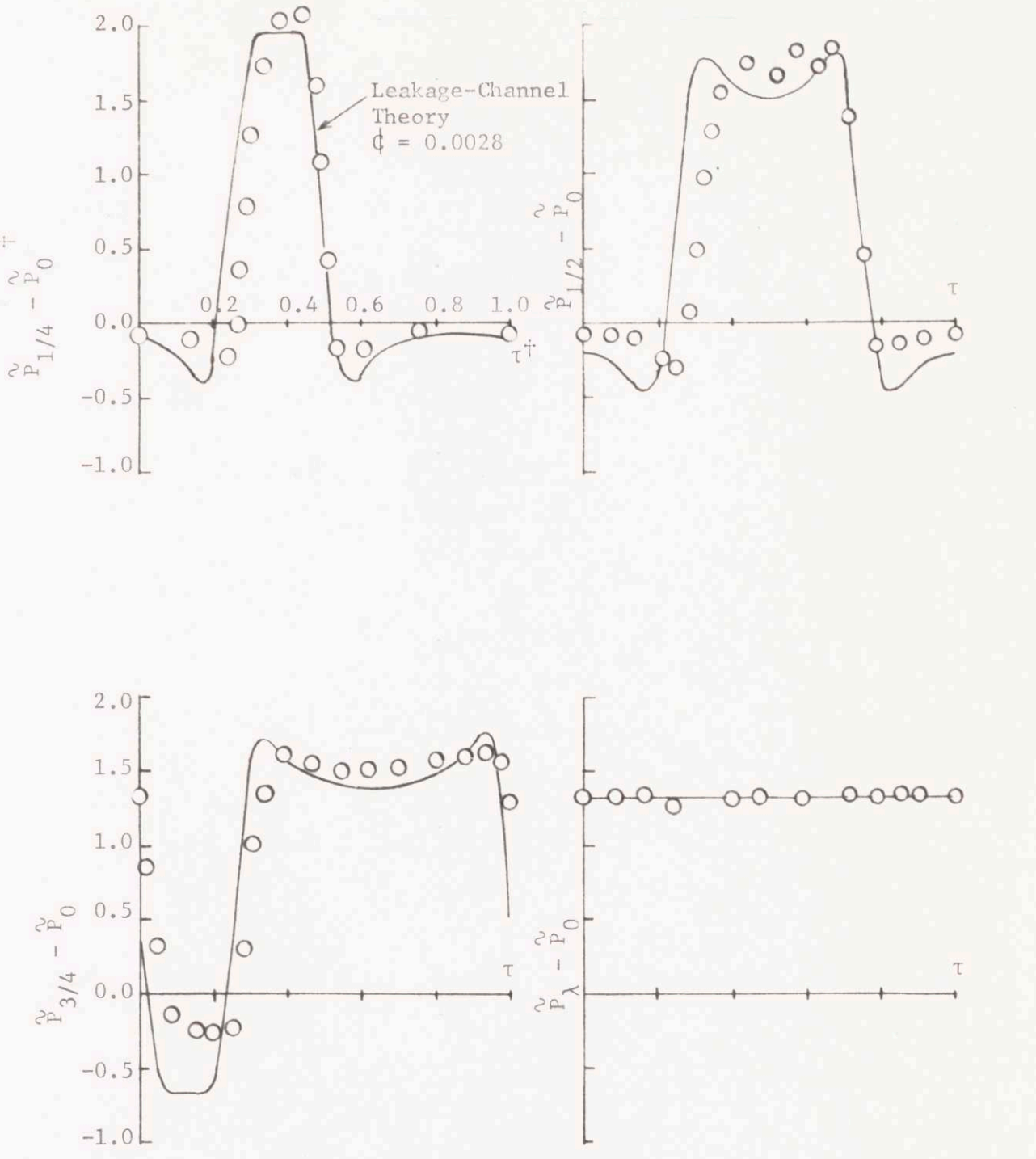

† Scales identical on each trace

FIGURE 8

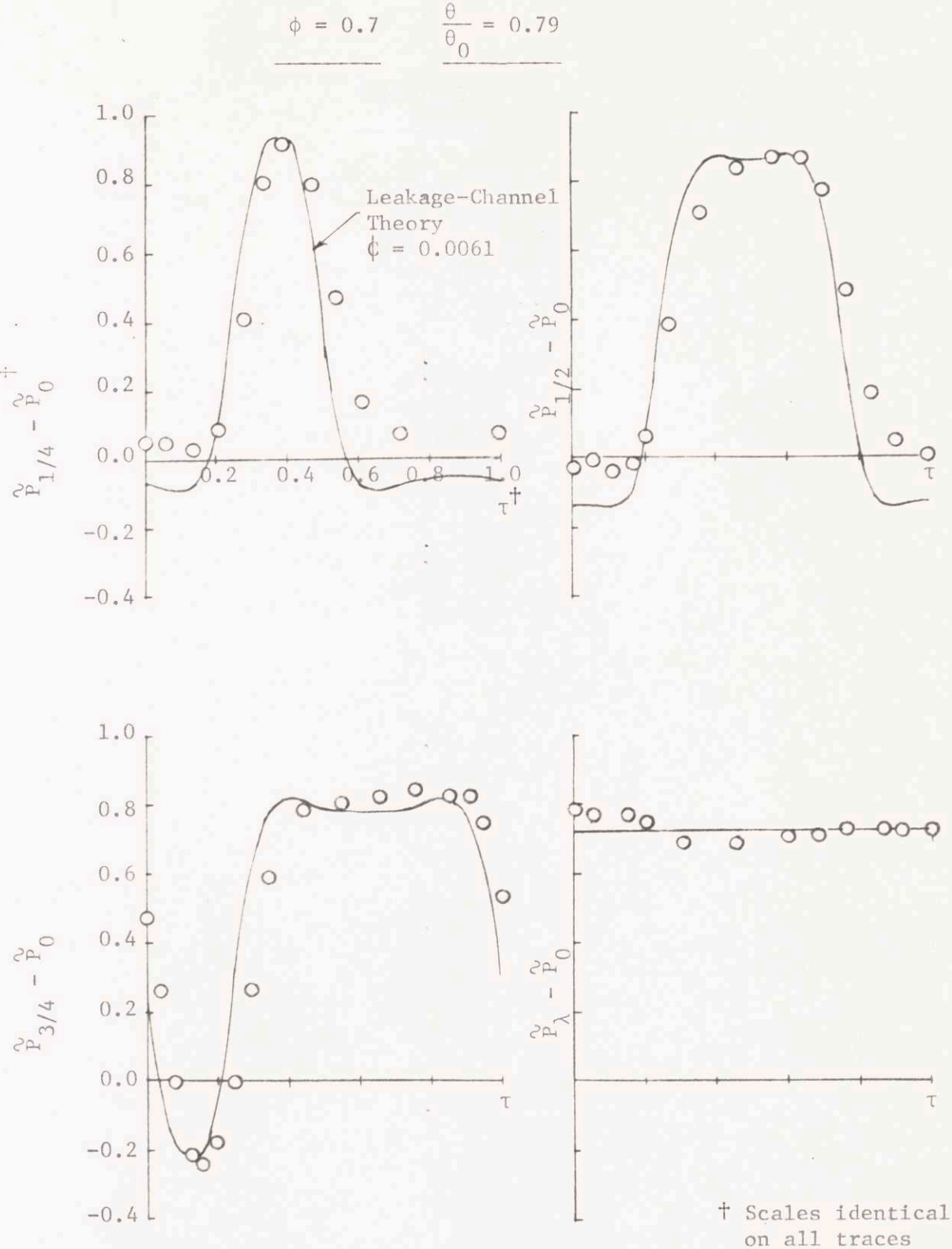
ϕ = 0.7
$\frac{\theta}{\theta_0}$ = 0.79
Leakage-Channel Theory
ϕ = 0.0061
$\tilde{P}_{1/4} - \tilde{P}_0$ †
$\tilde{P}_{1/2} - \tilde{P}_0$
$\tilde{P}_{3/4} - \tilde{P}_0$
$\tilde{P}_\lambda - \tilde{P}_0$
τ
τ†
† Scales identical on all traces

FIGURE 9

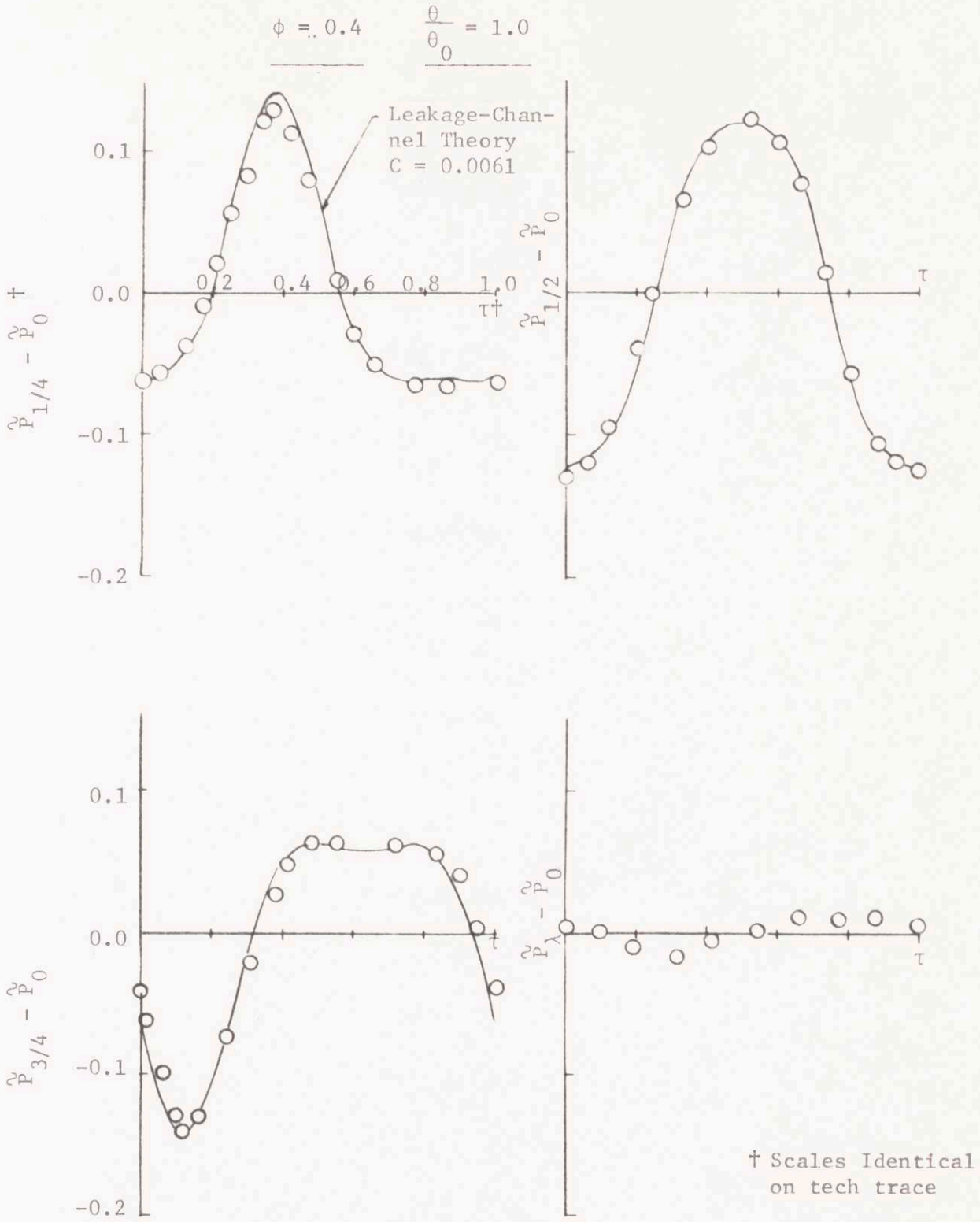
$\phi = 0.4$
$\frac{\theta}{\theta_0} = 1.0$
Leakage-Channel Theory
C = 0.0061
$\tilde{P}_{1/4} - \tilde{P}_0$ †
$\tilde{P}_{1/2} - \tilde{P}_0$
$\tilde{P}_{3/4} - \tilde{P}_0$
$\tilde{P}_{\lambda} - \tilde{P}_0$
0.1
0.0
-0.1
-0.2
0.2
0.4
0.6
0.8
1.0
τ
τ†
† Scales Identical on tech trace

FIGURE 10

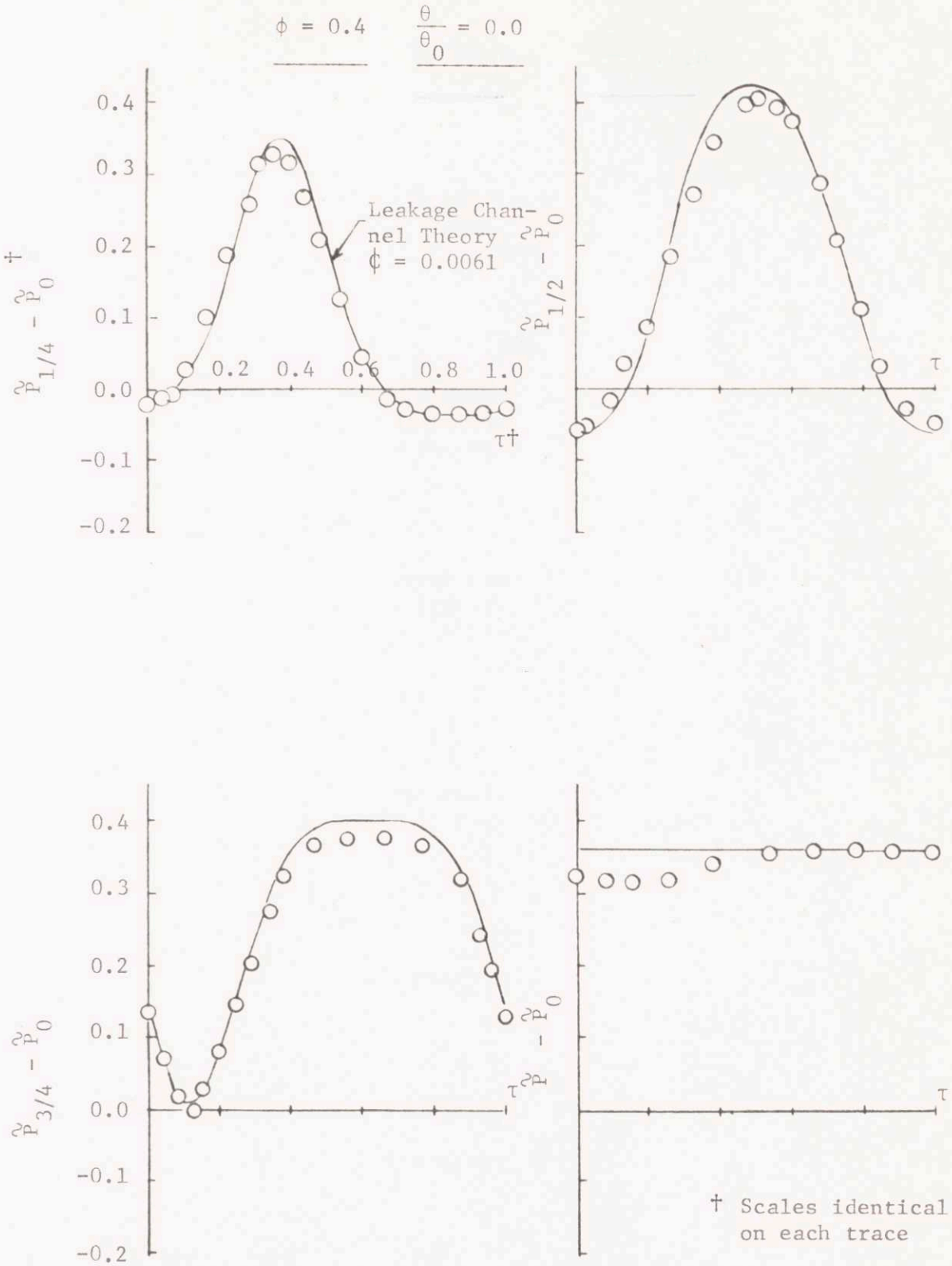
ϕ = 0.4
$\frac{\theta}{\theta_0}$ = 0.0
Leakage Channel Theory
ϕ = 0.0061
$\tilde{P}_{1/4} - \tilde{P}_0$ †
$\tilde{P}_{1/2} - \tilde{P}_0$
$\tilde{P}_{3/4} - \tilde{P}_0$
$\tilde{P} - \tilde{P}_0$
0.4
0.3
0.2
0.1
0.0
-0.1
-0.2
0.2
0.4
0.6
0.8
1.0
τ†
τ
† Scales identical on each trace

FIGURE 11

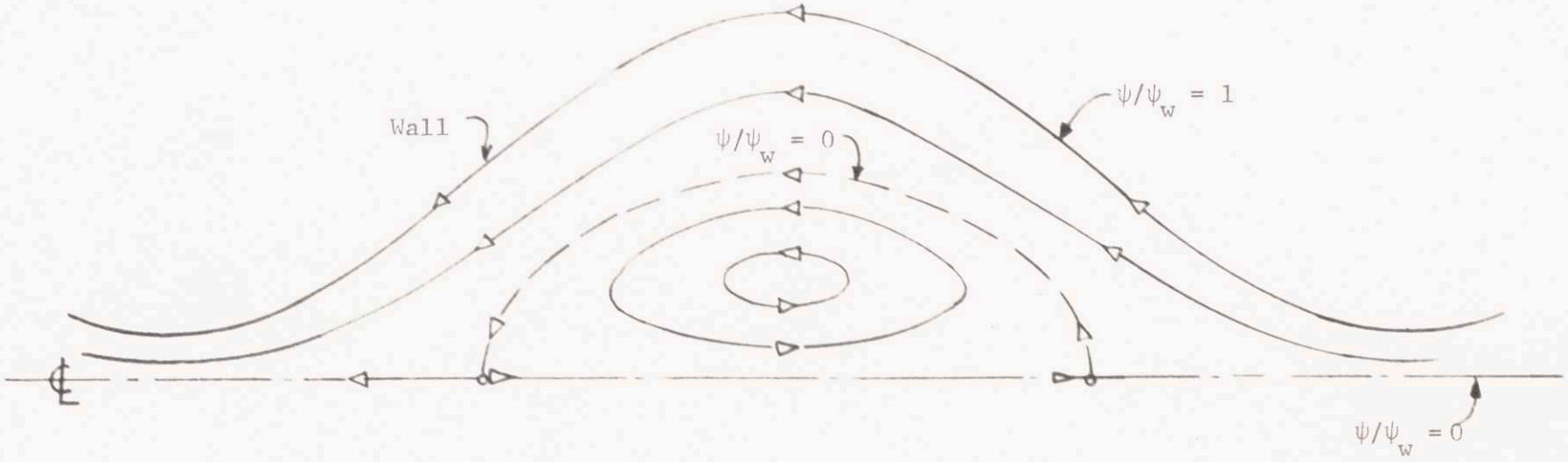

STREAMLINES IN WAVE FRAME

FIGURE 12

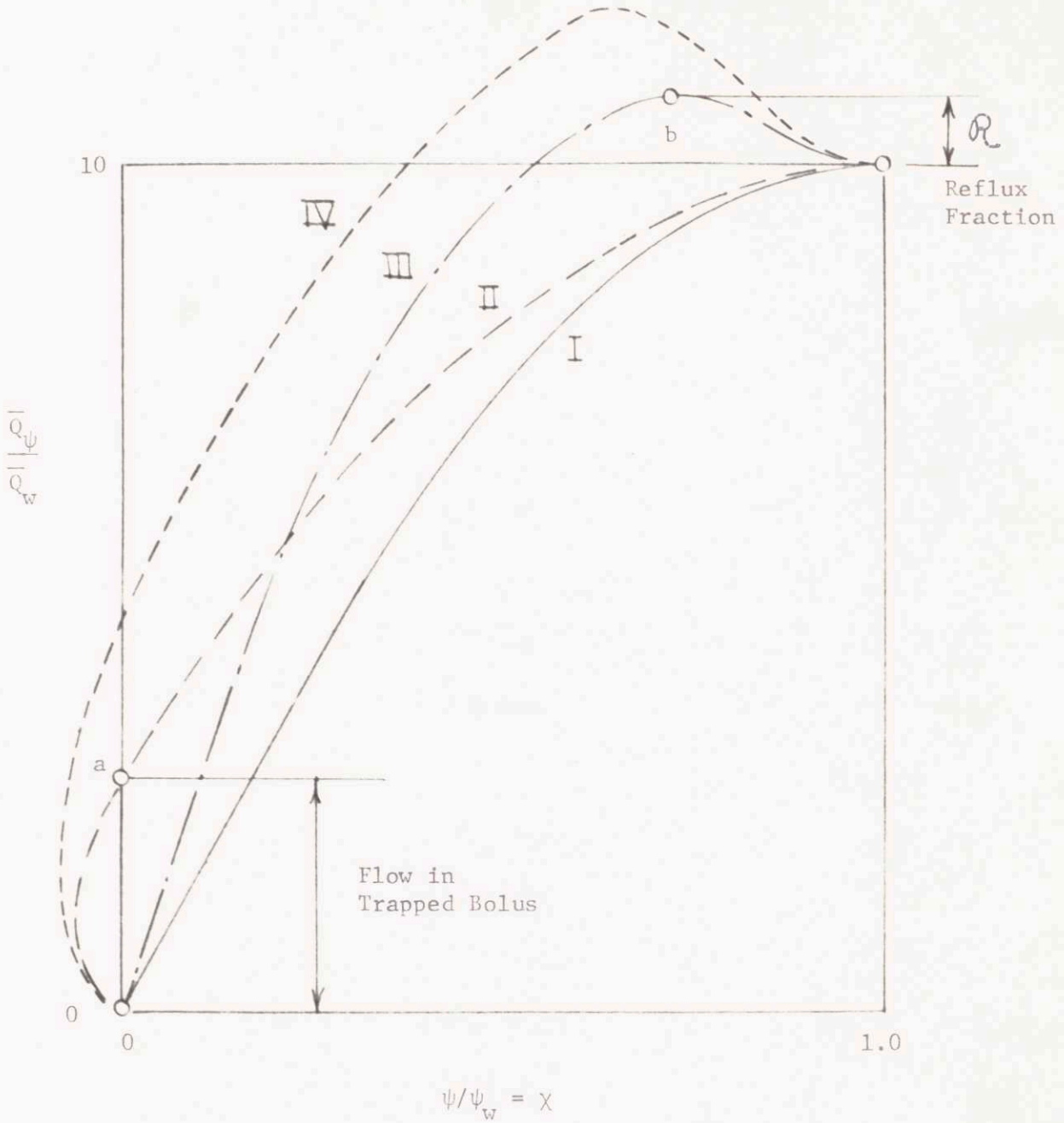
10
0
0
1.0
a
b
R
Reflux
Fraction
IV
III
II
I
Flow in
Trapped Bolus
$|Q_\psi|/|Q_w|$
$\psi/\psi_w = \chi$

FIGURE 13

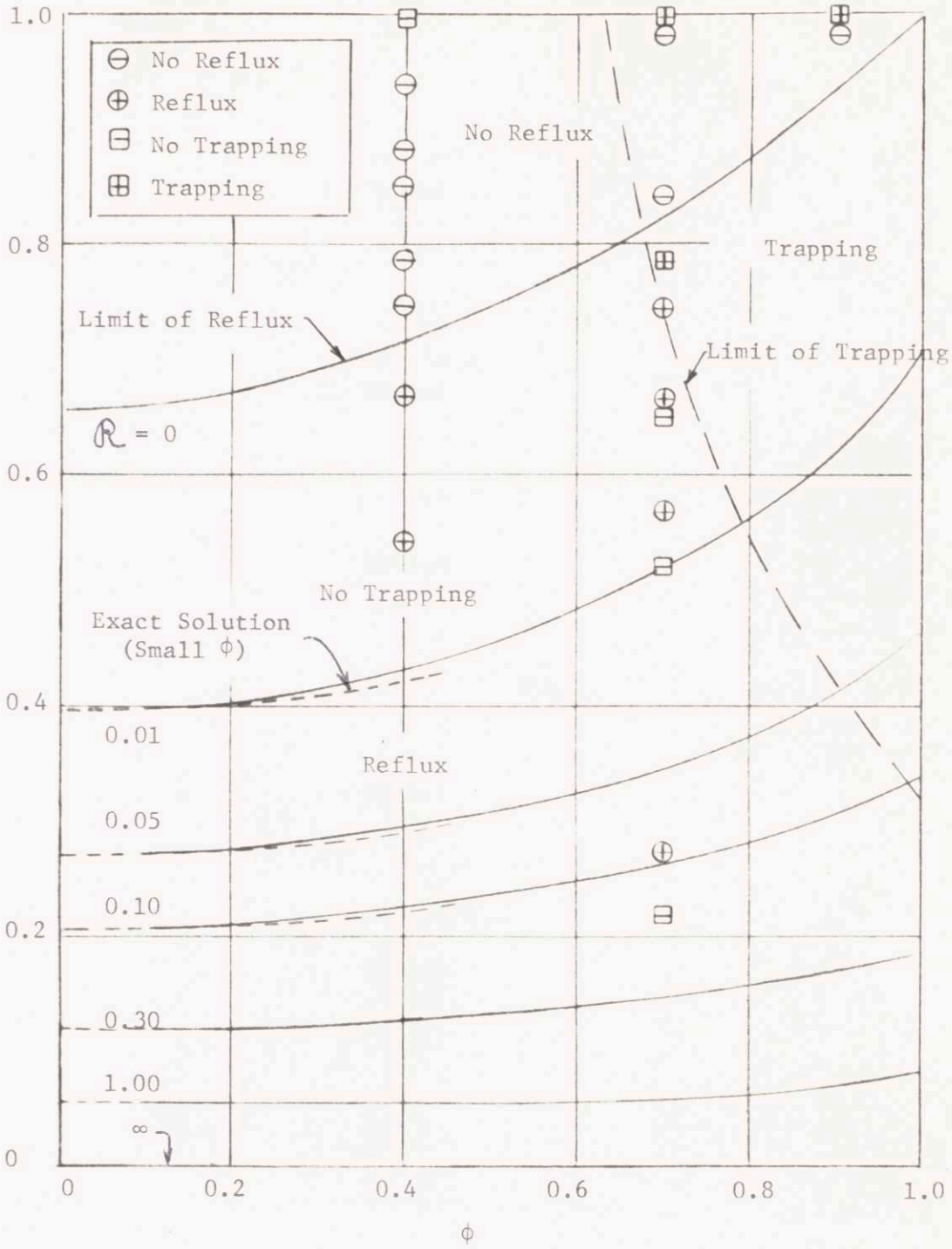
No Reflux
Reflux
No Trapping
Trapping
No Reflux
Trapping
Limit of Reflux
Limit of Trapping
ℛ = 0
No Trapping
Exact Solution
(Small ϕ)
0.01
Reflux
0.05
0.10
0.30
1.00
∞
θ/θ0
ϕ
0
0.2
0.4
0.6
0.8
1.0

FIGURE 14

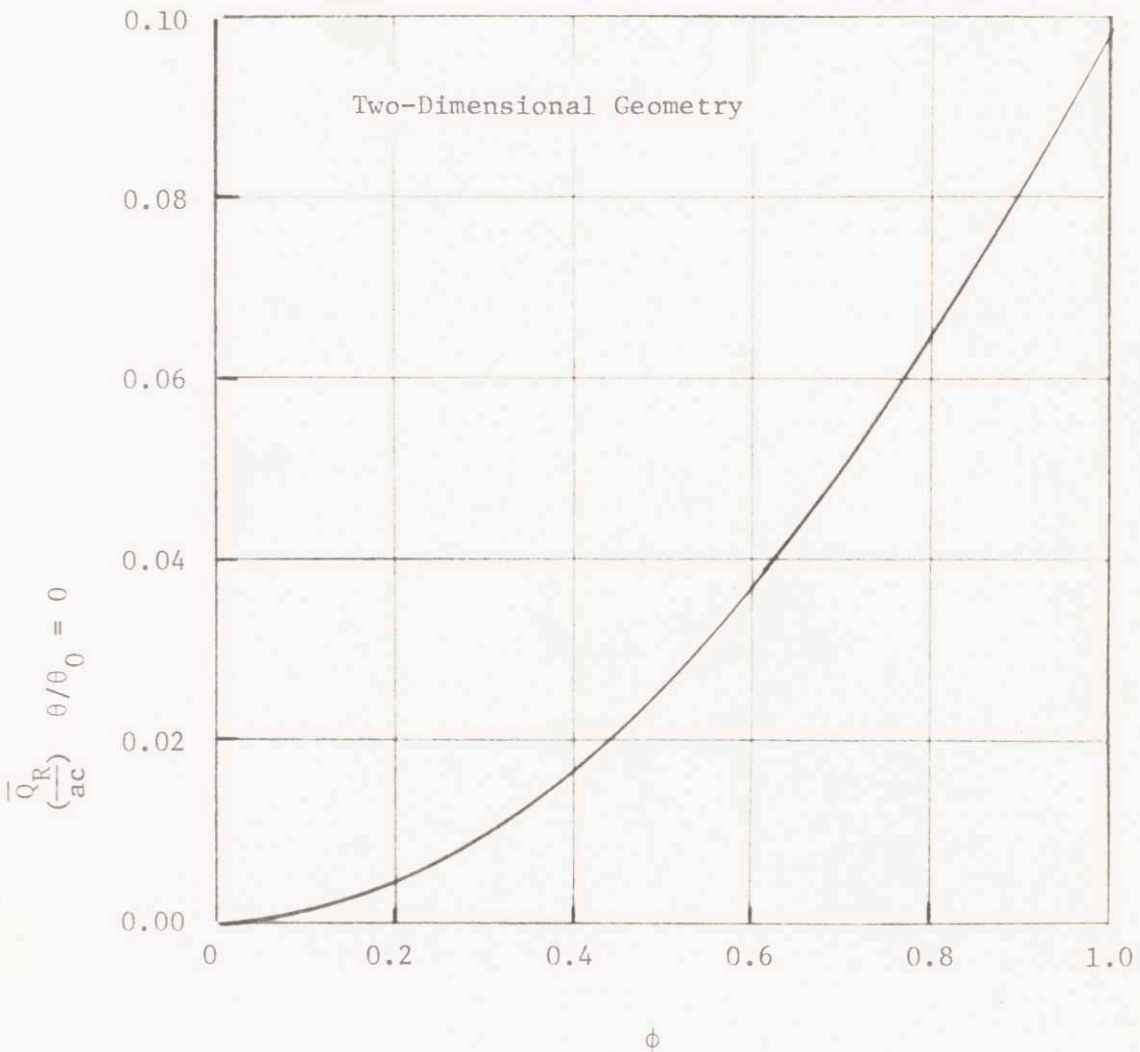
Two-Dimensional Geometry
0.10
0.08
0.06
0.04
0.02
0.00
0
0.2
0.4
0.6
0.8
1.0
$\frac{\bar{Q}_R}{ac}$ $\theta/\theta_0 = 0$
ϕ

FIGURE 15

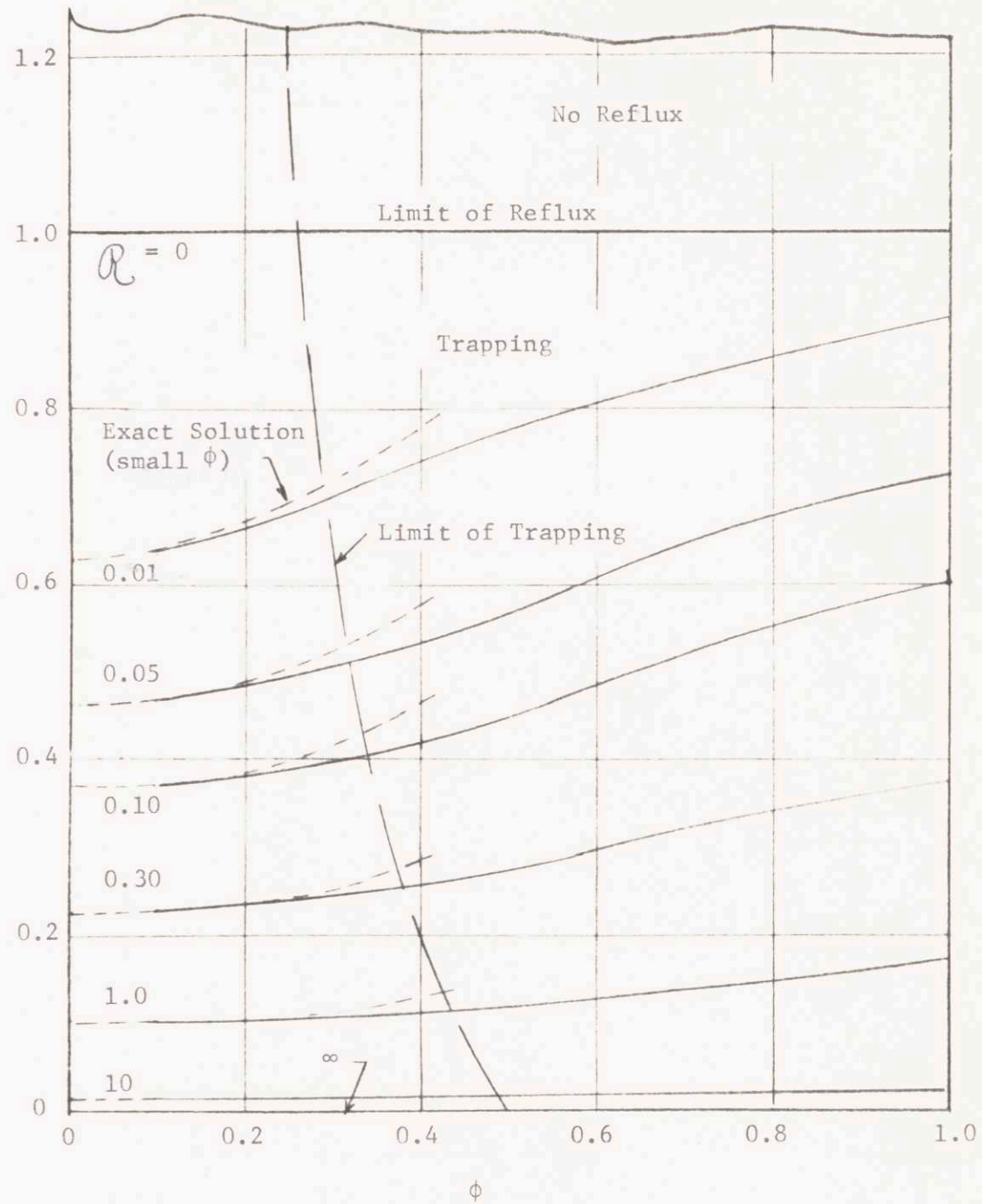
1.2
1.0
0.8
0.6
0.4
0.2
0
No Reflux
Limit of Reflux
$\mathcal{R}$ = 0
Trapping
Exact Solution
(small ϕ)
Limit of Trapping
0.01
0.05
0.10
0.30
1.0
10
∞
0
0.2
0.4
0.6
0.8
1.0
θ/θ0
ϕ

FIGURE 16

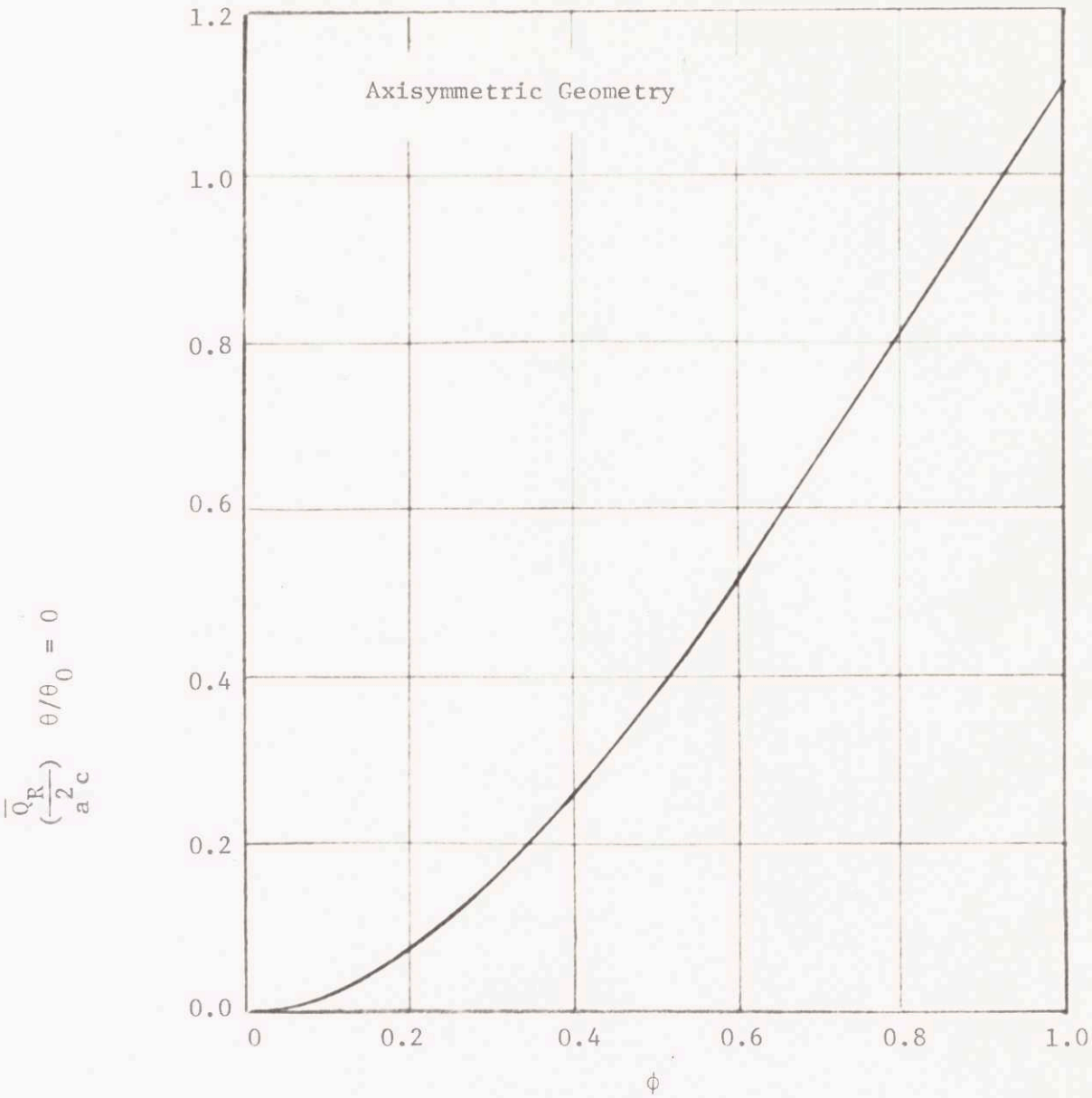
Axisymmetric Geometry
1.2
1.0
0.8
0.6
0.4
0.2
0.0
0
0.2
0.4
0.6
0.8
1.0
ϕ
$\frac{\bar{Q}_R}{(\frac{a}{2})c}$ $\theta/\theta_0 = 0$

FIGURE 17

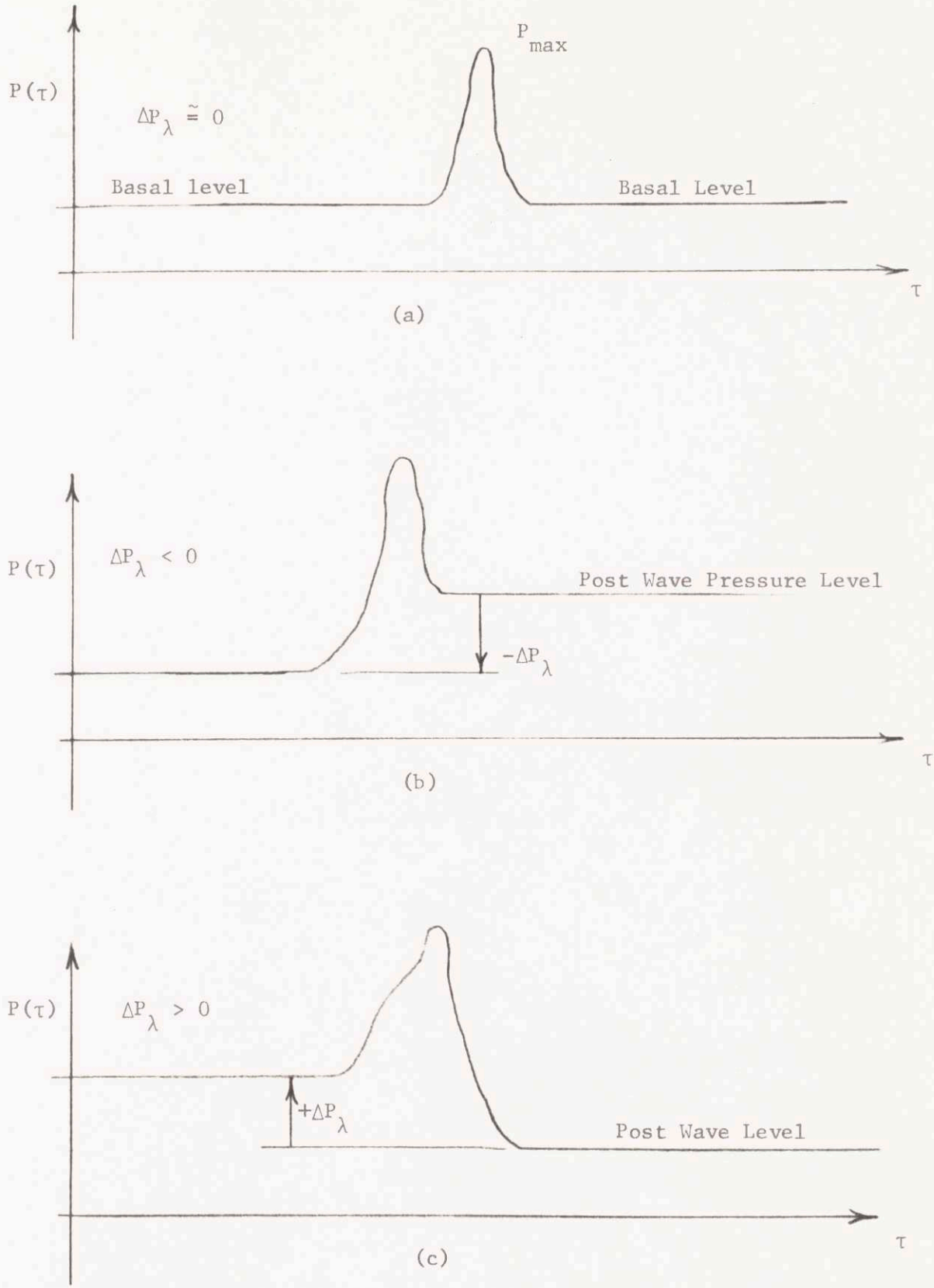
P(τ)
$\Delta P_\lambda \cong 0$
P_{max}
Basal level
Basal Level
τ
(a)
P(τ)
$\Delta P_\lambda < 0$
Post Wave Pressure Level
$-\Delta P_\lambda$
τ
(b)
P(τ)
$\Delta P_\lambda > 0$
$+\Delta P_\lambda$
Post Wave Level
τ
(c)

FIGURE 18

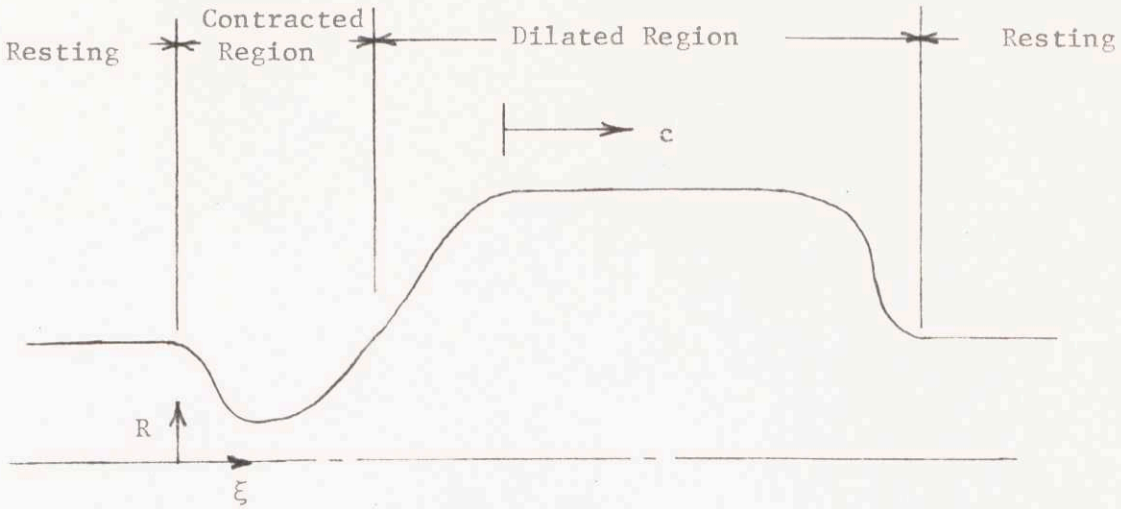

GENERAL WAVE SHAPE

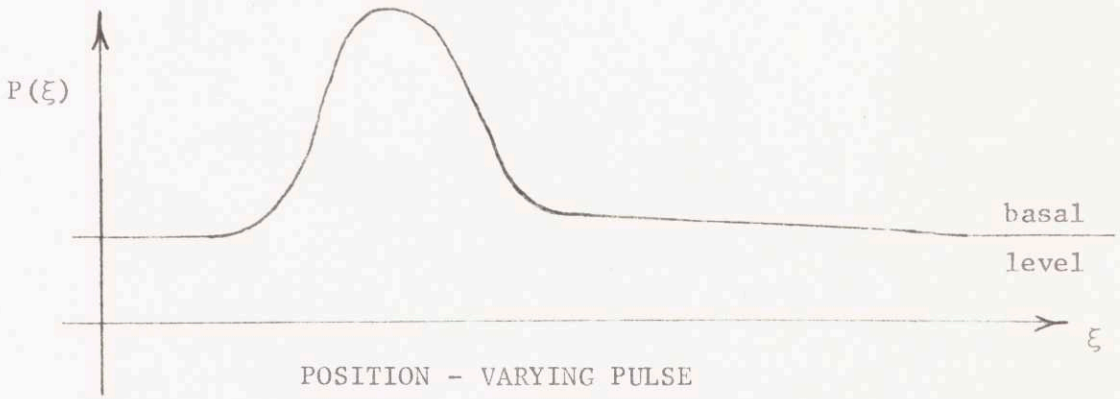

POSITION - VARYING PULSE

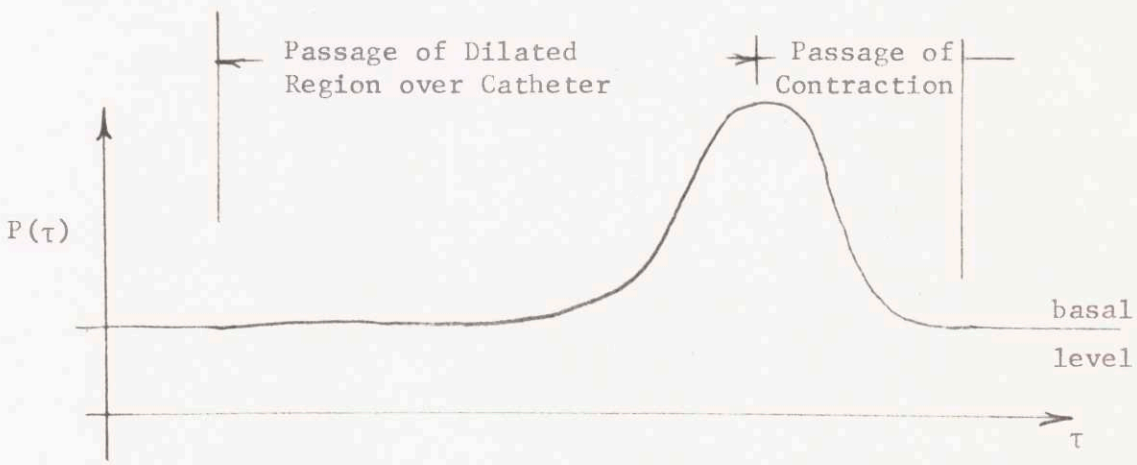

TIME - VARYING PULSE

FIGURE 19

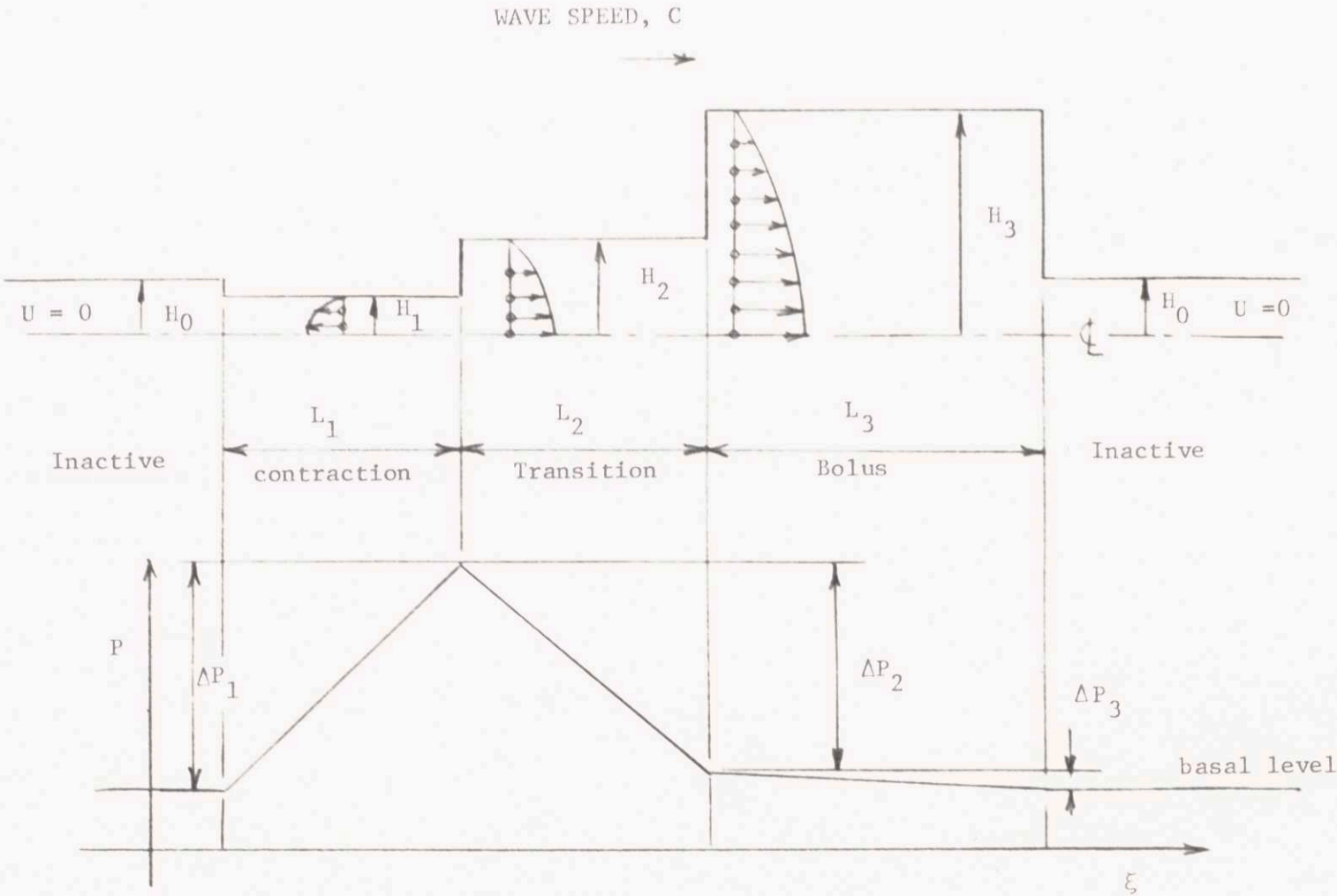
WAVE SPEED, C
U = 0
H_0
H_1
H_2
H_3
H_0
U =0
Inactive
L_1
contraction
L_2
Transition
L_3
Bolus
Inactive
P
ΔP_1
ΔP_2
ΔP_3
basal level
ξ

FIGURE 20

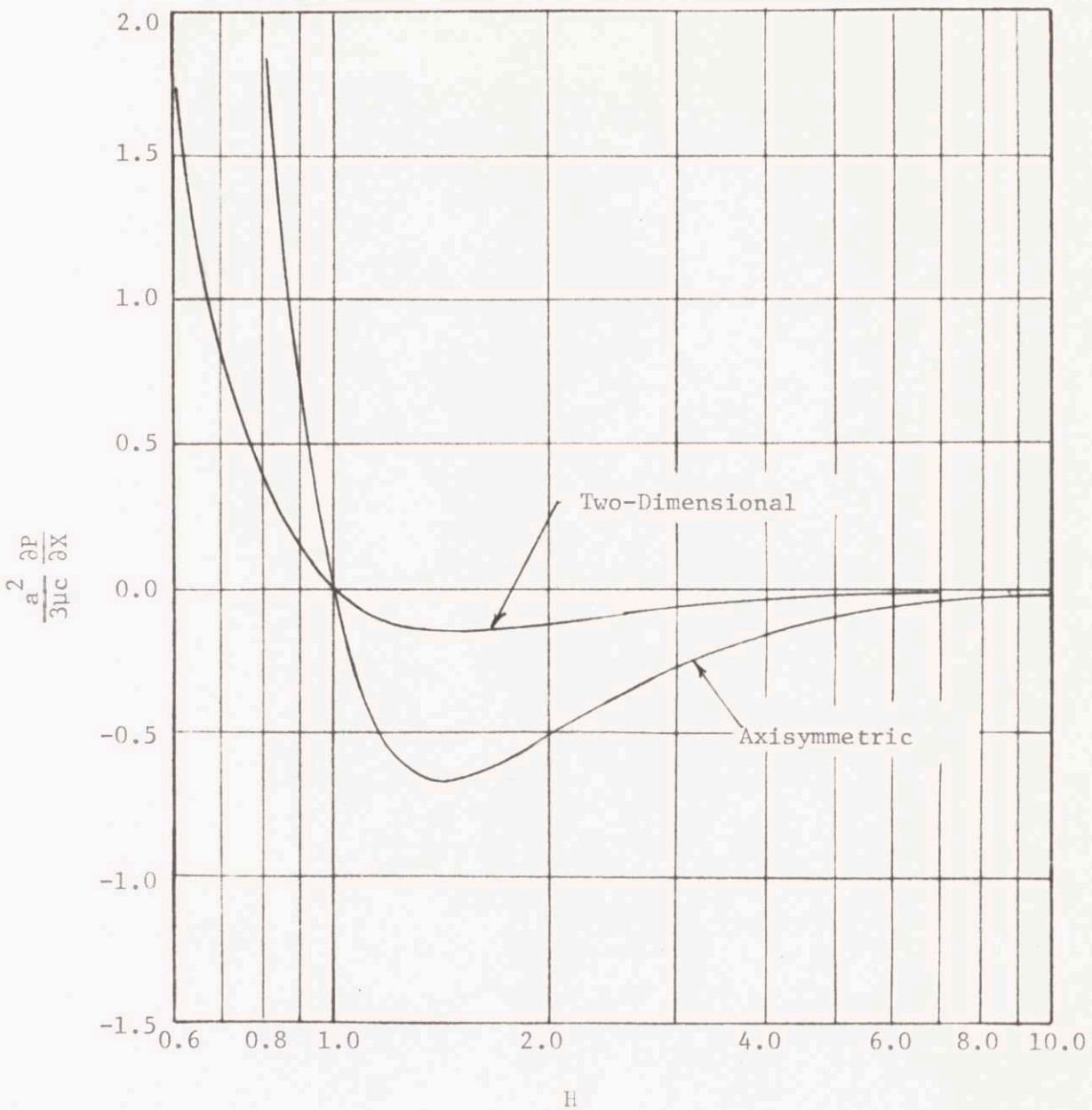
2.0
1.5
1.0
0.5
0.0
-0.5
-1.0
-1.5
0.6
0.8
1.0
2.0
4.0
6.0
8.0
10.0
H
$\frac{a^2}{3\mu c}\frac{\partial P}{\partial X}$
Two-Dimensional
Axisymmetric

FIGURE 21

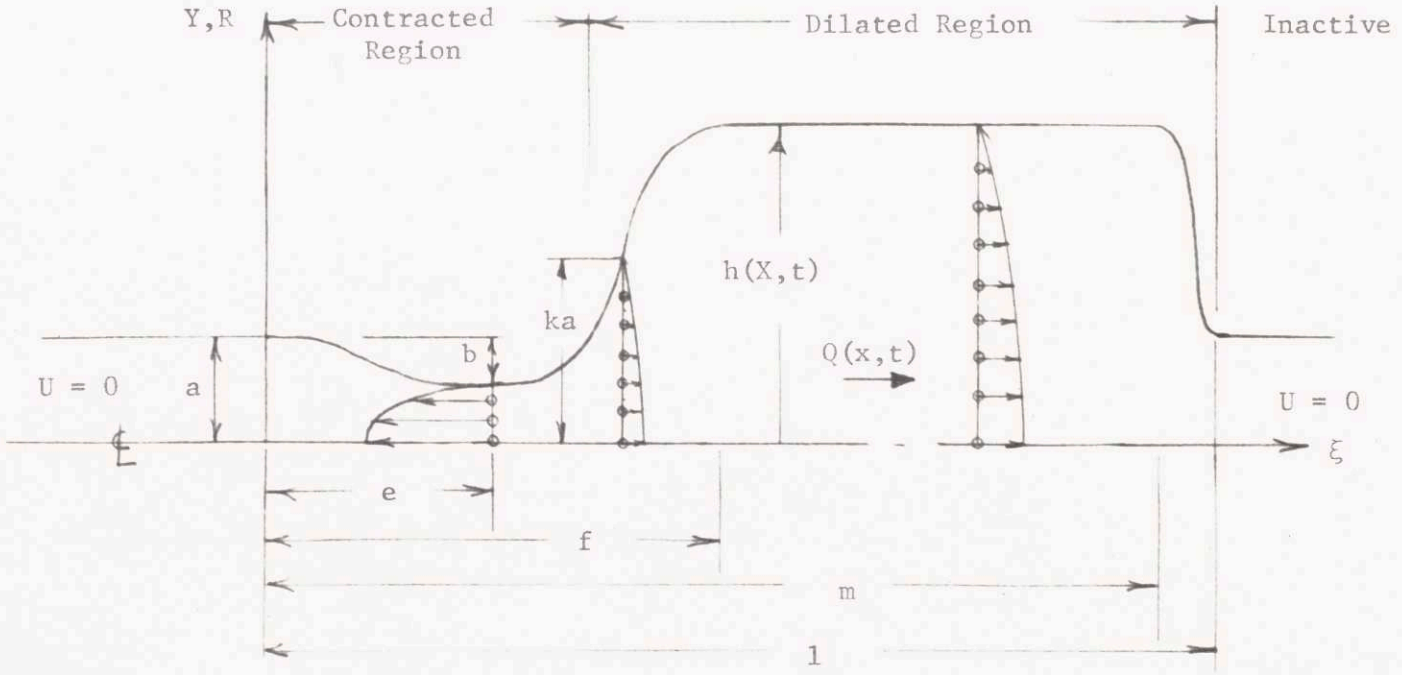

FIGURE 22

Equations

$0 \leq \xi - \tau \leq e$

$$H = (1 - \frac{\phi}{2}) + \frac{\phi}{2} \cos \frac{\pi}{e} (\xi - \tau)$$

$e < \xi - \tau \leq f$

$$H = k - (k - 1 + \phi) \cos \frac{\pi}{j} (\xi - \tau - e)$$

$f < \xi - \tau \leq m$

$$H = 2k + \phi - 1$$

$m < \xi - \tau \leq 1$

$$H = (k + \frac{\phi}{2}) + (k - 1 + \frac{\phi}{2}) \cos \frac{\pi}{\ell} (\xi - \tau - m)$$

where $j = f - e$ and $\ell = 1 - m$

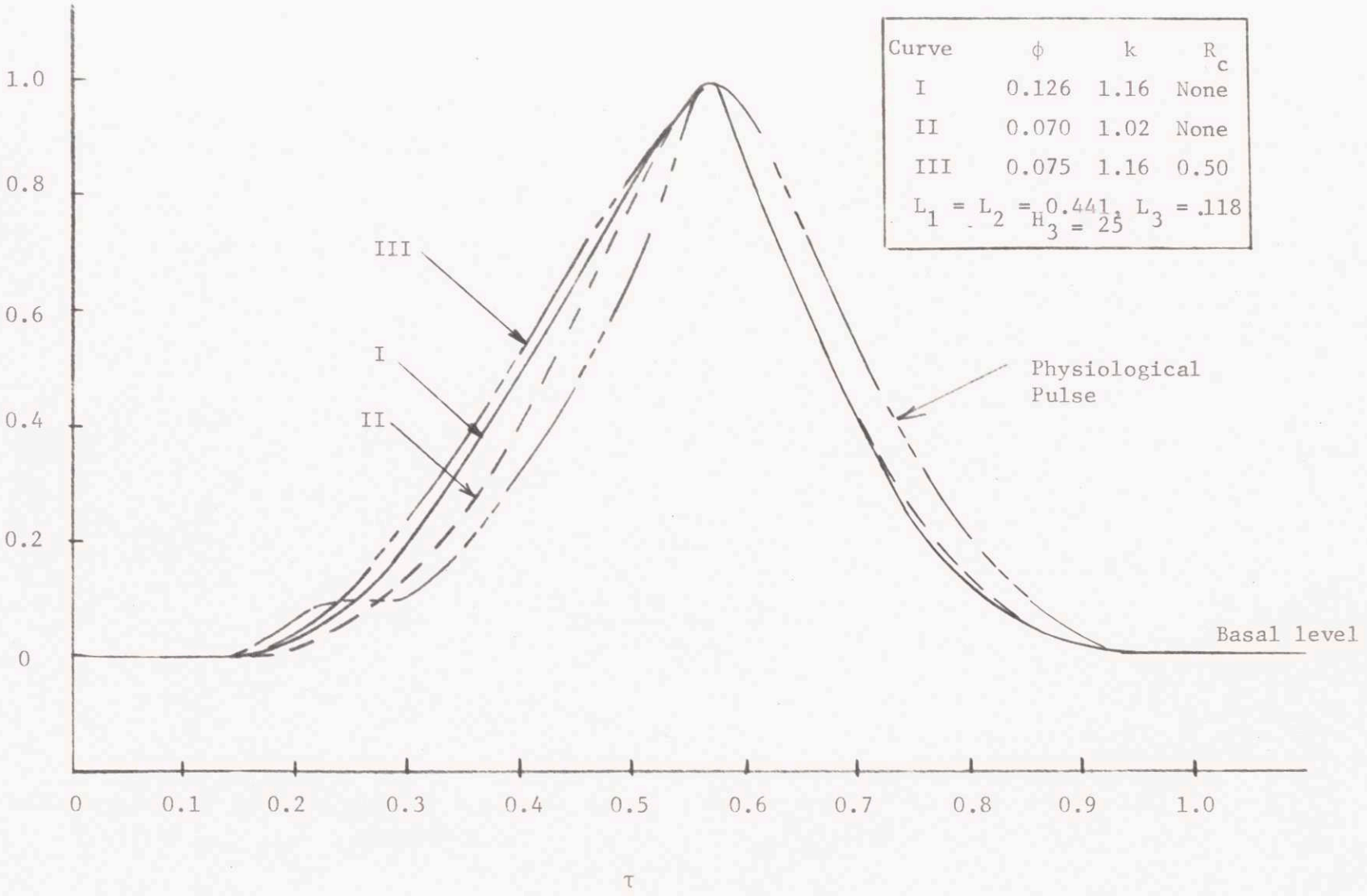
Curve φ k R_c
I 0.126 1.16 None
II 0.070 1.02 None
III 0.075 1.16 0.50
$L_1 = L_2 = 0.441$, $L_3 = .118$
$H_3 = 25$
III
I
II
Physiological Pulse
Basal level
$\frac{P - P_0}{P_{max} - P_0}$
1.0
0.8
0.6
0.4
0.2
0
0 0.1 0.2 0.3 0.4 0.5 0.6 0.7 0.8 0.9 1.0
τ

FIGURE 23

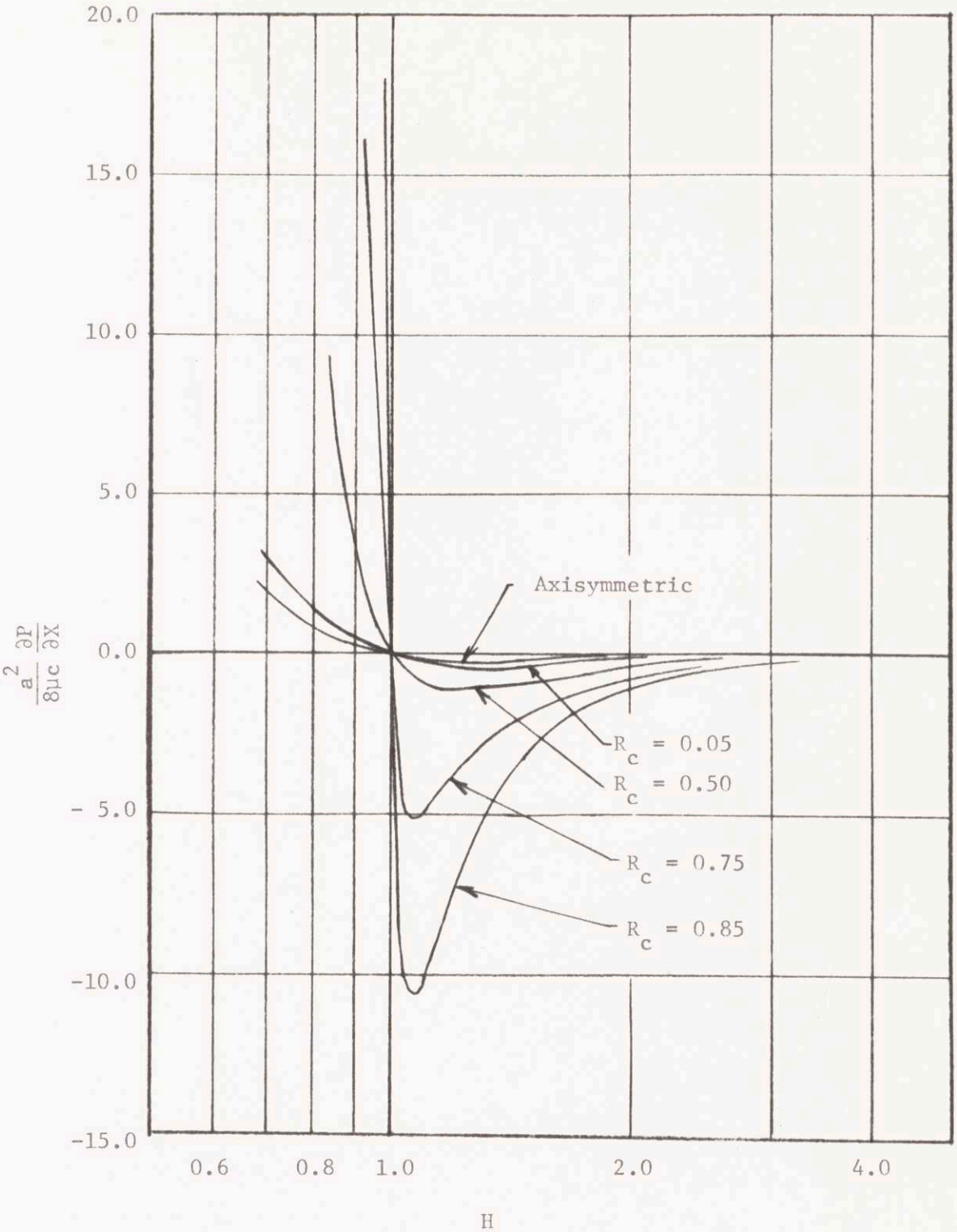
20.0
15.0
10.0
5.0
0.0
- 5.0
-10.0
-15.0
0.6
0.8
1.0
2.0
4.0
H
$\frac{a^2}{8\mu c}\frac{\partial P}{\partial X}$
Axisymmetric
R_c = 0.05
R_c = 0.50
R_c = 0.75
R_c = 0.85

FIGURE 24

AXISYMMETRIC

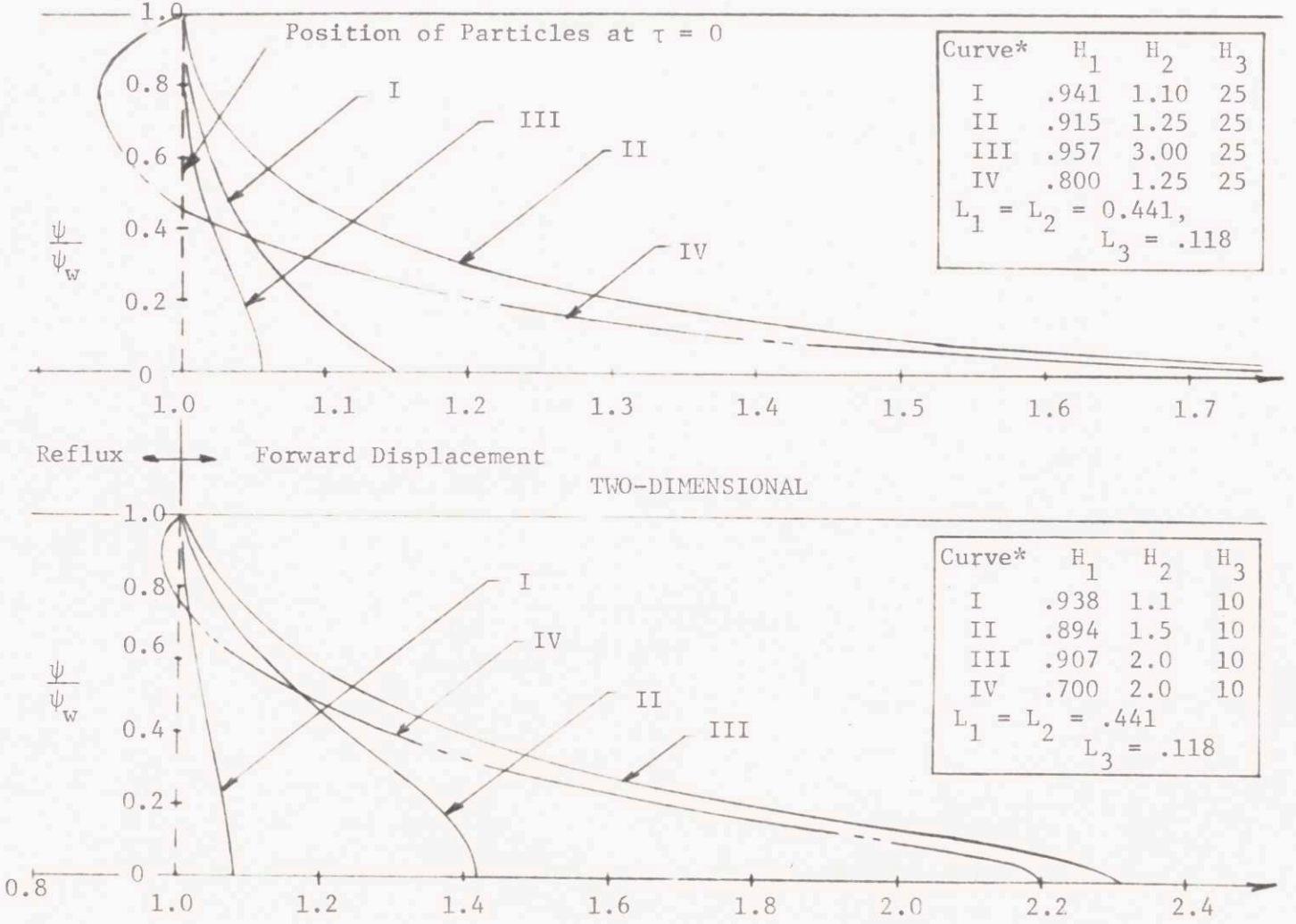

*Particle on $\psi/\psi_w = 0$ is trapped at stagnation point of bolus.

FIGURE 25

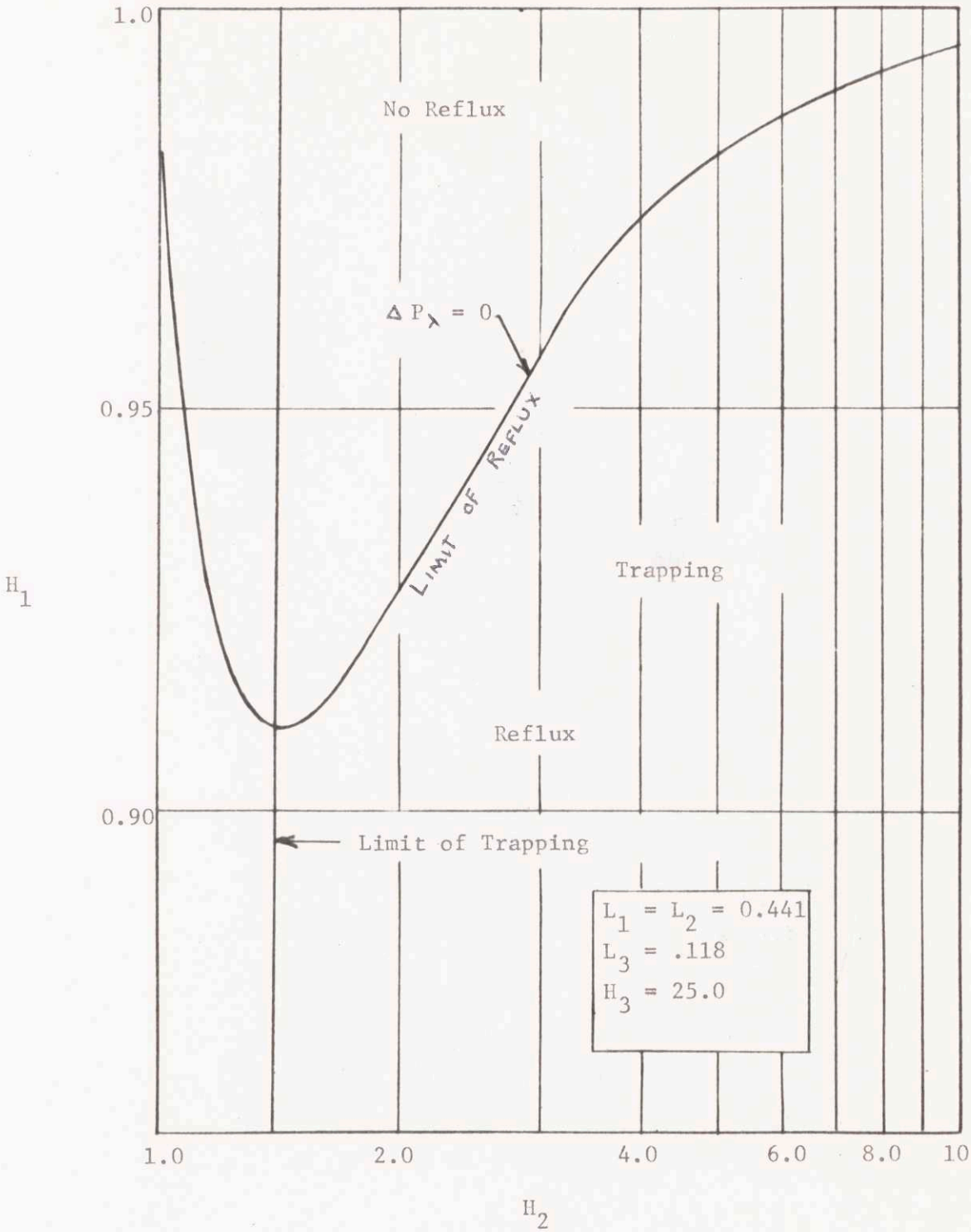
1.0
0.95
0.90
No Reflux
$\Delta P_1 = 0$
Limit of Reflux
Trapping
Reflux
Limit of Trapping
$L_1 = L_2 = 0.441$
$L_3 = .118$
$H_3 = 25.0$
1.0
2.0
4.0
6.0
8.0
10
H_1
H_2

FIGURE 26

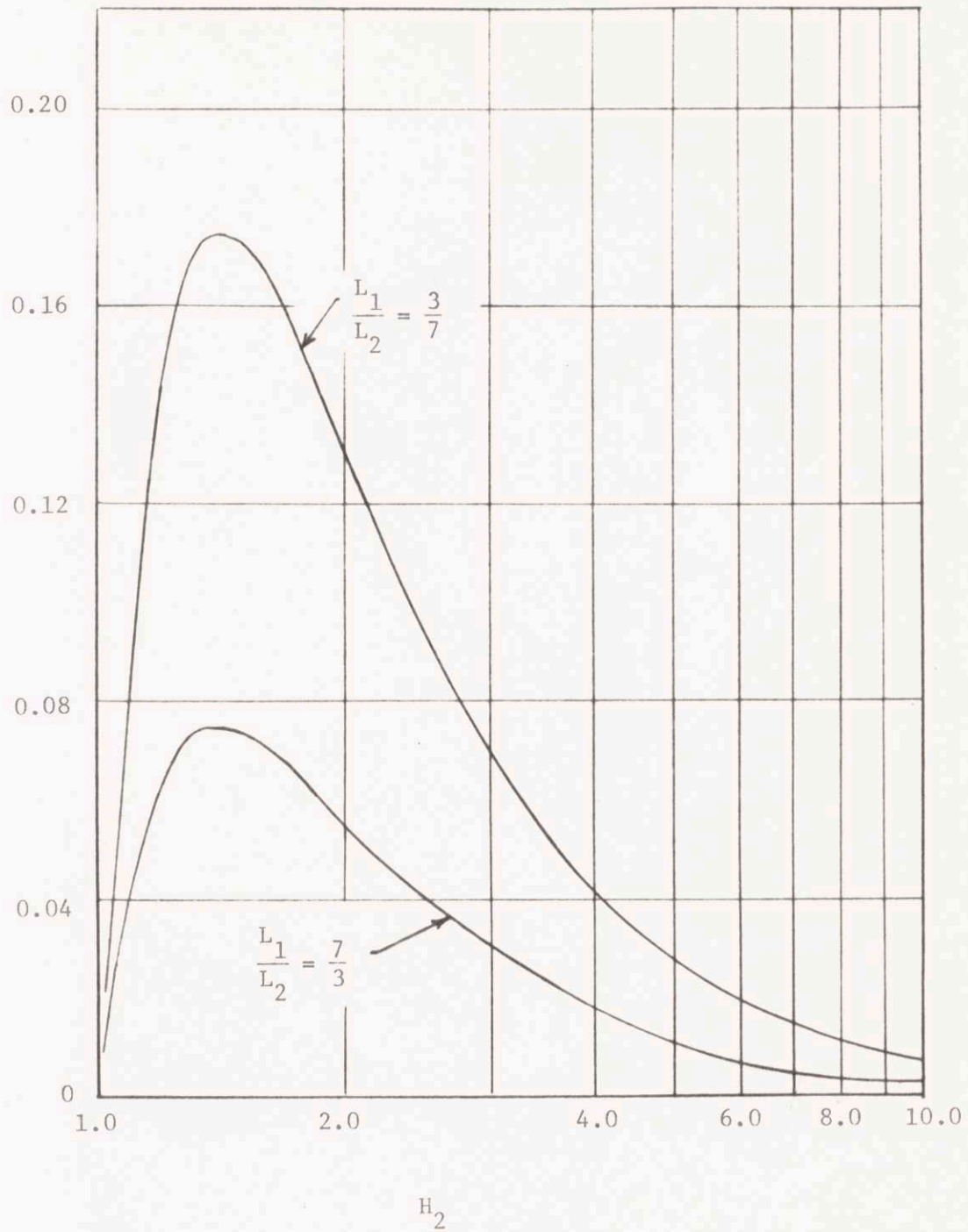
0.20
0.16
0.12
0.08
0.04
0
$\frac{L_1}{L_2} = \frac{3}{7}$
$\frac{L_1}{L_2} = \frac{7}{3}$
1.0
2.0
4.0
6.0
8.0
10.0
H_2
$\tilde{p}_{max} - \tilde{p}_0$

FIGURE 27

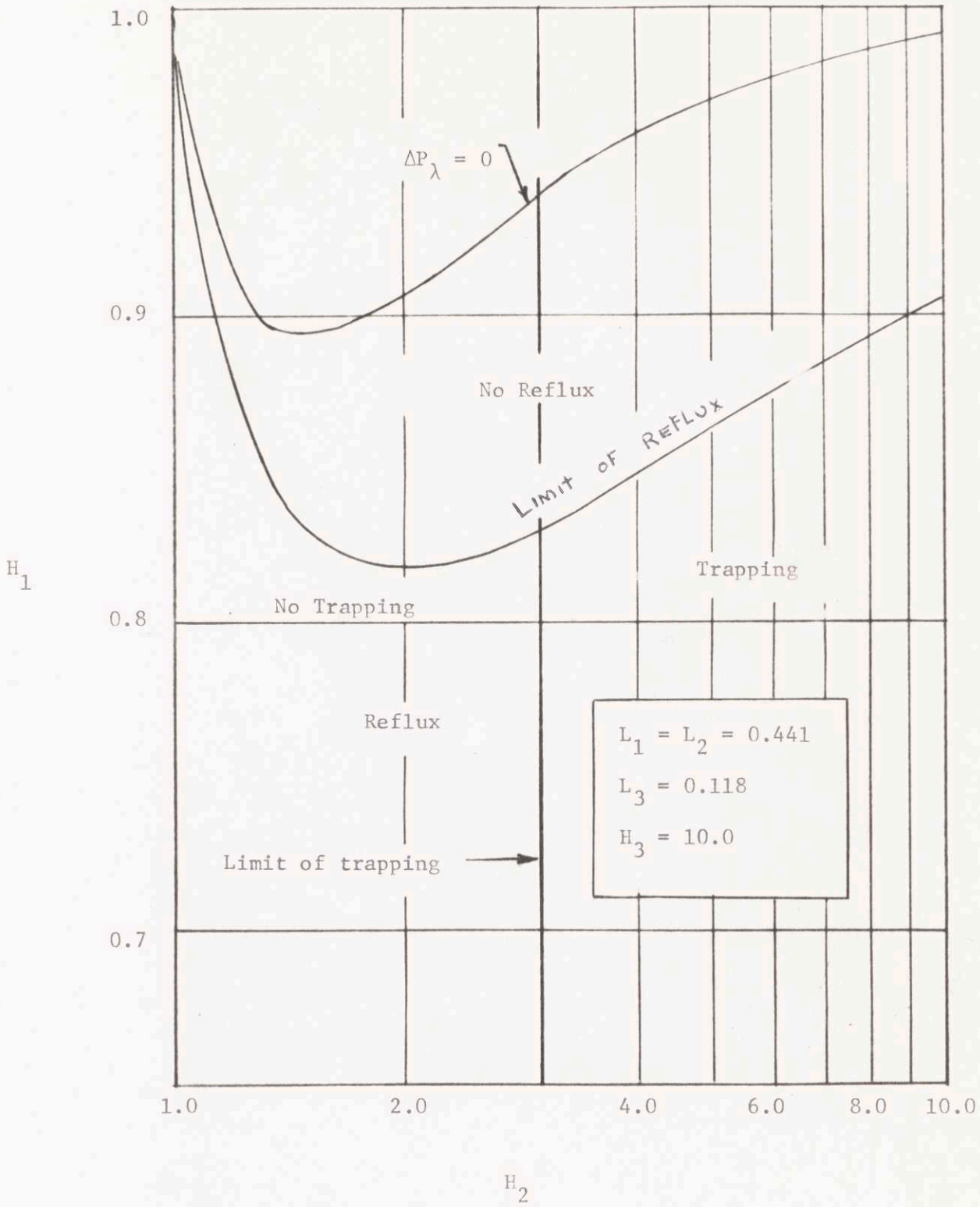
1.0
0.9
0.8
0.7
H_1
$\Delta P_\lambda = 0$
No Reflux
Limit of Reflux
Trapping
No Trapping
Reflux
Limit of trapping
$L_1 = L_2 = 0.441$
$L_3 = 0.118$
$H_3 = 10.0$
1.0
2.0
4.0
6.0
8.0
10.0
H_2

FIGURE 28

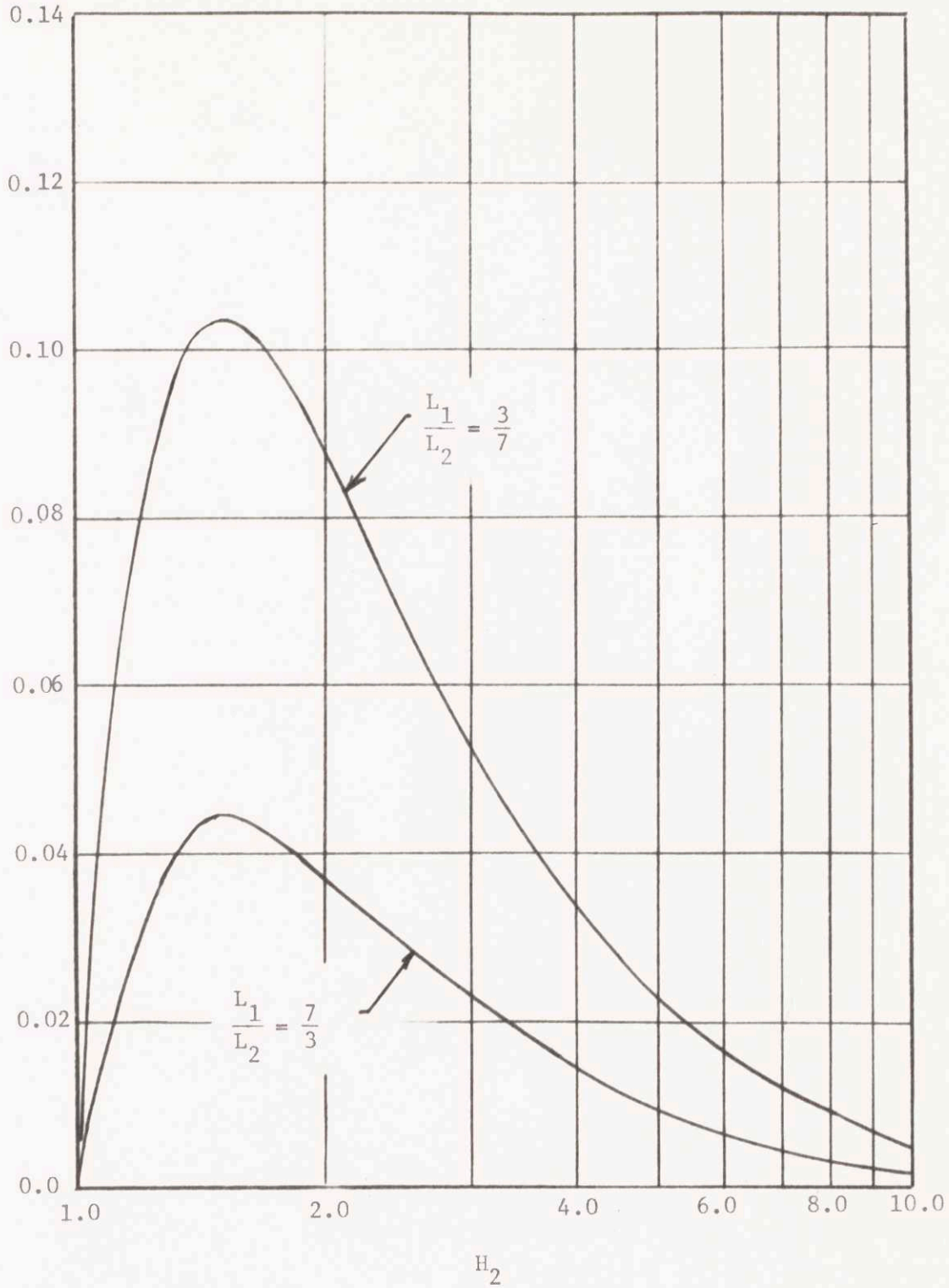
0.14
0.12
0.10
0.08
0.06
0.04
0.02
0.0
$\frac{L_1}{L_2} = \frac{3}{7}$
$\frac{L_1}{L_2} = \frac{7}{3}$
1.0
2.0
4.0
6.0
8.0
10.0
H_2

FIGURE 29

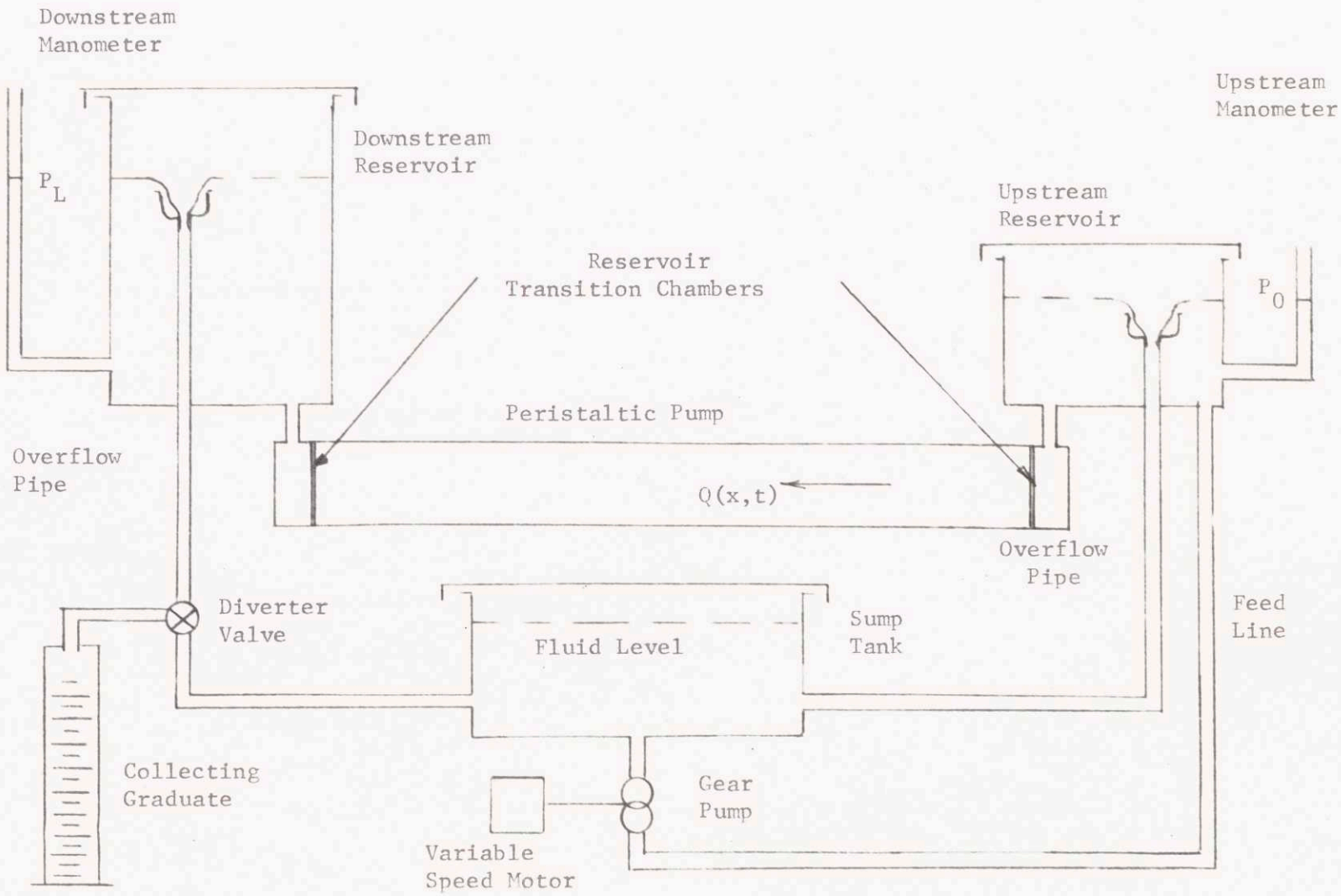
Downstream
Manometer
Upstream
Manometer
Downstream
Reservoir
P_L
Upstream
Reservoir
Reservoir
Transition Chambers
P_0
Peristaltic Pump
Overflow
Pipe
Q(x,t)
Overflow
Pipe
Diverter
Valve
Fluid Level
Sump
Tank
Feed
Line
Collecting
Graduate
Gear
Pump
Variable
Speed Motor

FIGURE 30

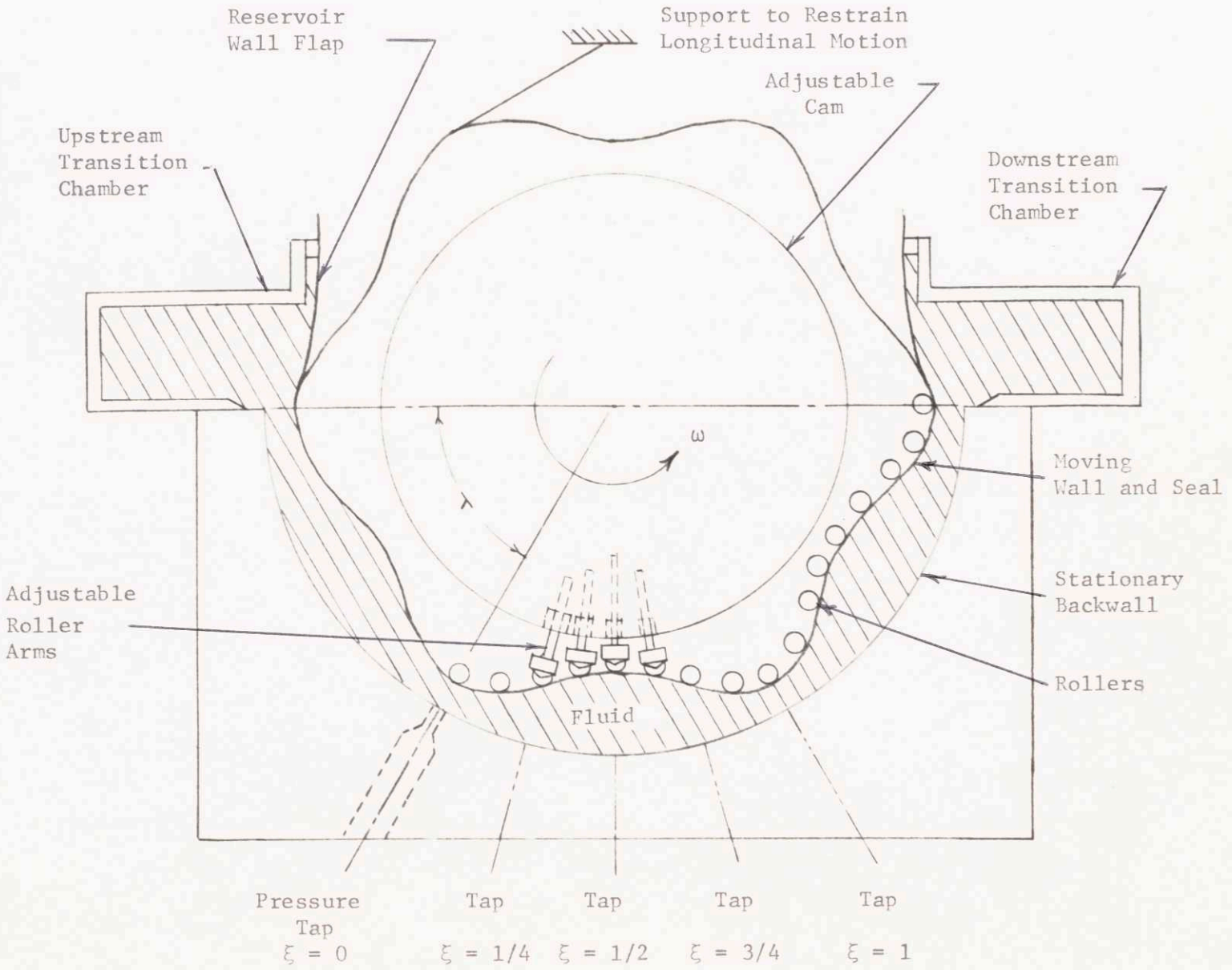
Reservoir
Wall Flap
Support to Restrain
Longitudinal Motion
Adjustable
Cam
Upstream
Transition
Chamber
Downstream
Transition
Chamber
ω
Moving
Wall and Seal
Stationary
Backwall
Adjustable
Roller
Arms
Rollers
Fluid
Pressure
Tap
ξ = 0
Tap
ξ = 1/4
Tap
ξ = 1/2
Tap
ξ = 3/4
Tap
ξ = 1

FIGURE 31

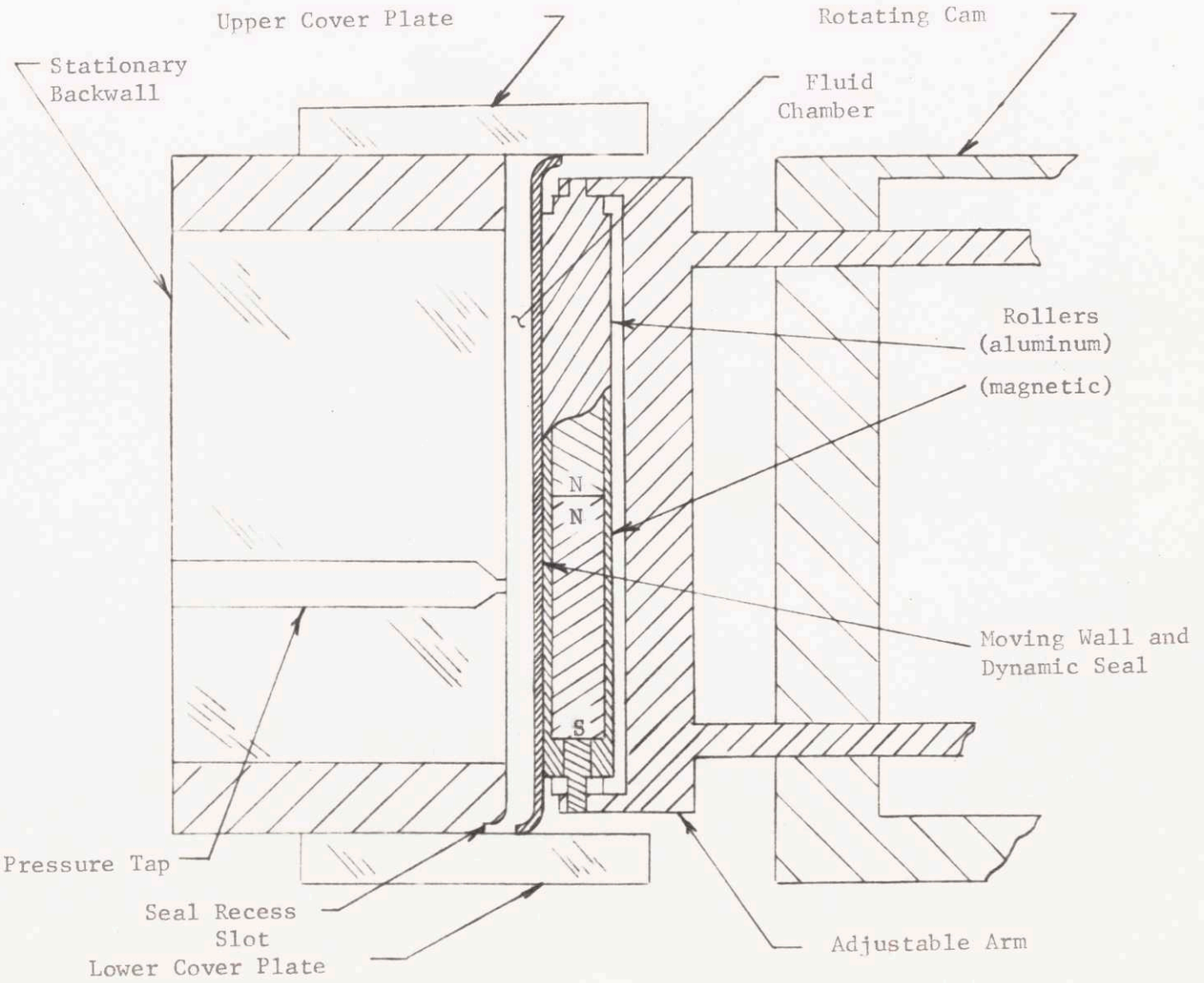
Upper Cover Plate
Rotating Cam
Stationary
Backwall
Fluid
Chamber
Rollers
(aluminum)
(magnetic)
N
N
Moving Wall and
Dynamic Seal
S
Pressure Tap
Seal Recess
Slot
Lower Cover Plate
Adjustable Arm

FIGURE 32

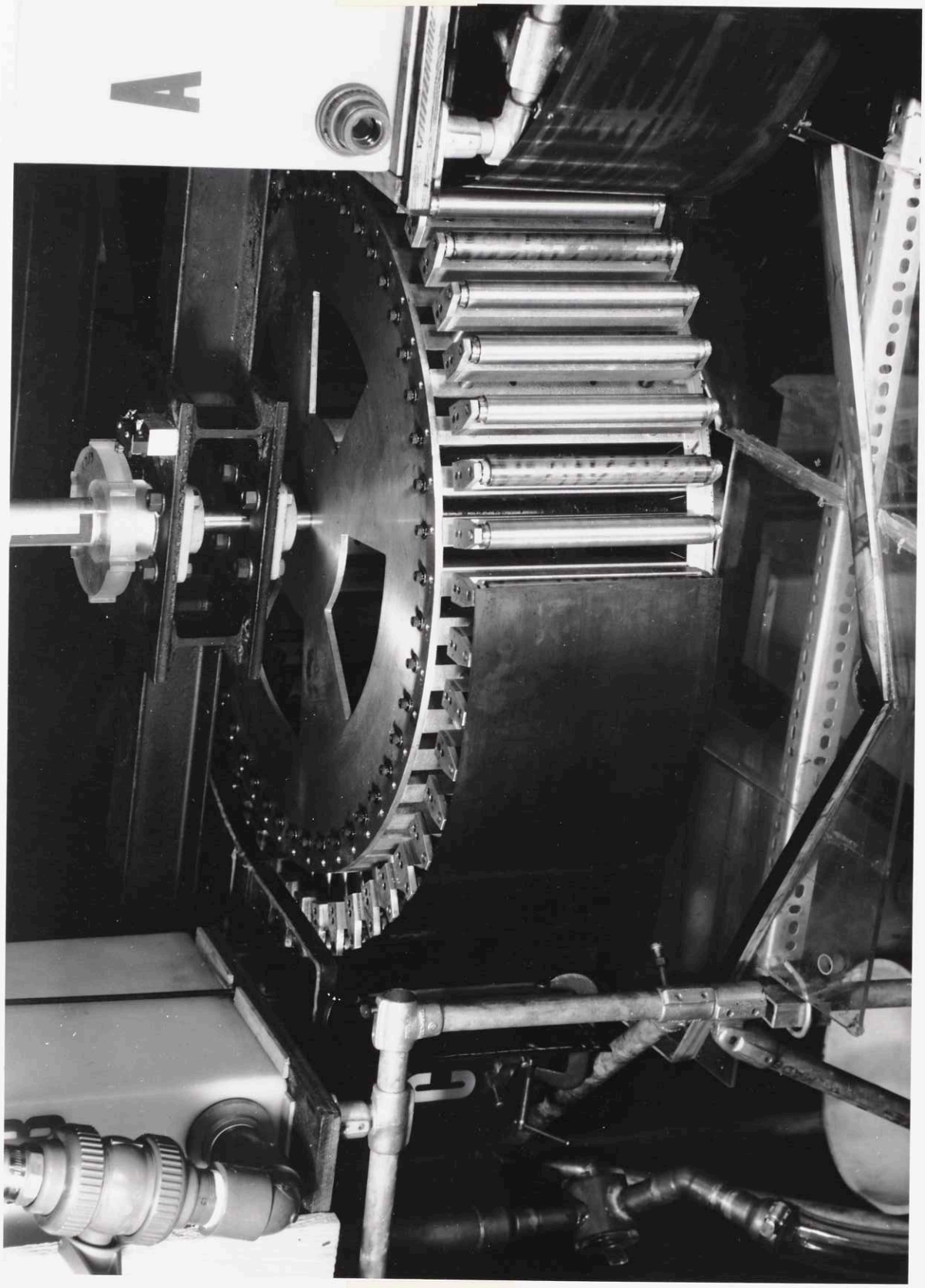

FIGURE 33

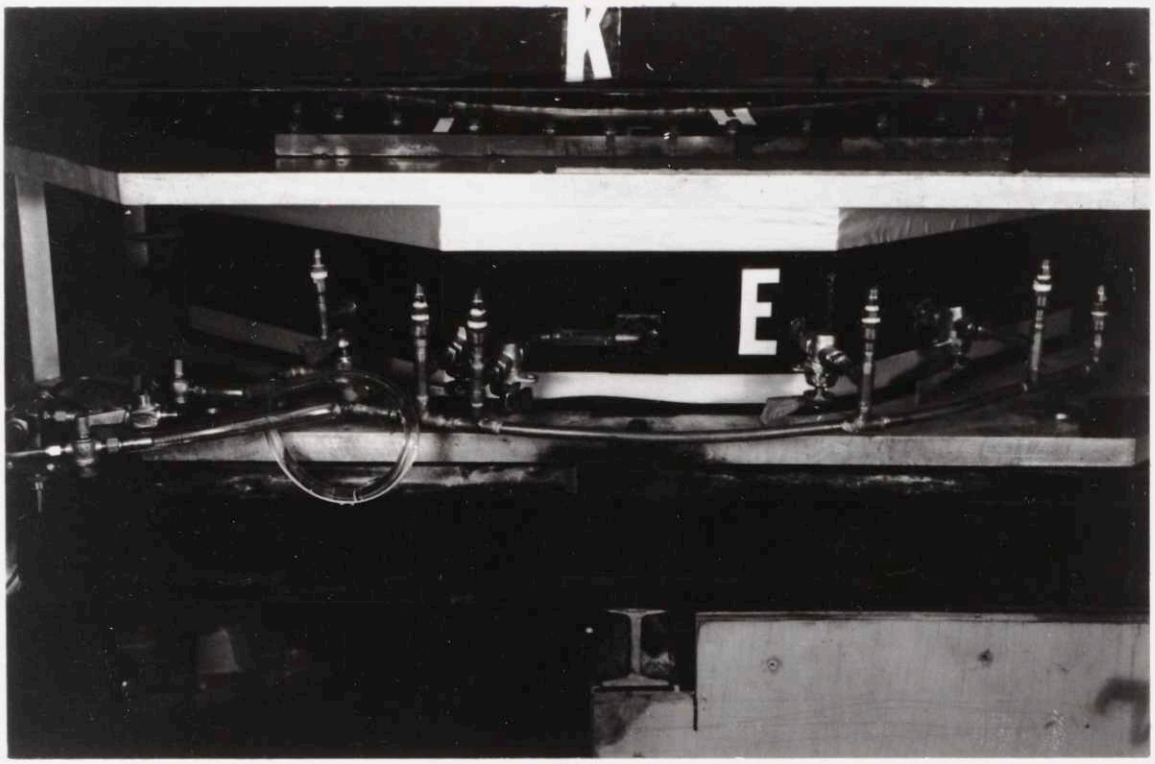

(a)

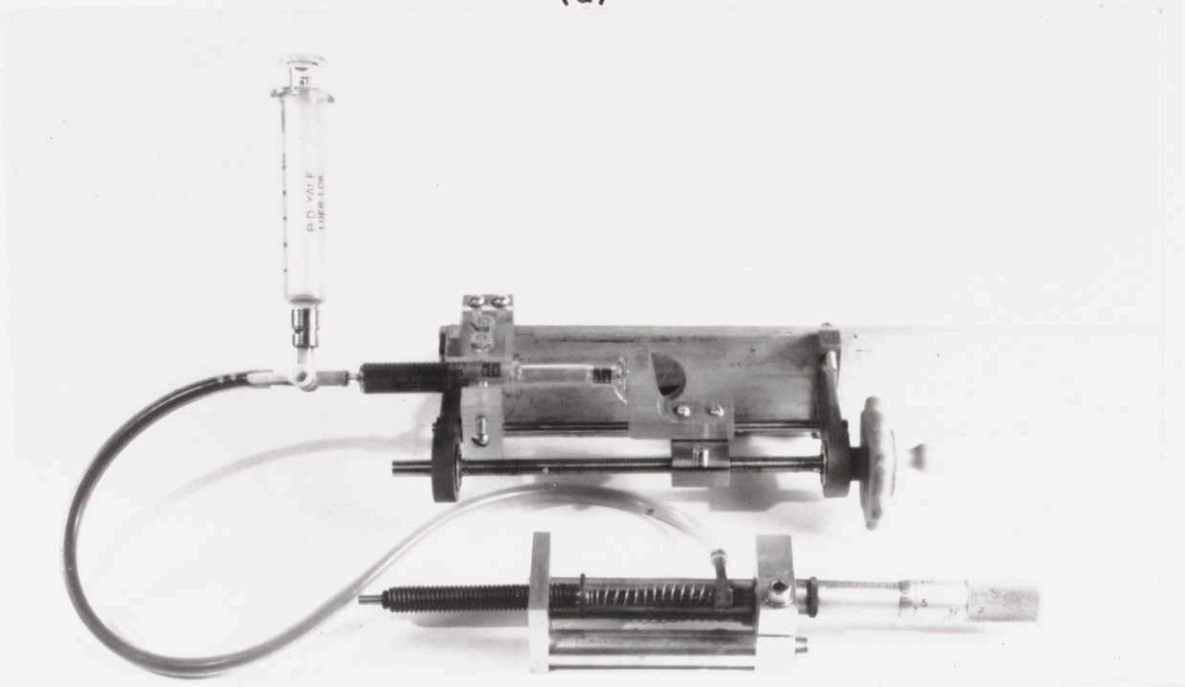

(b)

FIGURE 34

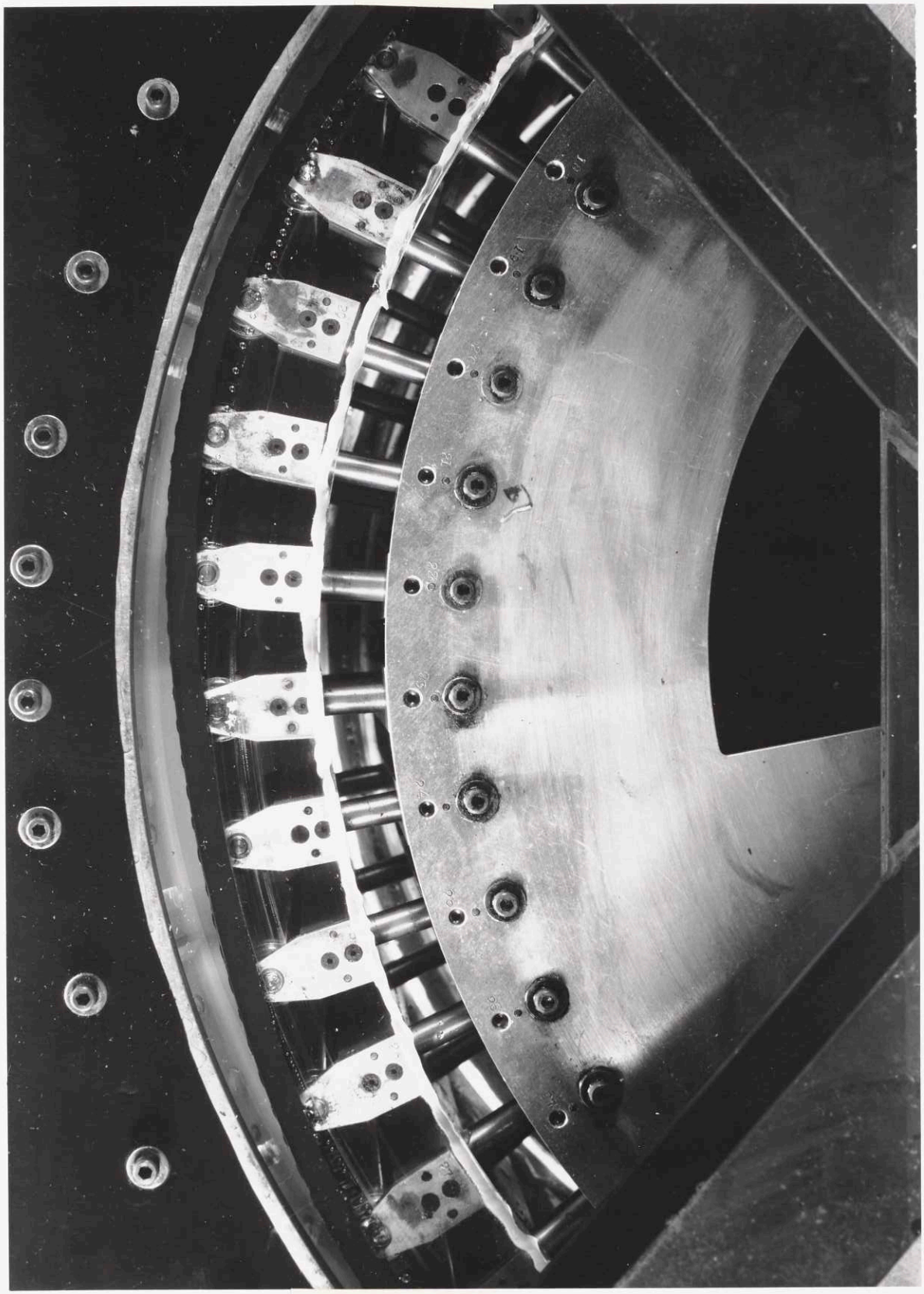

FIGURE 35

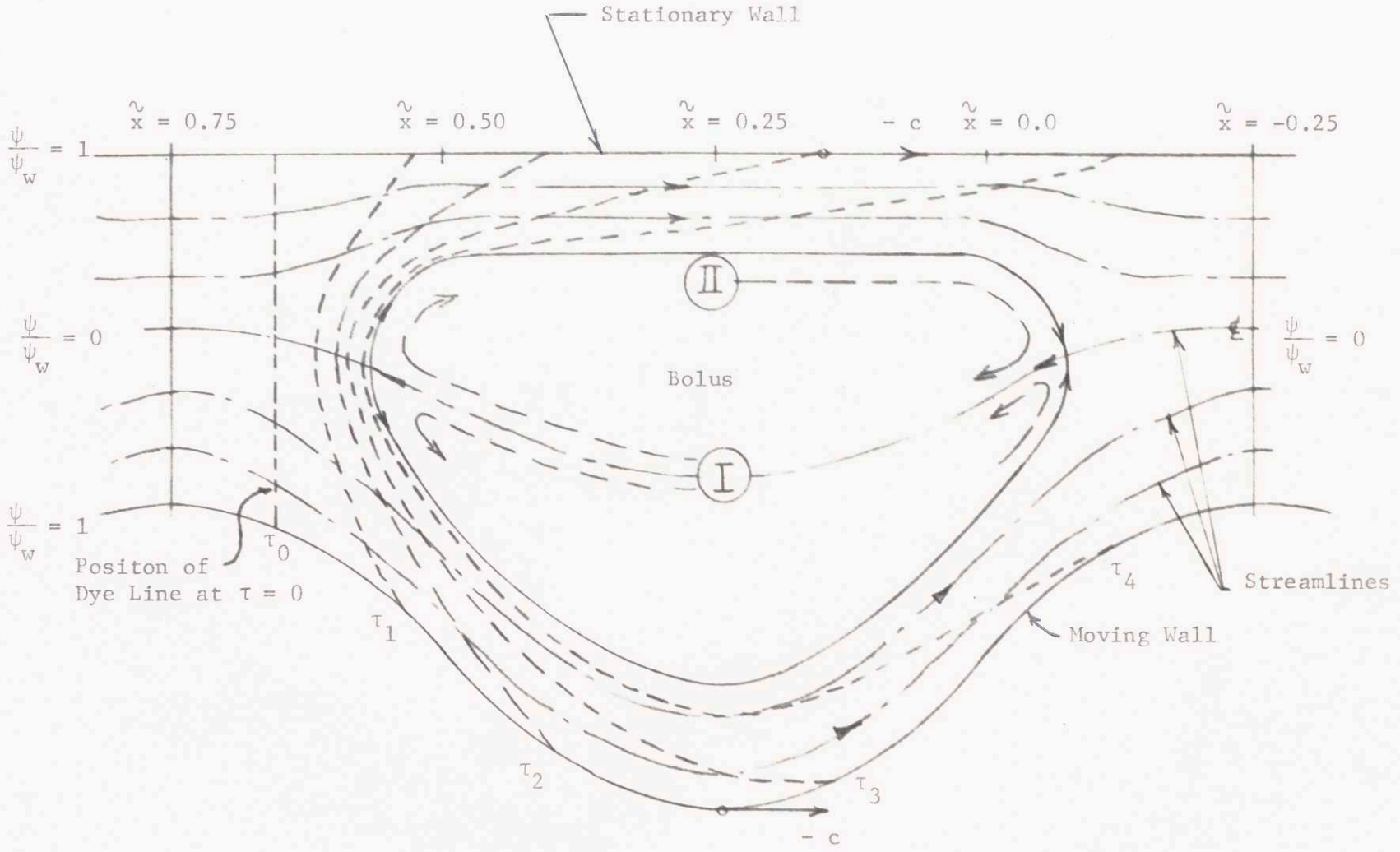
Stationary Wall
$\tilde{x}$ = 0.75
$\tilde{x}$ = 0.50
$\tilde{x}$ = 0.25
- c
$\tilde{x}$ = 0.0
$\tilde{x}$ = -0.25
$\frac{\psi}{\psi_w}$ = 1
$\frac{\psi}{\psi_w}$ = 0
$\frac{\psi}{\psi_w}$ = 1
$\frac{\psi}{\psi_w}$ = 0
II
I
Bolus
Positon of
Dye Line at τ = 0
τ_0
τ_1
τ_2
τ_3
τ_4
Streamlines
Moving Wall
- c

FIGURE 36

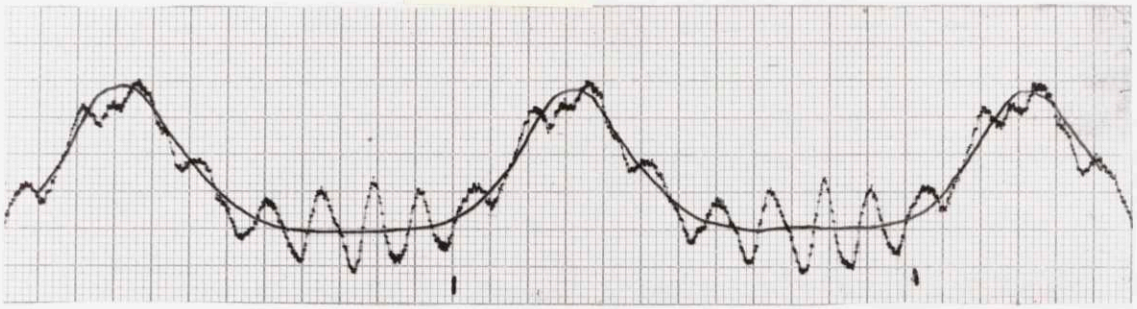

$P_\xi \equiv 1/4 - P_o$

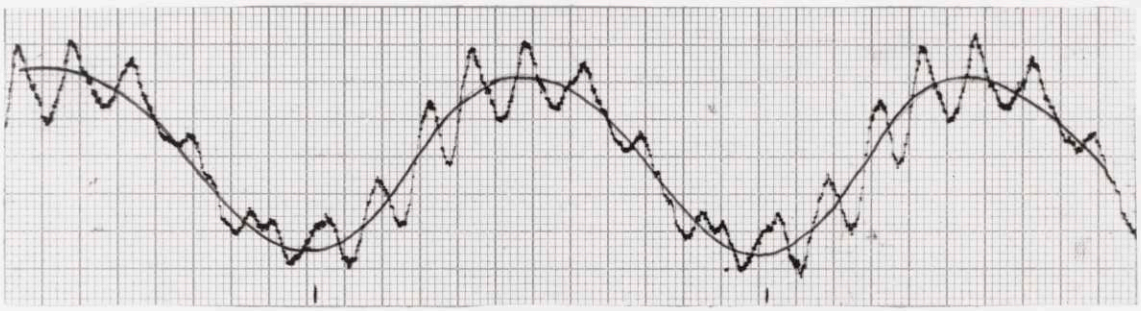

$P_\xi = 1/2 - P_o$

$P_\xi = 3/4 - P_o$

$P_\xi = \lambda - P_o$

$\phi = 0.4$ $\theta/\theta_o = 0.0$

FIGURE 37

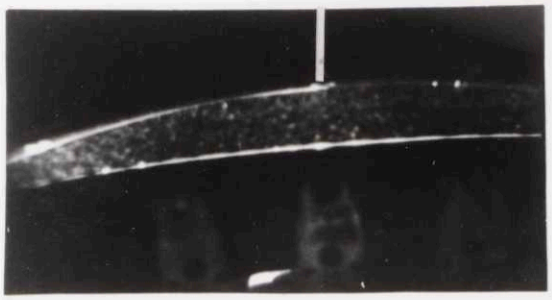

$\tau = 0.0$

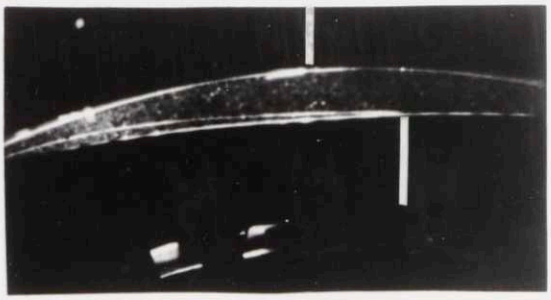

$\tau = 0.0$

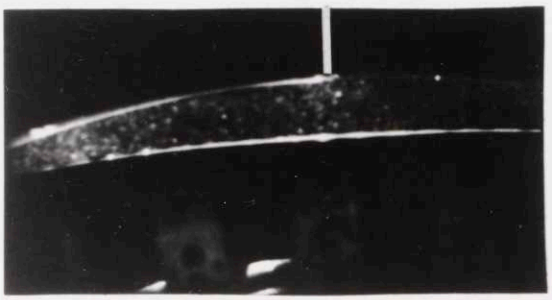

$\tau = 2.0$

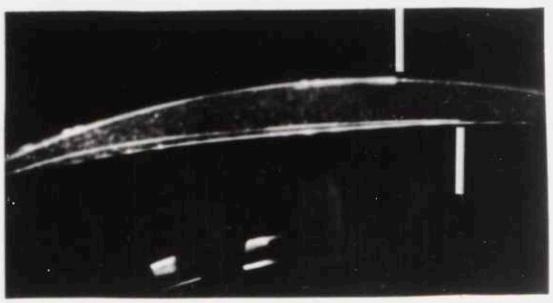

$\tau = 1.0$

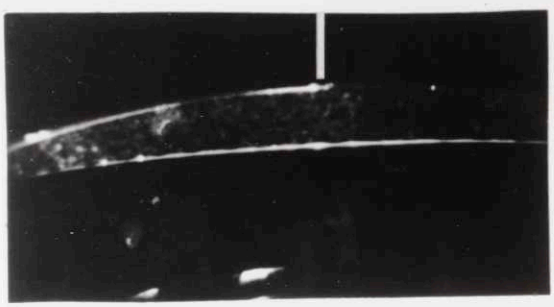

$\tau = 3.0$

$\tau = 3.0$

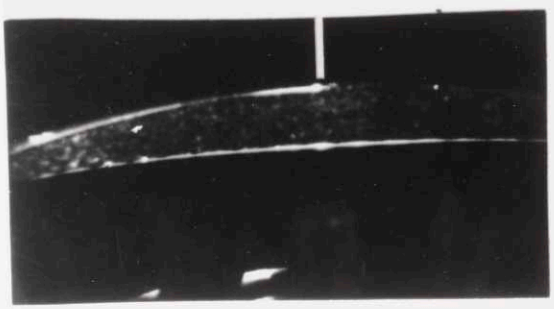

$\tau = 4.0$

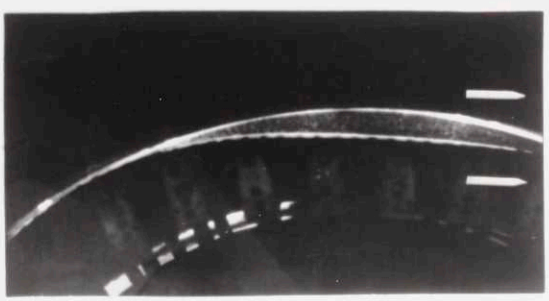

$\tau = 10.0$

NO REFLUX $\theta/\theta_0 = 0.84$ REFLUX $\theta/\theta_0 = 0.57$

FIGURE 38

$\tau = 0.0$

$\tau = 0.368$

$\tau = 0.066$

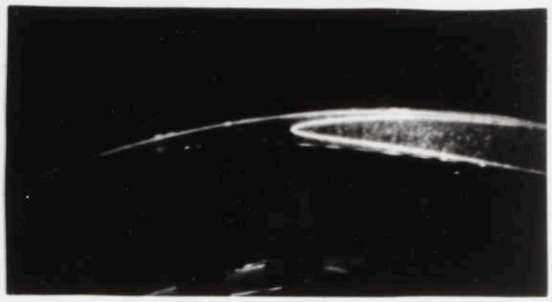

$\tau = 0.532$

$\tau = 0.204$

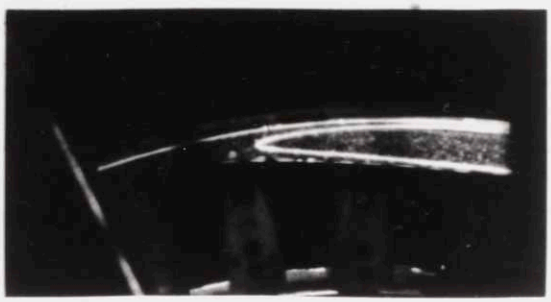

$\tau = 0.695$

$\tau = 0.287$

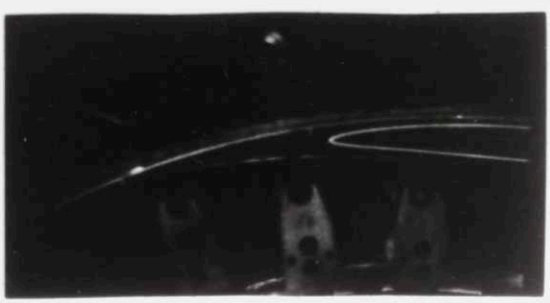

$\tau = 1.190$

$\phi = 0.7$ $\theta/\theta_0 = 1.0$

FIGURE 39

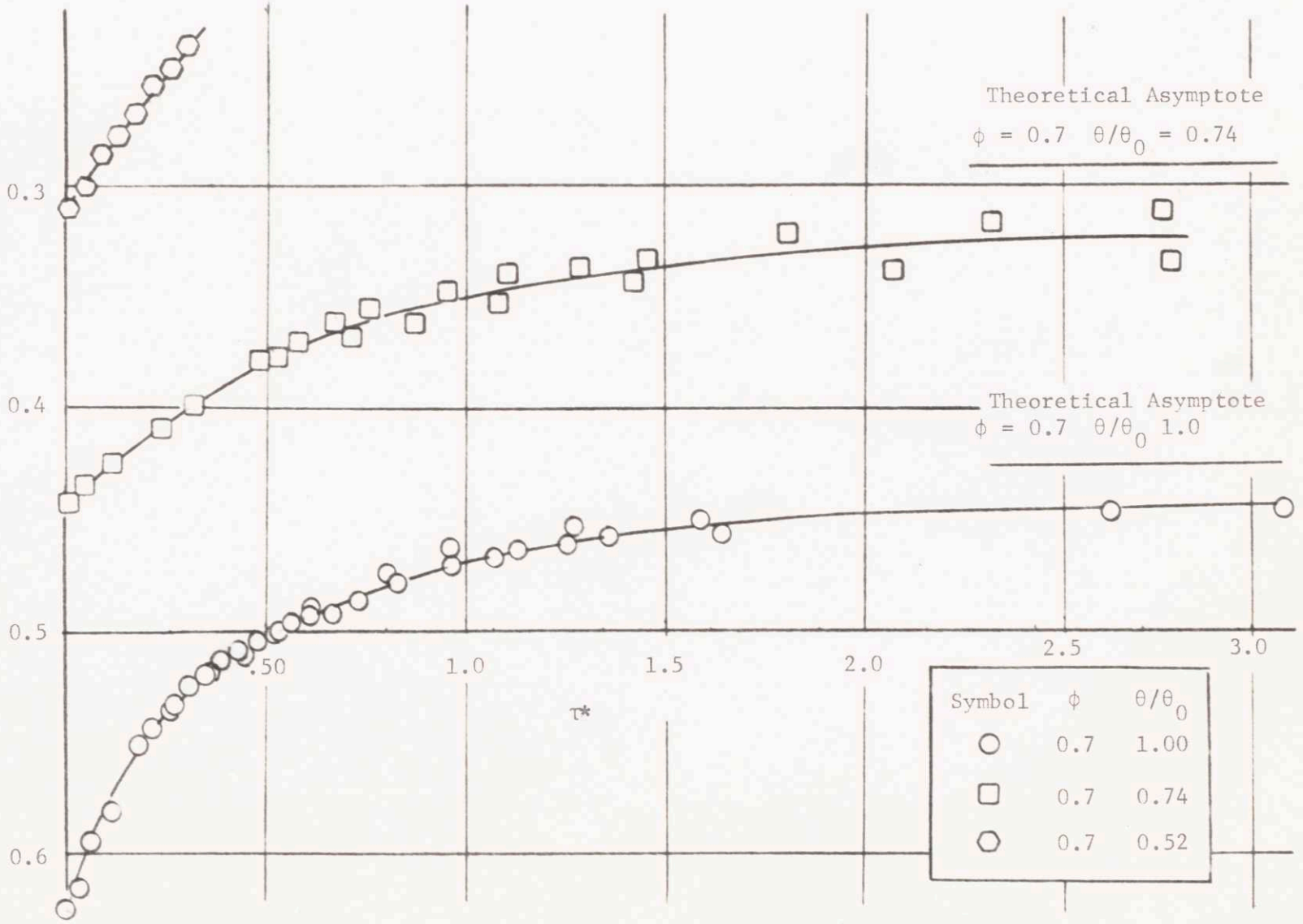

* After Injection of Dye

FIGURE 40

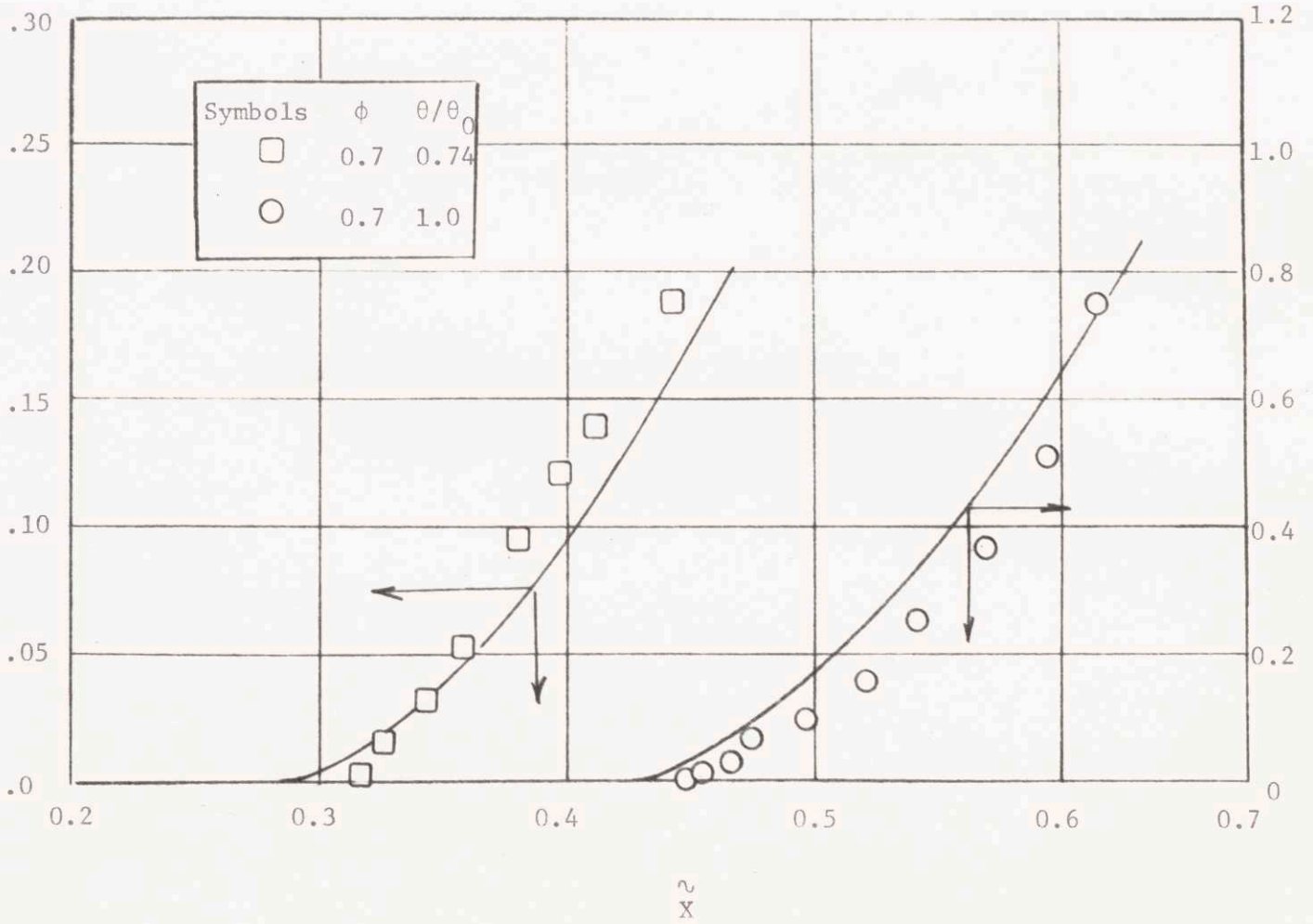
Symbols
ϕ
θ/θ0
0.7
0.74
0.7
1.0
.30
.25
.20
.15
.10
.05
.0
1.2
1.0
0.8
0.6
0.4
0.2
0
0.2
0.3
0.4
0.5
0.6
0.7
u/c θ/θ0 = 0.74
u/c θ/θ0 = 1.0
x̃

FIGURE 41

(a) Leading Edge of Bolus

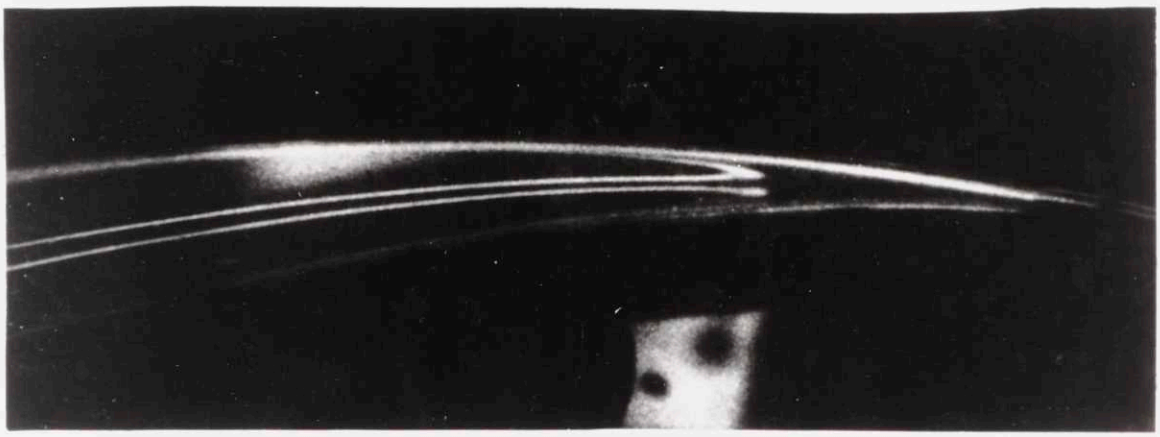

(b) Internal Streamline Pattern

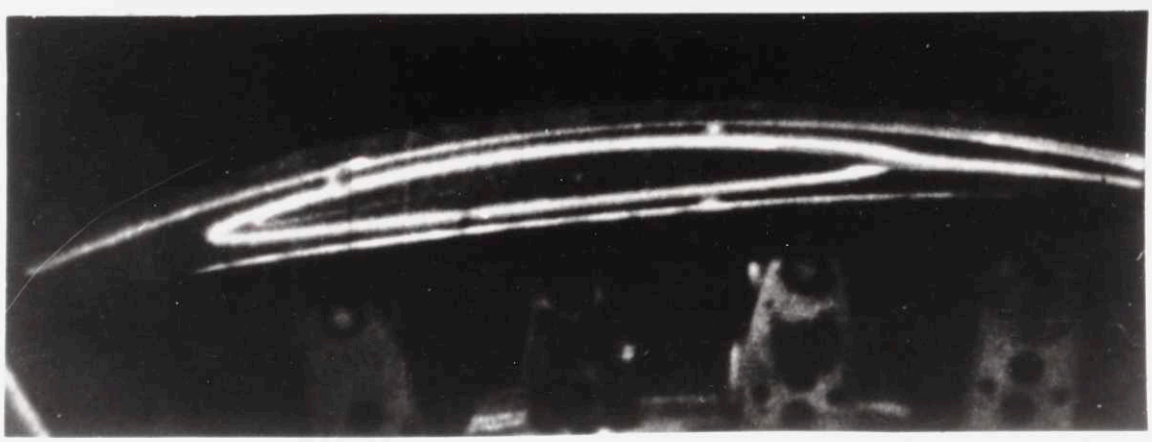

(c) Overall View of Bolus

FIGURE 42

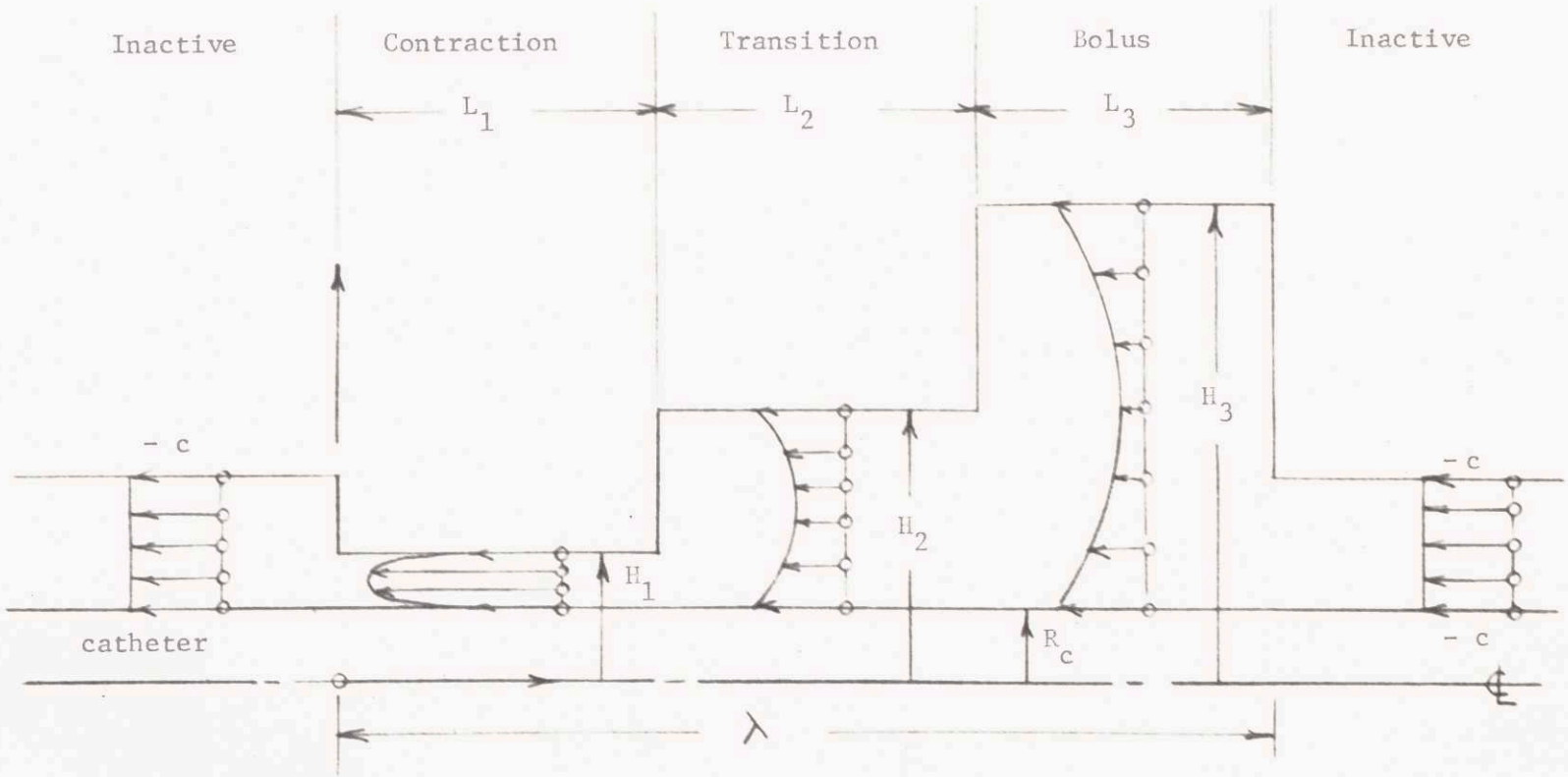

WAVE REFERENCE FRAME

FIGURE 43

Bibliography

1. Burns, J. C., and Parks, T.: "Peristaltic Motion", Journal of Fluid Mechanics. Vol. 29, part 44, pp. 731-743 (1967).

2. Fung, Y. C. and Yih, C. S.: "Peristaltic Transport", manuscript to be published in Journal of Applied Mechanics.

3. Hanin, M.: "The Flow Through a Channel Due to Transversely Oscillating Walls", Israel Journal of Technology, Vol. 6, no. 1-2, pp. 67-71 (1968).

4. Shapiro, A. H., Jaffrin, M. Y., and Weinberg, S. L.: "Peristaltic Pumping with Long Wavelength at Low Reynolds number", Journal of Fluid Mechanics. Vol. 37, part 4, pp. 799-826 (1969). Also published as Massachusetts Institute of Technology, Fluid Mechanics Lab Publication No. 68-5 (1968)

5. Jaffrin, M. Y.: "Inertia and Streamline Curvature Effects on Peristaltic Pumping", manuscript published in Industrial Liason Program, Massachusetts Institute of Technology.

6. Lykoudis, P. S., 1966, "The Fluid Mechanics of the Upper Urinary Tract", Purdue University, School of Aeronautics, Astronautics and Engineering Sciences, Lafayette, Indiana.

7. Narath, P.: Renal Pelvis and Ureter, Grune and Stratton, New York (1951).

8. Kiil, F.: The Function of the Ureter and Renal Pelvis, Sanders Company, Philadelphia (1957).

9. Rattner, W., Fink, S., and Murphy, J.: "Pressure Studies in the Human Ureter and Renal Pelvis", Journal of Urology, Vol. 78, No. 4 (1957), pp. 359-362.

10. Morales, P., Crowder, C., Fishman, A., and Maxwell, M.: "The Response of the Ureter and Pelvis to Changing Urine Flows", Journal of Urology, Vol. 67, No. 4 (1952), pp. 484-491.

11. Maximow, A. A., Bloom, W.: A Textbook of Histology, 7th ed. W. B. Saundars Co., (1957), p. 469.

12. Bäcklund, L.: "Experimental Studies on Pressure and Contractility in the Ureter", Acta Physiologica Scandinavia, Vol. 59, Supplementum 212, Uppsala, Sweden (1963).

13. Barry. W. F., Abscher, R. G., and Boyarsky, S., "Correlation of Cineradiographic Image and Pressure Tracing of Ureteral Activity", presented at a Workship on Hydrodynamics of the Upper Urinary Tract, Center for Continuing Education, University of Chicago, October 1969.

14. Davis, D., Zimskind, and Paquet, J. P.: "Studies on Urodynamics: New Light on Ureteral Function", Journal of Urology, Vol. 90, No. 2, (1963), pp. 150-159.

15. Kreutzmann, H. A. R.: "Studies in Normal Ureteral and Vesical Pressure", Journal of Urology, Vol. 19, (1928), pp. 520-524.

16. Gruber, C. M.: "A Comparative Study of the Intra-Vesical Ureters (Ureters-Vesical Valves) in Man and in Experimental Animals", Journal of Urology, Vol. 21 (1929), pp. 567-581.

17. Boyarsky, S.: "Surgical Physiology of the Renal Pelvis and Ureter", Monograph in the Surgical Sciences Journal, Vol. 1, No. 2 (1964), pp. 173-213.

18. Kass, E.: Boston City Hospital, private communication

19. Latham, T. W.: "Fluid Motions in a Peristaltic Pump", S.M. Thesis, Massachusetts Institute of Technology, 1966.

20. Eckstein, E., "Experimental and Theoretical Pressure Studies of Peristaltic Pumping, S.M. Thesis, Massachusetts Institute of Technology, 1970.

21. Purday, H. F. P.: An Introduction to the Mechanics of Viscous Flow. Dover, England (1949), pp. 16-18.

22. Schlichting, H.: Boundary Layer Theory, McGraw-Hill, New York, 6th edition (1968).

23. McMahon, T., Murthy, V. S., Clark, C., Jaffrin, M. Y., Shapiro, A. H.: "The Dynamics and Fluid Mechanics of the Intra-Aortic Balloon Heart Assist Device", Fluid Mechanics Laboratory Publication, No. 69-11, Massachusetts Institute of Technology, December, 1969.